INORGANIC CHEMISTRY
FRONTIERS

REVIEW

View Article Online
View Journal | View Issue

Cite this: *Inorg. Chem. Front.*, 2020, **7**, 300

Recent advances in MOF-based photocatalysis: environmental remediation under visible light

Qi Wang,*[a,b] Qiaoyuan Gao,[a] Abdullah M. Al-Enizi,[c] Ayman Nafady[c] and Shengqian Ma *[b]

Visible light-induced photocatalysis is a promising way for environmental remediation due to efficient utilization of solar energy. Recently, metal–organic frameworks (MOFs) have attracted increasing attention in the field of photocatalysis. In comparison with traditional metal oxide semiconductors, MOFs have many advantages, such as high specific surface area, rich topology and easily tunable porous structure. In this review, we aim to summarize and illustrate recent advances in MOF-based photocatalysis for environmental remediation under visible light, including wastewater treatment, air purification and disinfection. A series of strategies have been designed to modify and regulate pristine MOFs for enhanced photocatalytic performance, such as ligand functionalization, mixed-metal/linker strategy, metal ion/ligand immobilization, dye sensitization, metal nanoparticle loading, carbon material decoration, semiconductor coupling, MOF/COF coupling, carrier loading and magnetic recycling. The above modifications may result in extended visible light absorption, efficient generation, separation and transfer of photogenerated charges, as well as good recyclability. However, there are still many challenges and obstacles. In order to meet the requirements of using MOF photocatalysis as a friendly and stable technology for low-cost practical applications, its future development prospects are also discussed.

Received 1st September 2019,
Accepted 28th October 2019

DOI: 10.1039/c9qi01120j

rsc.li/frontiers-inorganic

1. Introduction

In the 21st century, environmental pollution and fossil energy crisis have become two major problems that plague human survival and development. Among various renewable energy sources, solar energy is a kind of abundant and clean choice. Thus, solar light-driven technologies for environmental remediation have attracted great attention. Herein, heterogeneous photocatalysis, as represented by TiO_2, was proved to be a feasible way. Upon UV light irradiation, electron–hole (e^-–h^+) pairs can be generated in TiO_2, leading to reductive and oxidative reactions.[1] In this way, various kinds of refractory organic pollutants can be degraded and heavy metal ions can be reduced by TiO_2 photocatalysis.[2] However, UV light accounts for less than 5% of incident solar light, so the utilization of visible light (nearly 45%) is more promising for better utilization of solar energy and future large-scale practical applications. Consequently, there is an urgent need to develop more visible light-responsive photocatalysts with high activity and stability.

Metal–organic frameworks (MOFs) are a class of porous crystalline materials consisting of metallic nodes (metal ions or clusters) and organic linkers.[3] Due to their ultra-high specific surface area (over 6000 $m^2\ g^{-1}$),[4] rich topology and easily tunable porous structure,[5] MOFs have recently attracted increasing attention in the field of photocatalysis.[6–10] Distinct from classical inorganic semiconductors with a delocalized conduction band (CB) and valence band (VB), MOFs can be identified as molecules arranged in a crystalline lattice. In addition, some MOFs, such as MOF-5 ($Zn_4O(BDC)_3$, BDC: 1,4-benzenedicarboxylate), UiO-66 ($Zr_6O_4(OH)_4(BDC)_6$, UiO: University of Oslo) and MIL-125 ($Ti_8O_8(OH)_4(BDC)_6$, MIL: Materials Institute Lavoisier) displayed semiconductor-like behavior. Herein, the metal-oxo clusters and organic linkers can be regarded as isolated semiconductor quantum dots and light-absorbing antenna, respectively.[11–13] In the past few decades, with the development of water/acid-resistant MOF materials,[14] more and more light-responsive MOFs have been reported for the photocatalytic removal of pollutants,[2,8] disinfection of bacteria,[15] production of H_2,[16,17] fixation of CO_2,[18] selective transformation of organics[19] *etc.*[20,21]

Since there are a large number of selections between metal ions/clusters and organic linkers, MOFs are endowed as extremely tunable photocatalysts for efficient utilization of solar light. In the past five years, there are many reviews discussing various aspects of MOFs,[6–9,16,22–26] including environmental

[a]*School of Environmental Science and Engineering, Zhejiang Gongshang University, Hangzhou 310018, China*
[b]*Department of Chemistry, University of South Florida, Tampa, FL 33620, USA. E-mail: wangqi8327@zjgsu.edu.cn, sqma@usf.edu*
[c]*Chemistry Department, College of Science, King Saud University, Riyadh, 11451, Saudi Arabia*

applications. For example, Wang *et al.* summarized the photocatalytic degradation of organic pollutants from wastewater in 2014.[27] At that moment, most photoactive MOFs were applied for the degradation of dyes under UV or UV-Vis light irradiation. Very small numbers of MOFs utilizing visible light were listed and usually need the assistance of H_2O_2 as an oxidant. Later in 2016, Wang *et al.* further conducted a mini-review on the photocatalytic reduction of Cr(VI) by MOFs.[8] In the same year, Ye's group also summarized the progress in MOF photocatalysis. They mainly focused on several representative MOFs, including MOF-5, UiO-66(Zr), MIL-125(Ti) and MIL-101(Fe). In comparison with traditional semiconductors, the reported MOFs or MOF-based composites displayed promising photocatalytic performance, especially in CO_2 reduction.[28] The modified MOFs as photocatalysts were also reviewed by Qiu *et al.*[29] They focused on the progress of various modification strategies to typical light-responsive MOFs. Enhanced photocatalytic performance (pollutant removal, CO_2 reduction, H_2 production or organic transformation) was reported utilizing UV, UV-Vis or visible light. Meanwhile, Bedia *et al.* conducted a review on the synthesis and characterization of MOFs for photocatalytic water purification.[30] Besides, a short review concerning iron-based MOFs for visible light-induced photocatalysis was also reported.[31] In this year, Jiang's group summarized their recent contributions toward MOF-based photocatalysis and photothermal catalysis, mainly focusing on H_2 production and selective organic transformations.[24] However, there were limited reviews focusing on visible light-responsive MOFs, especially for environmental remediation. With the increasing variety of MOFs and MOF-based composites, invaluable application prospects will be expected.

Thus, based on the above analysis, this review aims at recent advances in MOF-based photocatalysis for environmental remediation under visible light, including wastewater treatment, air purification and disinfection. For example, various kinds of organic dyes, phenolic compounds, insecticides, pharmaceuticals and personal care products (PPCPs) in aqueous media can be photodegraded. The structures of typical organic pollutants photodegraded by MOFs are presented in Fig. 1. Besides, the highly migratable Cr(VI) and radiative U(VI) can be photoreduced to their corresponding trivalent states,[8,32] which can be easily precipitated and separated from aqueous solution. Gaseous pollutants such as NO and toluene can be photo-oxidized into harmless products.[33] Inactivation of bacterial was also reported.[34] Thus, for better understanding and easy reading, this review begins with pristine MOFs that can work under visible light. Strategies for engineering MOFs for enhanced performance are further presented, including ligand functionalization, mixed-metal/linker strategy, metal ion/ligand immobilization, dye sensitization, metal nanoparticle loading, carbon material decoration, semiconductor coupling, MOF/COF coupling, carrier loading and magnetic recycling.

2. The development of photoactive MOFs from UV to visible light

Early in 1999, MOF-5 was synthesized by Yaghi's group.[35] In 2004, the optical and vibrational properties of MOF-5 were investigated by Zecchina's group using UV-Vis Diffuse Reflectance Spectroscopy (UV-Vis DRS), photoluminescence (PL) spectroscopy and Raman spectroscopy. It was proposed that Zn_4O_{13} clusters and organic ligands in MOF-5 can behave as ZnO quantum dots (QDs) and light-absorbing antenna, respectively.[36] Until 2007, the semiconductor behavior of MOF-5 was demonstrated by Garcia's group *via* later laser flash

Qi Wang

Qi Wang obtained her Ph.D. degree in 2009 under the supervision of Prof. Jincai Zhao from the Institute of Chemistry, Chinese Academy of Science. She is currently a professor in the School of Environmental Science and Engineering at Zhejiang Gongshang University. She worked as a visiting scholar in the University of South Florida in 2019. Her research interests focus on photocatalysis, photoelectrocatalysis and environmental catalysis.

Shengqian Ma

Shengqian Ma obtained his B.S. degree from Jilin University, China in 2003, and graduated from Miami University (Ohio) with a Ph.D. degree in 2008. After finishing two-year Director's Postdoctoral Fellowship at Argonne National Laboratory, he joined the Department of Chemistry at the University of South Florida (USF) as an Assistant Professor in August 2010. He was promoted to an Associate Professor with early tenure in 2015 and to a Full Professor in 2018. His current research interest focuses on the development of functional porous materials including metal–organic frameworks (MOFs), covalent organic frameworks (COFs), and porous organic polymers (POPs) for energy, biology, and environment-related applications.

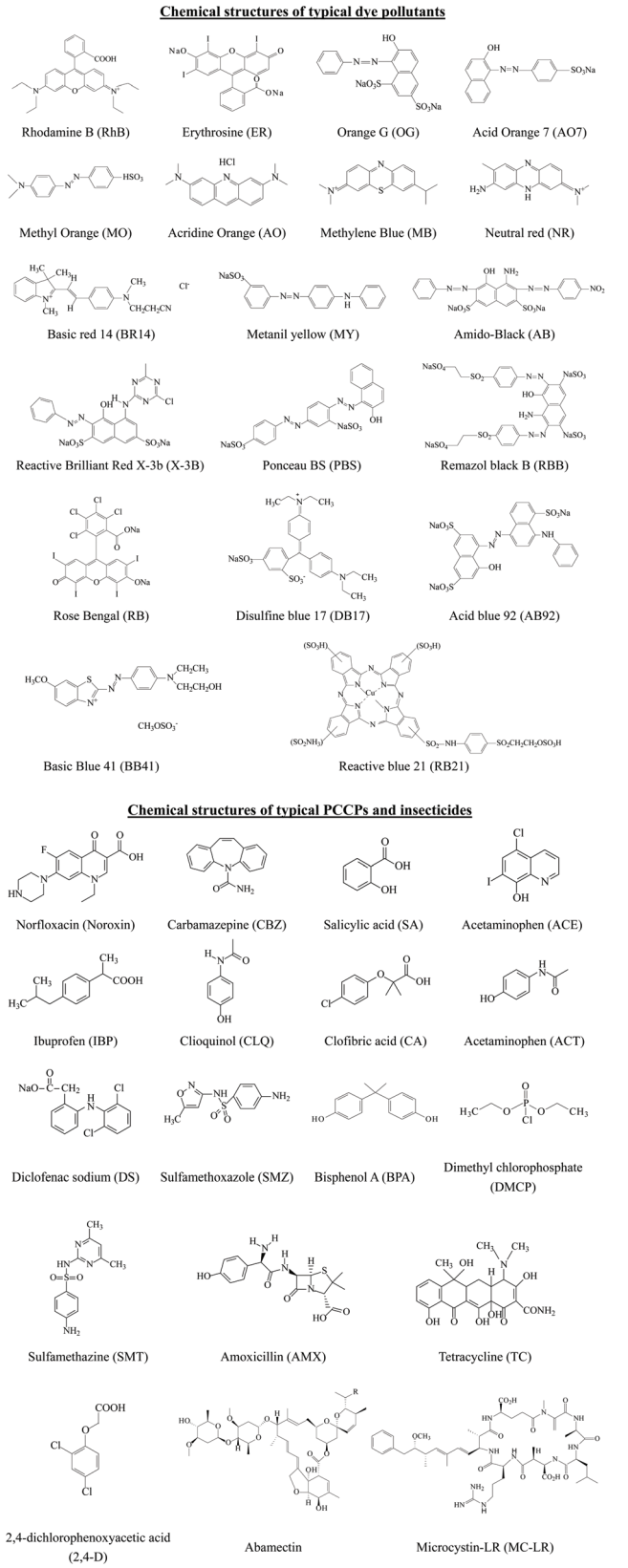

Fig. 1 Chemical structures of typical dyes, PPCPs and insecticides reported in literature studies.

photolysis, and the application of MOF-5 as a photocatalyst for phenol degradation was first tested.[37] The charge-transfer processes on MOF-5 were further studied *via* photoluminescence.[38] Despite these, MOF-5 decomposed gradually upon exposure to moisture in air or in water.[35] The instability of MOF-5 motivated researchers to find or synthesize more stable photocatalytic MOFs.

According to metal–ligand bond strengths and the HSAB (hard/soft acid/base) principle,[5] stable MOFs can be synthesized using either a hard or soft Lewis base. As shown in Fig. 2, high-valent metal ions (such as Ti^{4+}, Zr^{4+}, Al^{3+}, Fe^{3+} and Cr^{3+}) with a hard Lewis base (carboxylates) can lead to the formation of stable MOFs. The MIL series (MIL: Material Institute Lavoisier) and UiO-66(Zr) (UiO: University of Oslo) are representative MOFs with good stability. Besides, divalent metal ions (such as Zn^{2+}, Co^{2+}, Cu^{2+} and Ni^{2+}) with a soft Lewis base (azolates) resulted in several stable MOFs. Among which, zeolitic imidazolate frameworks (ZIFs) constructed by Zn^{2+} and imidazolate linkers were the most representative examples. Consistent with the above classifications, water-stable UiO-66 (Zr) was fabricated and displayed photocatalytic activity for H_2 evolution.[40,41] Besides, MIL-125(Ti) was highly photosensitive and water-stable, which can be photoexcited by UV light leading to the reduction of the Ti(IV) center and oxidation of adsorbed alcohol molecules.[42]

Based on the principle of traditional semiconductor photocatalysis, a photocatalyst can be directly excited by incident light with energy (E_{light}) larger than the band gap (E_g). In this way, electron–hole (e^-–h^+) pairs can be generated (Fig. 3). Similarly, electron transitions can also occur from the highest occupied molecular orbital (HOMO) to the lowest unoccupied molecular orbital (LUMO) in MOFs, leaving holes (h^+) in the HOMO. Herein, the HOMO/LUMO plays similar roles as the CB/VB in semiconductors. Namely, the photogenerated electrons in the LUMO can be transferred to O_2, leading to the formation of superoxide radicals ($O_2^{\bullet-}$). Meanwhile, holes in the HOMO can oxidize the surface hydroxyl group/water, generating hydroxyl radicals ($HO^{\bullet}$). Due to the presence of reactive species ($O_2^{\bullet-}$, $HO^{\bullet}$ and h^+), organic pollutants can be degraded. However, the band gaps ($E_{HOMO-LUMO}$) were reported to be *ca.* 3.4 eV, 3.9 eV and 3.6 eV for MOF-5, UiO-66(Zr) and MIL-125(Ti), respectively.[37,43–45] For effective excitation of such MOFs, the incident light ($E_{light} = 1240/\lambda > E_{HOMO-LUMO}$) was restricted to UV light with a short wavelength ($\lambda < 365$ nm). Thus, for efficient utilization of solar energy, MOFs responsive to visible light ($\lambda > 400$ nm, or $E_{light} < 3.1$ eV) are more desirable.

In contrast to MOFs with wide bandgaps, Fe-MOFs are extremely appealing. The extensive Fe–O clusters can be directly excited by visible light, leading to more efficient utilization of solar energy. Besides, the application cost of Fe-MOFs will be much cheaper due to the Earth-abundant nature of the Fe element. As shown in Fig. 4A, using $Fe(NO_3)_3$ or $FeCl_3$ as the Fe^{3+} precursor, and terephthalic acid (H_2BDC), fumaric acid (H_2FUM) or benzene-1,3,5-tricarboxylic acid (H_3BTC) as the ligand precursor, various kinds of Fe-MOFs (MIL-53,

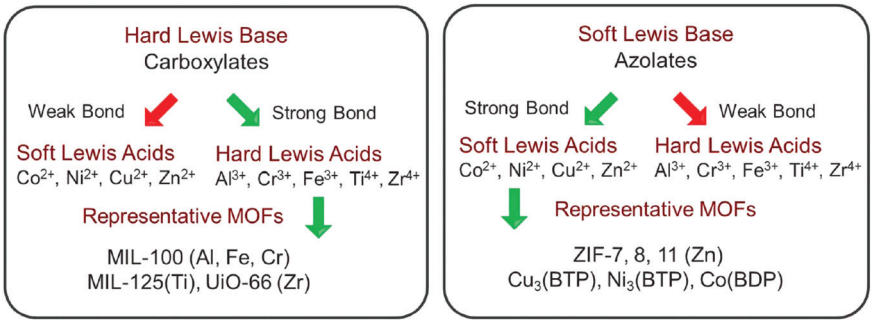

Fig. 2 Strategies to construct stable MOFs guided by HSAB theory. Adapted with permission from ref. 39, © 2018 WILEY-VCH.

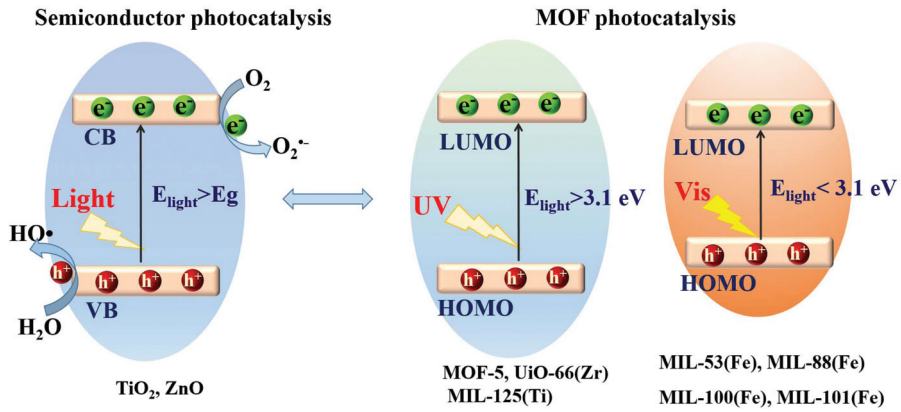

Fig. 3 Mechanism for semiconductor photocatalysis (left); comparison of band gaps and light source (UV or visible light) between representative MOFs (right).

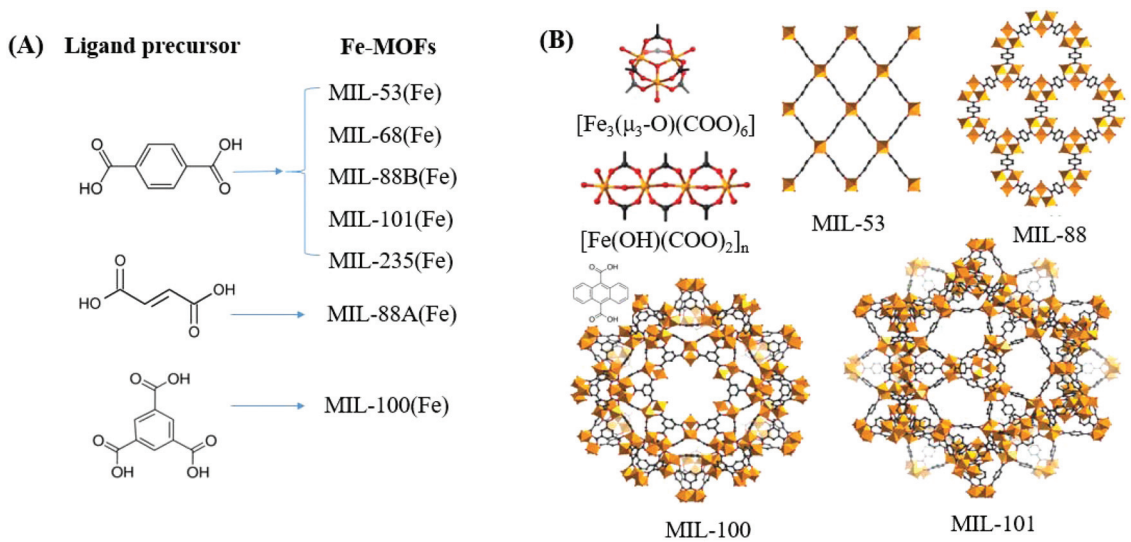

Fig. 4 (A) Fe-MOFs prepared with different ligand precursors; (B) structures of metal clusters and representative MIL series of Fe-MOFs. Adapted with permission from ref. 39, © 2018 WILEY-VCH.

MIL-68, MIL-88A, MIL-88B, MIL-100 and MIL-101) can be obtained. As summarized in Table 1,[39,46] the corresponding $E_{HOMO-LUMO}$ values ranged from 1.88 eV to 2.88 eV, which can be directly excited by visible light. Various kinds of organic pollutants (RhB, MB, AO7, CA, CBZ *etc.*) were reported to be degraded by Fe-MOFs under visible light. However, under

Table 1 Photocatalytic removal of pollutants by typical pristine MOFs under visible light

MOF	Clusters	Ligands	$E_{HOMO-LUMO}$ (eV)	S_{BET} [a] ($m^2\ g^{-1}$)	Pollutant	$C_{pollutant}$ ($mg\ L^{-1}$)	$C_{catalyst}$ ($g\ L^{-1}$)	Time (min)	η [c] (%)	Ref.
MIL-53(Fe)	$[Fe(OH)(COO)_2]_n$	H_2BDC	2.62	NA	AO7 (with PS)	17.5	0.6	90	100	58
			2.88	19	RhB (with H_2O_2)	10	0.4	50	98	59
			2.69	38	RhB (with H_2O_2)	10	0.4	180	90	60
			2.55	16	RhB (with PMS)	40	1.0	20	95	61
			2.72	NA	MB	128	0.01	60	20 [b]	62
			NA	184	CA (with H_2O_2)	40	0.1	280	98	63
					CBZ (with H_2O_2)	40	0.1	280	90	
			2.72	NA	Cr(VI) (with $(NH_4)_2C_2O_4$)	20	1.0	40	100	47
			2.72	NA	U(VI) (with HCOOH, N_2)	50	0.4	120	80	32
			2.91	NA	SMT (with Fe(III), SPC)	5.6	0.2	60	91	64
MIL-68(Fe)	$[Fe(OH)(COO)_2]_n$	H_2BDC	2.80	NA	Cr(VI)(with $(NH_4)_2C_2O_4$)	20	0.25	5	100	65
					Cr(VI) (with MG)	10	0.25	240	95	
					MG (with Cr(VI))	30	0.25	240	80	
MIL-88B(Fe)	$[Fe_3(\mu_3\text{-}O)(COO)_6]$	H_2BDC	NA	NA	MB	10	0.25	50	100	66
					RhB	10	0.25	60	94	
MIL-101(Fe)	$[Fe_3(\mu_3\text{-}O)(COO)_6]$	H_2BDC	1.88	252	TC	50	0.5	180	97	54
MOF-235(Fe)	$[Fe_3(\mu_3\text{-}O)(COO)_6]$	H_2BDC	1.94	148	RhB (with H_2O_2)	19.2	0.2	20	100	67
MIL-88A(Fe)	$[Fe_3(\mu_3\text{-}O)(COO)_6]$	H_2FUM	2.05	NA	MB (with H_2O_2)	32	0.4	20	100	68
MIL-100(Fe)	$[Fe_3(\mu_3\text{-}O)(COO)_6]$	H_3BTC	NA	1974	MO	5	0.33	420	40 [b]	69
HKUST-1	$[Cu_2(CO_2)_4]$	H_3BTC	2.63	197	MG	10	0.25	85	98	70
					SO	15	0.25	85	89	
MIL-53(Al)	$[Al(OH)(COO)_2]_n$	H_2BDC	3.87	NA	MB	128	0.1	60	30 [b]	62
MIL-53(Cr)	$[Cr(OH)(COO)_2]_n$	H_2BDC	3.20	NA	MB	128	0.01	60	32 [b]	62
UiO-66(AN)	$[Zr_6(\mu_3\text{-}O)_4(\mu_3\text{-}OH)_4(COO)_{12}]$	H_2ANDC	2.47	627	MO	20	0.1	90	65	56
UTSA-38	$[(Zn_4O)(COO)_6]$	H_2NDC	2.85	1690	MO	20	0.4	120	64 [b]	71
VNU-1	$[Zr_6O_4(OH)_4(CO_2)_{12}]$	H_2CPEB	2.88	2100	MB	100	0.67	180	100 [b]	57
					MO	100	0.67	180	83 [b]	
Bi-mna	NA	H_2mna	NA	35	RhB	20	1.0	120	96	72
					MB	20	1.0	120	95	
PCN-222	$[Zr_6(\mu_3\text{-}O)_4(\mu_3\text{-}OH)_4(OH)_4(H_2O)_4(COO)_8]$	H_2TCPP	NA	1914	BPA	100	1.0	120	90	73

[a] S_{BET} surface area is presented in integer numbers. [b] UV-Vis light or sunlight. [c] Removal efficiencies (η) for pollutants are used as received or estimated from the figures in the reference and presented in integer numbers. NA: no experimental data available; PS: persulfate; PMS: peroxymonosulfate; SPC: percarbonate; SMT: sulfamethazine; H_2BDC: terephthalic acid; H_2FUM: fumaric acid; H_3BTC: benzene-1,3,5-tricarboxylic acid; H_2ANDC: anthracene-9,10-dicarboxylic acid; H_2NDC: 2,6-naphthalenedicarboxylic acid; H_2CPEB: 1,4-bis(2-[4-carboxyphenyl]ethynyl) benzene; H_2mna: 2-mercaptonicotinic acid; H_2TCPP: tetrakis (4-carboxyphenyl) porphyrin.

most circumstances, H_2O_2 was added as an electron acceptor to accelerate the degradation process. Besides, photocatalytic reduction of Cr(VI) or U(VI) can also be achieved on MIL-53(Fe) using $(NH_4)_2C_2O_4$ or HCOOH as the h^+ scavenger.[32,47]

Among the various visible light-responsive Fe-MOFs mentioned above, MIL-100(Fe) with a tricarboxylate linker was theoretically more stable than Fe-MOFs (MIL-53, MIL-88 and MIL-101) with a dicarboxylate linker.[5] As illustrated in Fig. 4B, both MIL-100(Fe) and MIL-101(Fe) display 3D structures. Among which, MIL-100(Fe) possesses thermal and water stability.[48] Whereas, MIL-101(Fe) may be transformed into MIL-53 or MIL-88 in strong polar solvents.[49,50] Furthermore, MIL-100 was reported to have higher water stability than UiO and ZIF.[51–53] The non-toxicity of MIL-100 was also verified by *in vivo* toxicity assays. Thus, MIL-100(Fe) is expected to be a promising visible light-responsive photocatalyst for environmental remediation. Using antibiotic tetracycline (TC) as the target pollutant, the performance of MIL-53(Fe), MIL-100(Fe) and MIL-101(Fe) was compared by Wang *et al.*[54] However, MIL-101(Fe) rather than MIL-100(Fe) exhibited the highest performance (Fig. 5A). TC can be removed *via* both adsorption and photocatalysis with a value of *ca.* 97% by MIL-101(Fe) after 180 min visible light irradiation. The rate constant (k) was calculated to be 1.6×10^{-2} min^{-1} (Fig. 5B), which was 7.1 and 1.8 times that in MIL-53(Fe) and MIL-100(Fe), respectively. However, the highest specific surface area (S_{BET}) was observed in MIL-100(Fe) (1203 m^2 g^{-1}), which was much larger than that of MIL-101(Fe) (253 m^2 g^{-1}) and MIL-53(Fe) (21 m^2 g^{-1}). Generally, the catalyst surface played an important role in heterogeneous photocatalysis, and larger S_{BET} was usually beneficial for photocatalysis under other identical conditions. As for MIL-101(Fe), in addition to its highest adsorption of TC, its lowest band gap (1.88 eV) may also be beneficial for the greatest TC removal performance. Thus, the difference in the photocatalytic performance of the tested Fe-MOFs may be influenced by both band gap and adsorption properties. Under different conditions (temperature, solvent, *etc.*), the different types of Fe-MOFs may have their own advantages and application fields. Further research work should be undertaken to enhance the photocatalytic performance as well as the water/thermo-stability under harsh conditions.

In addition to Fe-MOFs, the dicarboxylate and tricarboxylate linkers can interact with other metal ions (such as Cu^{2+}, Al^{3+} or Cr^{3+}), leading to the formation of visible light-active HKUST-1 (HKUST: Hong Kong University of Science and Technology), MIL-53(Al) or MIL-53(Cr), respectively. With the development of MOF materials, the selection of ligands was extended from the original H_2BDC/H_3BTC to structures with higher π-conjugation. A large number of visible light-responsive MOFs were synthesized and applied for environmental remediation. For example, the band gap of MOF-5 (4.0 eV) can be reduced to 3.3 eV when using biphenyl or naphthalenedicarboxylic acids as the ligand precursor (Fig. 6A). A novel Zn^{2+}-centered MOF (UTSA-38) with a narrow band gap (2.85 eV) was fabricated using 2,6-naphthalenedicarboxylic acid (H_2NDC) as the ligand precursor (Fig. 6B).[55] Photocatalytic degradation of methyl orange (MO, 20 mg L^{-1}) was achieved by UTSA-38, despite low efficiency (<30%) under visible light irradiation for 120 min.

Moreover, strategies were also developed to utilize the water-stable Ti- and Zr-centered MOFs. Motivated by the findings of MOF-5, the band gaps along with the photocatalytic performance may be tuned by changing the organic linker.[44] As for Zr-MOFs, once H_2BDC was replaced by anthracene-9,10-dicarboxylic acid (H_2ANDC) or 1,4-bis(2-[4-carboxyphenyl] ethynyl) benzene (H_2CPEB), UiO-66(AN) or VUN-1 (VNU: Vietnam National University) with a band gap of 2.47 eV and 2.88 eV was obtained (Fig. 6B), respectively.[56,57] For the degradation of MO (20 mg L^{-1}), shorter time (90 min) and smaller catalyst dosage (0.1 g L^{-1}) led to 65% removal efficiency under visible light.[56] Methylene blue (MB) can be 100% removed by VUN-1 after 180 min UV-Vis irradiation.[40] As for Ti-MOFs, the same strategy still works well. The band gap can be engineered when Ti–O clusters were connected with different organic

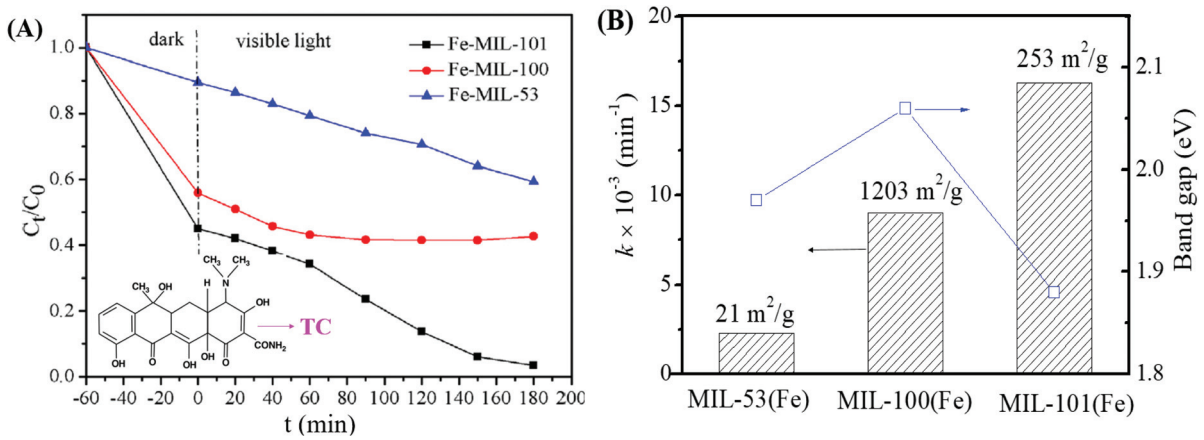

Fig. 5 (A) Photocatalytic degradation of TC by different types of Fe-MILs; (B) rate constant for TC removal on different Fe-MILs in comparison with band gaps and specific surface areas. Adapted with permission from ref. 54, © 2018 Elsevier.

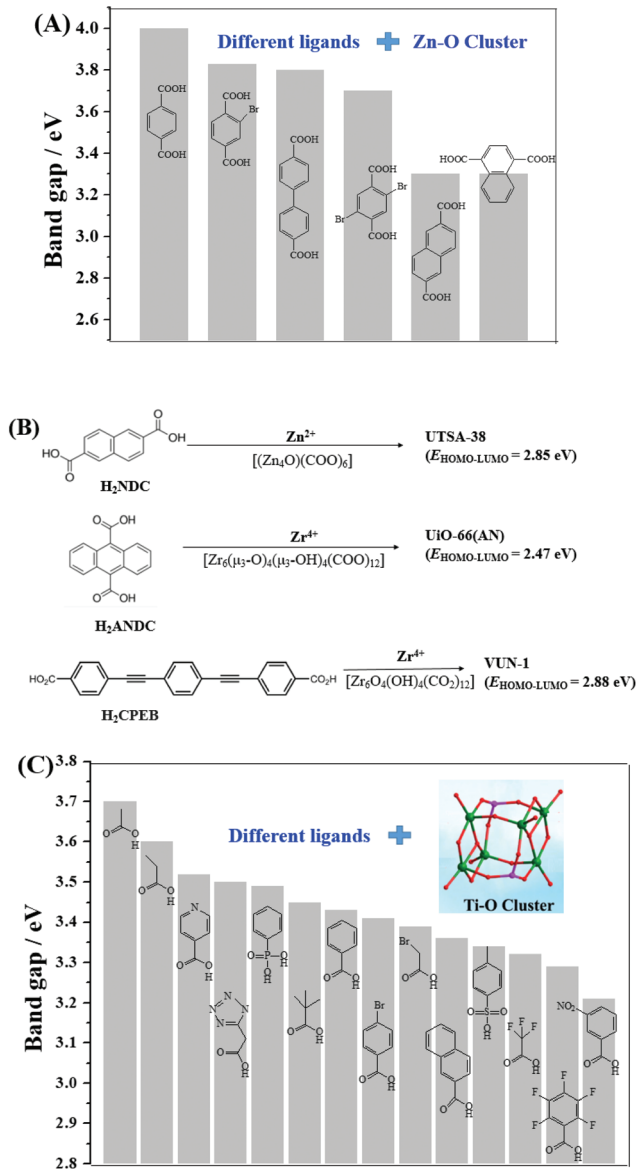

Fig. 6 (A) Bandgap engineering of Zn–O clusters with different organic ligands;[44] (B) visible light-responsive Zn-MOFs and Zr-MOFs prepared with different ligand precursors; (C) bandgap engineering of Ti–O clusters with different organic ligands.[45] Adapted with permission from ref. 44 and 45, © 2008 Wiley-VCH, © 2016 Wiley-VCH.

ligands (Fig. 6C).[45] The performance of different Ti-MOFs was investigated and compared *via* photocatalytic water splitting under UV-Vis light.

3. Strategies for engineering visible light-active MOFs

In comparison with traditional metal oxide semiconductors, MOFs have many advantages in photocatalysis because of their inherent structural features (such as large surface area and porous structure) and a tunable combination between metallic nodes and organic linkers. However, the photocatalytic efficiency still cannot meet the actual needs. Many attempts have been made to enhance the photocatalytic performance. As shown in Fig. 7, a series of strategies have been developed for extended visible light absorption, more efficient generation, separation and transfer of charge carriers, as well as good recyclability.

3.1 Ligand functionalization

Considering the huge difference in available quantities of metal ions and organic linkers, modification of organic linkers rather than metallic modes will be a powerful strategy to tune the optical properties of MOFs. Taking the most frequently studied H_2BDC precursor as an example, MIL-125(Ti) synthesized with unmodified H_2BDC can only respond to UV light.[42] As shown in Fig. 8, after introducing an $-NH_2$ group into H_2BDC, isostructural NH_2-MIL-125(Ti) was synthesized in the same way, which displayed yellow color and extended visible light absorption.[74] The band gap dramatically decreased from 3.60 eV to 2.46 eV. Besides, due to enhanced CO_2 adsorption by the $-NH_2$ group, NH_2-MIL-125(Ti) was reported for the first time as a targeted photocatalyst toward CO_2 reduction under visible light. Furthermore, dye-like moieties with higher π-conjugated groups were used as substituents to H_2BDC.[75] The resulting MR-MIL-125(Ti) displayed a clear red shift of optical absorption. The absorption edge reached almost 700 nm, indicating that the band gap was *ca.* 1.93 eV. Subsequently, a p-type Ti-containing MOF (NTU-9) was also developed, using two –OH group-substituted H_2BDC (2,5-dihydroxyterephthalic acid) as an organic linker.[76] The light absorption region can be extended up to 750 nm. The red NTU-9 sample can act as a visible light-responsive photocatalyst for dye degradation with the assistance of H_2O_2. RhB (48 mg L^{-1}) and MB (32 mg L^{-1}) dyes can be completely degraded after 80 min and 20 min visible light irradiation, respectively. Moreover, high stability can also be observed after three cyclic runs.

To elucidate the specific role of $-NH_2$ substitution in engineering the optical response of MIL-125(Ti), Hendon *et al.* carried out detailed research *via* both experimental and theoretical ways.[77] Results indicated that the enhanced optical properties were ascribed to the regulation of the HOMO. The introduction of a single $-NH_2$ group leads to an elevation of 1.2 eV of the HOMO with no influence on the LUMO. The effect of other functional groups (–OH, $-CH_3$, –Cl) as well as diaminated linker BDC-$(NH_2)_2$ were also studied. The band gaps decreased in the order of $-CH_3$/–Cl < –OH < $-(NH_2)_2$ substitution. Herein, $-(NH_2)_2$ substitution was considered as the most powerful method. Besides, the band gap of MIL-125(Ti) can be rationally regulated by changing the ratio between $-NH_2$ and $-(NH_2)_2$.[77] This strategy can be further extended to other aromatic linkers.

Similar band gap engineering by ligand functionalization was also reported for UiO-66(Zr) and UiO-66(Ce).[78,79] For example, Hendrickx *et al.* conducted a combined theoretical and experimental study on the intrinsic optical properties of

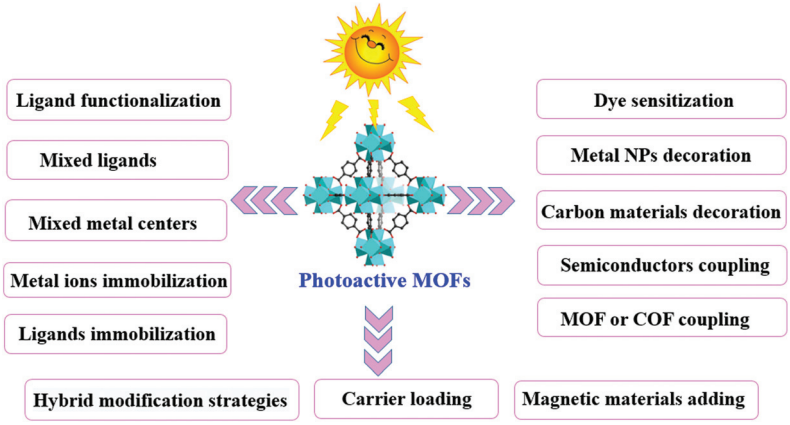

Fig. 7 Strategies to engineer MOFs as efficient photocatalysts for environmental applications.

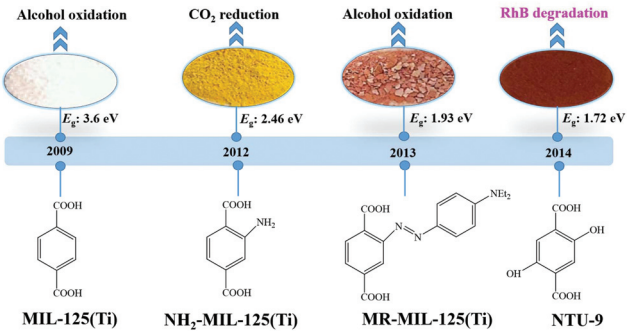

Fig. 8 The development history of Ti-MOFs *via* ligand functionalization and their first application in photocatalysis.

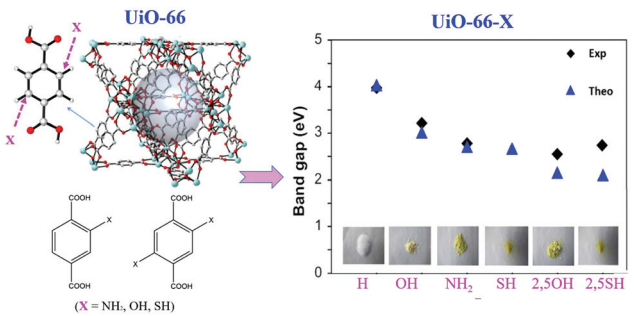

Fig. 9 The effect of functionalized BDC linkers on regulating the band gaps of UiO-66(Zr). Adapted with permission from ref. 78, © 2015 American Chemical Society.

UiO-66(Zr).[78] As shown in Fig. 9, using mono or bifunctionalized BDC linkers, the band gap of UiO-66(Zr) can be engineered from 4.0 eV to 2.2 eV. The values obtained *via* HSE06 calculations agreed well with the experimental results. As for the mechanism of band gap engineering, similar to NH_2-MIL-125 (Ti),[77] the decreased band gap was ascribed to the elevation of the HOMO after ligand functionalization.[80] Typically, according to the theory of conventional semiconductor photocatalysis, a narrower band gap means more efficient response to visible light, which may have a positive effect on the photocatalytic performance under visible light. Unexpectedly, some difference was reported for MOF photocatalysis. For example, UiO-66–X (X = H, NH_2, NO_2 or Br) were synthesized and compared for the oxidation of As(III) and the reduction of Cr(VI) under visible light.[43] As listed in Table 2, the photocatalytic performance of the as-prepared UiO-66 MOFs was strongly affected by different functionalized linkers. Among the four tested samples, $-NH_2$ functionalization displayed the highest photocatalytic activity for either As(III) oxidation or Cr(VI) reduction. For example, As(III) can be 100% removed by UiO-66–X (X = NH_2), while the value was 60%, 18% or 50% for –H, $-NO_2$ or –Br functionalized UiO-66, respectively.[43] In comparison with unmodified UiO-66, the absorption edges were red-shifted to *ca.* 360, 400 and 450 nm for UiO-66–X (X = Br, NO_2 and NH_2), respectively. Correspondingly, decreased band gaps were estimated from 3.88 to 2.76 eV.

However, the photocatalytic performance for both As(III) oxidation and Cr(VI) reduction was not correlated with band gaps. Only $-NH_2$ functionalization enhanced the photocatalytic performance, while $-NO_2$ and –Br had an inhibitory effect. Based on further exclusion of the influence of specific surface area, the above phenomena can be explained by the electronic effects of ligands. As shown in Fig. 10, the $\log(K_X/K_H)$ correlated well with the Hammett's σ_m values of different X ligands. Herein, K_X and K_H represent the rate constants for As(III) oxidation by UiO-66–X and UiO-66 respectively. The electron-donating group ($-NH_2$) with a negative σ_m value can enhance the electron density around the Zr–O cluster, leading to increased separation and transfer of photogenerated charge carriers. Whereas, the electron-withdrawing groups ($-NO_2$ and –Br) had an opposite effect. Thus, rather than the surface area or band gap, the electronic effect was considered to play a dominating role in affecting the photocatalytic performance of UiO-66–X. Subsequently, the electronic effects of ligand substitution were also demonstrated using functionalized MIL-68(In) for the photocatalytic treatment of Cr(VI)-containing wastewater.[81]

Table 2 Ligand functionalization of typical MOFs for the photocatalytic removal of environmental pollutants under visible light

MOFs	$E_{HOMO-LUMO}$ [a] (eV)	S_{BET} [b] ($m^2\ g^{-1}$)	Pollutant	$C_{pollutant}$ ($mg\ L^{-1}$)	$C_{catalyst}$ ($g\ L^{-1}$)	Time (min)	η [c] (%)	Ref.
UiO-66(Zr)–X: X substituted H_2BDC as the ligand precursor								
X = H	3.88	1141	As(III)[d]	2	1.0	60	64	43
X = NH_2	2.76	733		2	1.0	60	100	
X = NO_2	3.10	465		2	1.0	60	18	
X = Br	3.44	456		2	1.0	60	50	
X = H	3.88	1141	Cr(VI)[d]	10	0.5	100	20	43
X = NH_2	2.76	733		10	0.5	100	100	
X = NO_2	3.10	465		10	0.5	100	11	
X = Br	3.44	456		10	0.5	100	15	
MIL-68(In)–X: X substituted H_2BDC as the ligand precursor								
X = H	3.94	611	Cr(VI)[d,e]	20	1.0	60	16	81
X = NH_2	2.79	584		20	1.0	60	100	
X = NO_2	3.02	582		20	1.0	60	<5	
X = Br	3.70	601		20	1.0	60	8	
NH_2–MOFs: NH_2 functionalization with different metal centers								
MIL-125(Ti)	NA	NA	Cr(VI)	8	0.5	45	60	82
MIL-53(Fe)	NA	NA		8	0.5	45	17	
MIL-88B(Fe)	NA	NA		8	0.5	45	100	
UiO-66(Zr)	NA	NA		8	0.5	45	46	
Development of NH_2 functionalization								
NH_2-MIL-101(Fe)	1.32	NA	Toluene	27.6	0.16	360	79	33
NH_2-UiO-66(Zr) film	2.90	NA	Cr(VI)	5	0.5	120	98	83
NH_2-UiO-66(Hf) film	2.88	NA	Cr(VI)	5	0.9	120	99	83
Hierarchical NH_2-MIL-125(Ti)	2.53	1133	RhB	100	0.4	120	84	84
NH_2-MIL-125(Ti)	2.64	1129	NO	NA	0.4	5	31	85
NH_2-MIL-125(Ti)	2.75	1344	Cr(VI)[f]	48	0.4	60	91	86
MIL-68(In)-NH_2	2.82	674	Cr(VI)[g]	20	1.0	180	97	87
Other group functionalization								
NTU-9[i]	1.72	NA	RhB[h]	48	0.5	80	100	76
			MB[h]	32	0.5	20	100	

NA: no experimental data available. [a] $E_{HOMO-LUMO}$ is used as received or estimated from the adsorption edges of MOFs. [b] S_{BET} surface area is presented in integer numbers. [c] Removal efficiencies (η) for pollutants are used as received or estimated from the figures in the reference and presented in integer numbers. [d] UV-Vis light or sunlight. [e] Addition of ammonium oxalate under a N_2 atmosphere. [f] Addition of ethanol. [g] Addition of ethanol under a N_2 atmosphere. [h] Addition of H_2O_2. [i] $(OH)_2$-H_2BDC as the organic ligand.

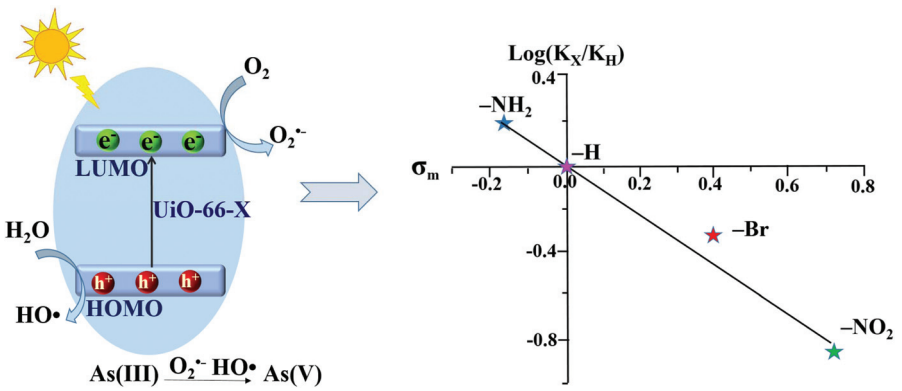

Fig. 10 Proposed mechanism (left) and Hammett plot (right) for photocatalytic oxidation of As(III) by UiO-66–X (X = H, NH_2, NO_2 or Br). Reproduced from ref. 43 with permission from the PCCP Owner Societies.

In addition to UV-active MIL-125(Ti) and UiO-66(Zr), –NH_2 functionalization was also applied to Fe-containing MOFs. Similarly, enhanced visible light absorption and photocatalytic performance can be observed. Moreover, the effect of –NH_2 functionalization on different MOFs was further investigated.[82] For example, the performances of NH_2–MIL-88B(Fe), NH_2–MIL-125(Ti) and NH_2–UiO-66(Zr) were compared for the reduction of aqueous Cr(VI). Among which, NH_2–MIL-88B(Fe) displayed the highest activity. Cr(VI) can be totally reduced by NH_2–MIL-88B(Fe) within 45 min visible light irradiation (Table 2). Whereas, the values were 60% and 46% by NH_2–MIL-125(Ti) and NH_2–UiO-66(Zr), respectively. The superior performance of NH_2–MIL-88B(Fe) can be explained by dual excitation pathways. Namely, both Fe–O clusters and the –NH_2

group can be excited. The electron transfer from the excited $-NH_2$ to the Fe-O center led to increased separation of photogenerated charge carriers, as well as enhanced Cr(VI) reduction.

Moreover, $-NH_2$ functionalized Fe-MOFs also displayed potential application in air purification. For example, Zhang *et al.* demonstrated that hexagonal NH_2-MIL-101(Fe) spindles can be applied for the visible light-induced degradation of gaseous toluene.[33] As shown in Fig. 11A, NH_2-functionalization dramatically enhanced the visible light absorption of MIL-101 (Fe), corresponding to a decreased band gap (1.32 eV). After 6 h visible light irradiation, *ca.* 79% toluene can be degraded by NH_2-MIL-101(Fe). Whereas, the value was *ca.* 11% by TiO_2 (Fig. 11B). The mechanism for toluene degradation was revealed using an *in situ* FTIR technique (Fig. 11C). Characteristic peaks corresponding to the aromatic ring (3079 and 3038 cm^{-1}) and methyl groups (2937 and 2881 cm^{-1}) in toluene gradually decreased with prolonged irradiation time. Meanwhile, the peaks of CO_2 (2362 and 2337 cm^{-1}) gradually increased. The formation of a degradation intermediate (benzoic acid) was also deduced *via* the signals of the carboxylate group (1504, 1545 and 1562 cm^{-1}). Thus, the oxidative degradation of toluene to CO_2 can be confirmed (Fig. 11D).

3.2 Mixed-metal/linker strategy

Due to the versatility and flexibility of MOFs, the mixed-metal/linker strategy has been developed for preparing more efficient MOFs with desirable properties using more than one metal (mixed-metal) center or/and more than one organic linker (mixed-linker), respectively.[88–92] Typically, additional metal ions or linkers can be introduced into a MOF structure through a solvothermal or post-synthetic modification approach.[92] The as-prepared MOFs with mixed components exhibited unique and superior catalytic activity relative to pristine MOFs with a single component. Due to more types of

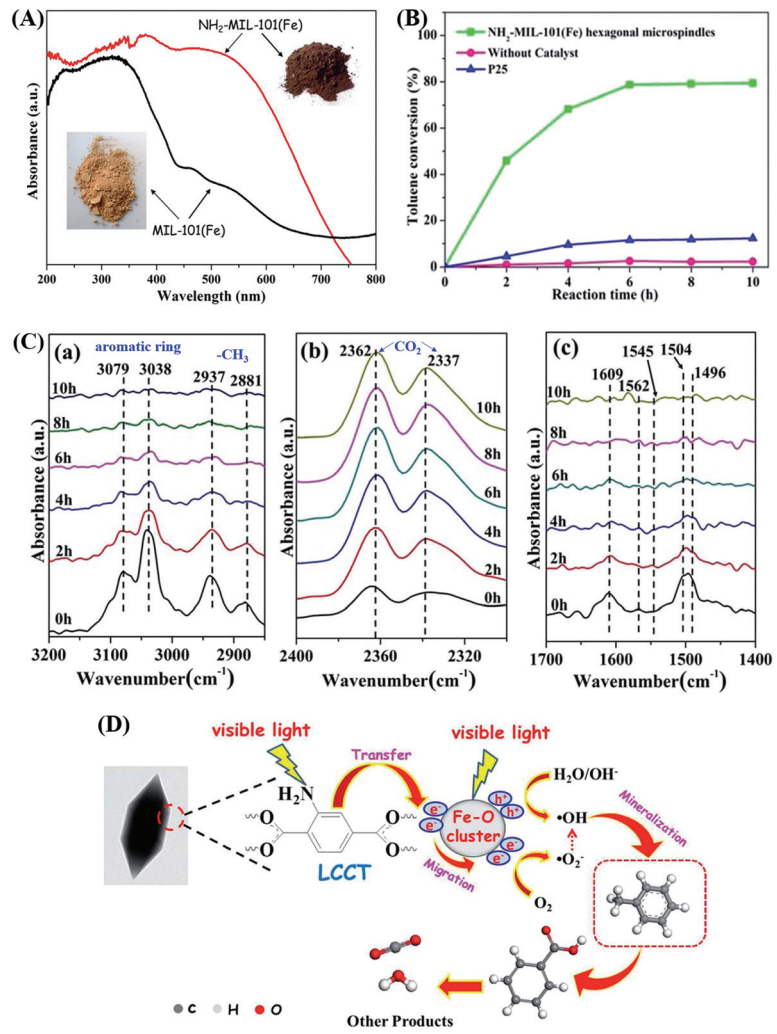

Fig. 11 (A) UV-Vis DRS of MIL-101(Fe) and NH_2-MIL-101(Fe); (B) photocatalytic degradation dynamics of toluene; (C) *In situ* FTIR spectra of toluene at different irradiation time by NH_2-MIL-101(Fe) in different regions: (a) 3200–2850 cm^{-1}, (b) 2400–2300 cm^{-1} and (c) 1700–1400 cm^{-1}; (D) proposed mechanism for toluene degradation by NH_2-MIL-101(Fe) under visible light. Adapted from ref. 33 with permission from The Royal Society of Chemistry.

active sites, enhanced photocatalytic performance may be anticipated.[93]

As for MOFs with mixed metals,[90] partial substitution of metal centers could regulate their efficiency for charge separation as well as photocatalytic performance.[92,94–106] Oxo-bridged heterometallic assemblies with more flexibility and tenability can be formed within the same MOFs.[92,99] For example, Ni-doped ZIF-8 was fabricated *via* a one-pot mechanochemical method.[100] The active Ni(II) centers in the backbones of ZIF-8 can regulate the light absorption region from UV to visible light. Under visible light irradiation, Ni-doped ZIF-8 with purple color can be excited, leading to efficient degradation of MB dye within 25 min, whereas, pristine ZIF-8 with white color displayed negligible activity. Besides, Cu^{2+} was successfully doped into the structure of ZIF-67 *via* initially mixing $Cu(COO)_2$, $Co(COO)_2$ and 2-methylimidazole in an organic solvent followed by a solvothermal procedure at 140 °C for 7 days.[98] The as-prepared Cu-doped ZIF-67 (Cu/ZIF-67) displayed significantly enhanced performance for methyl orange (MO) degradation under visible light. Recently, Cu doped NH_2-MIL-125(Ti) was also developed for enhanced photocatalytic degradation of MO and phenol.[101] At an optimal Cu doping amount (1.5 wt%), the estimated rate constants for MO and phenol were 10.4 and 3.4 times relative to that for pristine NH_2-MIL-125(Ti), respectively. As shown in Fig. 12, the doping of Cu^{2+} will introduce a shallow state below the position of the LUMO, which may trap electrons from the LUMO and transfer them to other electron acceptors *via* the Cu^{2+}/Cu^{+} redox cycle. In this way, the recombination of charge carriers can be greatly inhibited.

Besides, Ti substituted UiO-66–NH_2(Zr) was achieved by a post-synthetic exchange method.[94,95] The as-prepared UiO-66–NH_2(Zr/Ti) exhibited enhanced photocatalytic performance for CO_2 reduction and H_2 production, which was ascribed to the presence of Ti^{4+} as an electron mediator. Furthermore, Yasin and co-workers carried out theoretical DFT calculations of band gaps for UiO-66–X (X: H, NO_2 or NH_2) with different ratios of mixed metallic centers (Zr, Ti or Hf).[107] Results indicated that the band gap decreased gradually with increasing percentage of Ti^{4+} substitution. The lowest band gap (1.61 eV) was calculated on fully substituted Ti-BDC-NH_2. Despite these, either the conventional solvothermal method or the post-synthetic exchange approach took too long time (up to days or even weeks).[108] To overcome this barrier, a microwave-assisted method was recently developed due to much shorter reaction time and lower energy consumption.[109,110] For example, Ti substituted UiO-66–NH_2 could be fabricated within a few hours with well-maintained crystallinity and enhanced photocatalytic activity.

Similar to MOFs with mixed metals, MOFs with mixed linkers were also developed as unique photocatalysts. Using NH_2-BDC and X-BDC (X: H, F, Cl, Br) as the primary and secondary linker, respectively, a series of Zr-based MOFs were synthesized in one-pot reactions.[111] The introduction of X-BDC with an electron-withdrawing halogen group can lead to enhanced photocatalytic performance for alcohol oxidation, among which, Zr-MOF with NH_2-BDC and F-BDC mixed linkers exhibited the highest performance.

By computational prediction, Grau-Crespo *et al.* reported a conceptually simple route to engineer the band edge positions of ZIFs using mixed organic linkers.[112] As illustrated in Fig. 13A, a series of organic linkers were calculated. Relatively wide band gaps (>3.3 eV) can be observed using a single type of organic linker (Fig. 13B), indicating unachievable excitation by visible light. Whereas, the band gap dramatically decreased to 1.9 eV and 2.5 eV for ZnX_2 by combining fIm or mIm with nIm linkers. The predicted band positions were theoretically ideal for visible light-induced CO_2 reduction and water splitting. Moreover, they also calculated the influence of metal ion doping. Cu^{2+} doping would led to narrower band gaps with increased photo-absorption and e^{-}–h^{+} recombination times, which was consistent with the experimental results in the mixed-metal strategy.

The combinations of mixed-metal and mixed-ligand strategies were also developed. For example, Amador *et al.* reported the synthesis of a UiO-67–Ru–Ti MOF through the combination of two pathways (Fig. 14).[113] Firstly, 4,4′-biphenyldicarboxylic acid (BPDC) and $Ru(Bpy)_2$(5,5′-dcbpy) were employed in the solvothermal process, which acted as the structure and light-absorbing antenna, respectively. Subsequently, Zr^{4+} was partially substituted by Ti^{4+} *via* post-synthetic exchange. The as-prepared UiO-67–Ru–Ti MOF was evaluated by the degradation of MB dye. Dramatically enhanced performance can be observed under visible light relative to UiO-67–Ru or UiO-67–Ti with the single modification strategy.

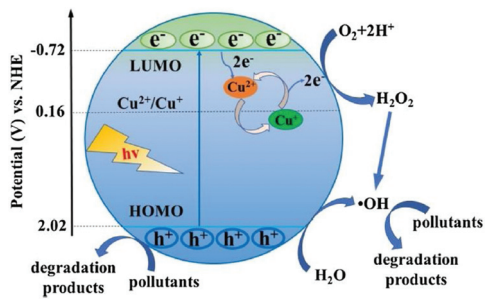

Fig. 12 Proposed mechanism for electron transfer pathways during the degradation of pollutants by Cu doped NH_2-MIL-125(Ti) under visible light. Adapted with permission from ref. 101, © 2018 Elsevier B. V.

3.3 Metal ion/ligand immobilization

In addition to functional group modification, implantation of transition metal ions to complex with ligands was reported to be a feasible way for enhanced photocatalytic performance.[114,115] For example, the implantation of Fe^{3+} in porphyrinic MOFs (PCN-224) was achieved *via* a post synthetic reaction between pristine MOFs and $FeCl_3$ in DMF solution.[114] As illustrated in Fig. 15A, the unsaturated Fe^{3+} was implanted into the porphyrin unit, leading to the formation of Fe@PCN-224. The uniform distribution of Fe in FCN-224 can be further confirmed by HAADF-STEM (high-angle annular

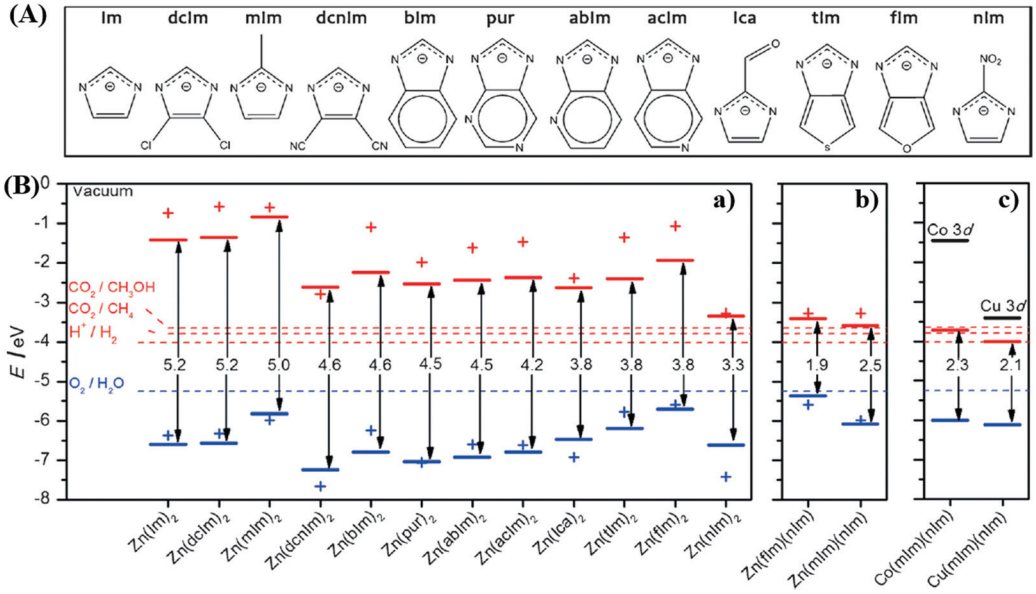

Fig. 13 (A) The chemical structures of different organic linkers (X) for constructing ZnX_2 MOFs; (B) calculated HOMO (blue) and LUMO (red) positions of ZnX_2 crystal structures (lines) and isolated HX molecules (crosses): (a) ZnX_2 with different combinations of organic ligands; (b) equivalent plot for ZnX_2 created by combining fIm or mIm with nIm linkers; (c) equivalent plot for Co(mIm)(nIm) and Cu(mIm)(nIm). Adapted with permission from ref. 112, © 2016 Wiley-VCH.

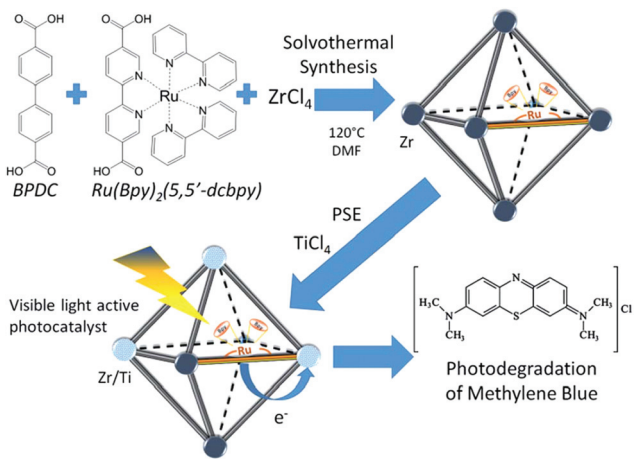

Fig. 14 Schematic processes for preparing a UiO-67–Ru–Ti MOF and its application.[113] Adapted with permission from ref. 113, © 2017 Elsevier B.V.

dark-field scanning TEM) and the corresponding elemental mapping images (Fig. 15B). After Fe^{3+} implantation, the optical response was extended to a longer wavelength, and the recombination of e^-–h^+ pairs was inhibited, which were revealed by UV-Vis Diffuse Reflectance Spectroscopy (UV-Vis-DRS), and photoluminescence (PL) and fluorescence lifetime measurements. Besides, the introduction of additional Fe^{3+} can also promote the activation of *in situ* generated H_2O_2, leading to more active $O_2^{\bullet-}$ and $HO^{\bullet}$ species. Thus, the photo-oxidation of gaseous isopropanol (IPA) was significantly boosted in Fe@PCN-224. The generation rate for the degradation intermediate (acetone) and product (CO_2) exhibited an 8.9 and 9.3 times enhancement relative to pristine PCN-224, respectively (Fig. 15C and D). Good stability for Fe@PCN-224 can be deduced from cyclic experiments (Fig. 15E). Besides, this strategy was also applicable for the modification of another porphyrinic MOF (PCN-222), which exhibited similar behaviors. Different from the Fe(III) complex in the porphyrin unit, the immobilization of Bi(III) in MIL-101(Cr) *via* a two-step hydrolysis route led to the formation of small Bi-oxoclusters inside the mesocages of MIL-101.[115] The complete photodegradation of methyl red (MR) can be easily achieved by the as-prepared Bi(III)@MIL-101(Cr) composite.

Starting from the characteristics of pollutants, the implantation of appropriate substances that can accumulate pollutants on the surface or in the tunnel of MOFs has also been verified as an efficient method. For example, due to selective binding with radiative U(VI), phosphonate was previously verified as an efficient ligand for functional materials in adsorptive remediation of uranyl. Recently, Wang's group reported the post-synthetic modification of Zr-clusters in PCN-222 with aminomethylphosphonic acid (PN-PCN-222) and ethanephosphonic acid (P-PCN-222).[116] It can be deduced from Fig. 16A that the morphology of PCN-222 was well maintained after ligand incorporation. Besides, phosphonic acids are chemically grafted onto the Zr clusters. Due to simultaneous selective complexation and photocatalytic reduction, U(VI) can be completely removed with an extremely wide concentration range (from 1 to 400 ppm). As shown in Fig. 16B, PN-PCN-222 (0.5 g L^{-1}) exhibited the highest performance for U(VI) removal (756.1 mg g^{-1}). At a lower catalyst dosage (0.25 g L^{-1}), the uptake amounts for U(VI) were 184.2 and 1289.3 mg g^{-1} in the dark and under visible light, respectively. Moreover,

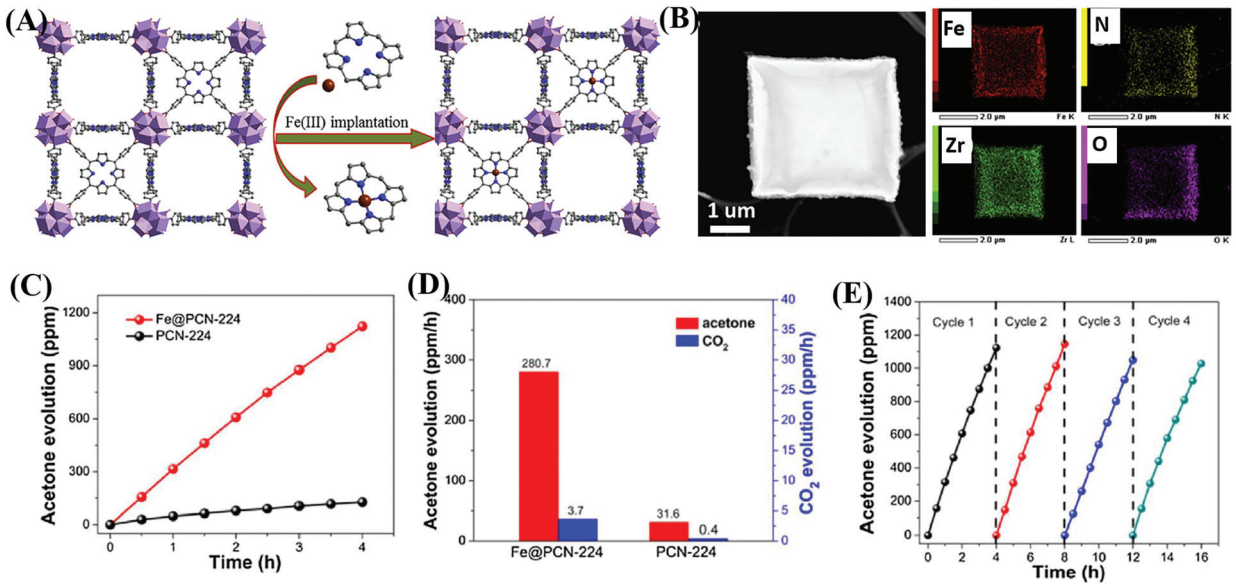

Fig. 15 (A) Schematic illustration for implanting Fe^{3+} into the porphyrin unit of PCN-224; (B) HAADF-STEM image of Fe@PCN-224 and its corresponding elemental mapping images; (C) Time-dependent acetone evolution and (D) Evolution rate of acetone and CO_2 during photocatalytic oxidation of IPA by PCN-224 and Fe@PCN-224; (E) cyclic photocatalytic evolution of acetone by Fe@PCN-224. Adapted with permission from ref. 114, © 2017 Elsevier B.V.

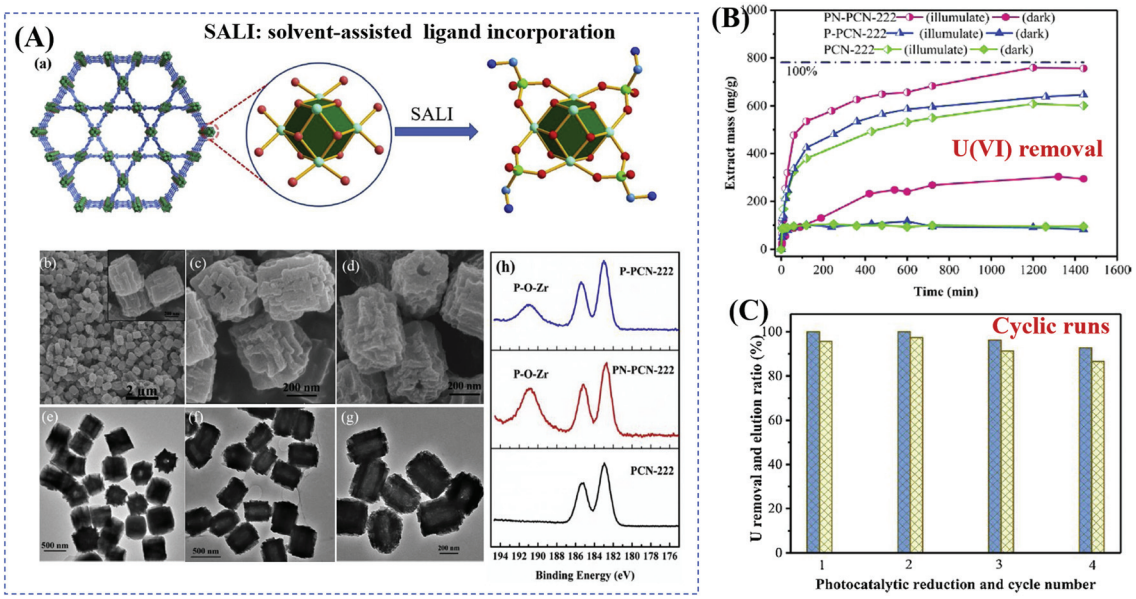

Fig. 16 (A) Schematic representation for modification of PCN-222 (Zr: green; P: bottle green; C: cambridge blue; O: red; N: blue; H atoms are omitted) (a); SEM and the corresponding TEM images of PCN-222 (b, c), PNPCN-222 (c, f), and P-PCN-222 (d, g); XPS spectra of Zr(IV) in different samples (h); (B) uranium extraction (400 ppm) by different samples; (C) cyclic extraction efficiency of U (10 ppm) *via* a photoreduction method (left axis) and elution 0.1 M HCl (right axis). Adapted with permission from ref. 116, © 2019 Elsevier B.V.

PN-PCN-222 exhibited stable photocatalytic performance and recyclability for U(VI) removal (Fig. 16C).

3.4 Dye sensitization

Dye sensitization is a mature way for harvesting more incident solar light, which is well known in dye-sensitized solar cells (DSSCs). Different from the traditional semiconductor-based system, a strong π–π stacking as well as van der Waals interaction may be expected in dye-sensitized MOFs due to the extensive presence of benzene rings in the organic linker of both MOFs and dyes. Inspired by this, dye-sensitized photocatalysis was further developed using MOFs as the substrate.

Specific dyes can be selected to form a complex with MOFs. As shown in Fig. 17, dye molecules in the ground state can absorb incident light and be transformed into the excited state (dye*). As long as the potential of dye* is more negative than the LUMO position of MOFs, electron injection from dye* to the LUMO of MOFs will be feasible. Finally, the electrons can be transferred to different acceptors (O_2, H^+ or CO_2) leading to the formation of active $O_2^{\bullet-}$, H_2 or $HCOO^-$, respectively. In this way, the excitation wavelength can be extended to visible light. At the beginning, many researchers were focused on H_2 production and CO_2 reduction.[75,117–122] Recently, dye-sensitized MOFs were gradually applied in the field of environmental remediation.[123–126]

For example, zinc phthalocyanine (ZnTCPc) was applied to form a complex with UiO-66 and UiO-66(NH_2) *via* an impregnation method.[124] As shown in Fig. 18, in comparison with pristine MOFs, both the ZnTCPc modified samples displayed enhanced visible light activity for MB degradation. Besides, due to the synergistic effect of visible light-responsive UiO-66 (NH_2), the degradation efficiency increased from 68% by ZnTCPc/UiO-66(Zr) to 89% by ZnTCPc/UiO-66(NH_2) after 120 min visible light irradiation. In addition to metal–organic ZnTCPc dye, Thakare and Ramteke reported the post-modification of MOF-5 using 8-hydroxyquinoline (HOQ) dye for the degradation of colorless phenol.[123] After 80 min visible light irradiation, phenol (1 mg L^{-1}) can be completely degraded using HQQ/MOF (4 g L^{-1}) as a photocatalyst. Whereas, less than 5% phenol was degraded using unmodified MOF-5, indicating the vital role of HQQ dye. Moreover, the photocatalytic performance remained well up to 5 cyclic runs. No difference was observed in both XRD and UV-Vis-DRS analyses, indicating the stability of the HQQ/MOF-5 composite. Besides, Rhodamine B (RhB) dye, which was frequently reported as a target dye pollutant, was also applied to sensitize MIL-125(Ti) *via* a post-impregnation method.[127] For the degradation of MO dye, boosted performance was observed from inactive MIL-125 (Ti) to more than 90% on RhB/TiO_2 after 60 min visible light irradiation. Trichromatic dyes, such as Basic Yellow 24 (BY24), Basic Red 14 (BR14) or Methylene Blue (MB), were also encapsulated in Cu-MOFs. The as-prepared dye@Cu-MOFs all exhibited enhanced performance for the degradation of large sized Reactive Blue 13 (RB13). Among which, MB@Cu-MOFs displayed the highest activity. The reason was ascribed to the difference in the visible light-absorption region. For example, MB covers 450–750 nm, which is broader than that of BR14 (380–580 nm) and BY24 (325–480 nm).

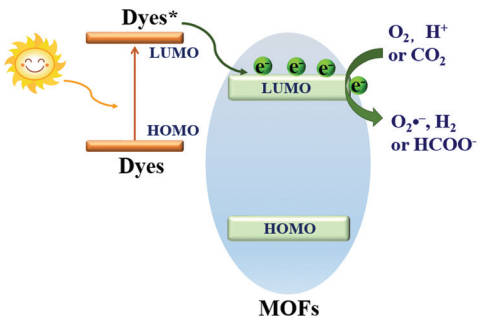

Fig. 17 Electron transfer pathway in a dye sensitized MOF (wide band gap) system.

3.5 Metal nanoparticle loading

Due to the porous characteristics, photoactive guest species can be incorporated into the pore spaces or partially stabilized on the surface of MOFs. Metal nanoparticles (MNPs), especially small noble MNPs with structural diversity and tailoring ability, are promising guest species. As a typical design, the encapsulation of MNPs into the cavity of MOFs can regulate the size and enhance the stability of MNPs. Up to now, the MNP/MOF composites have shown great potential in photocatalysis.[29,128–131] Herein, due to low Fermi energy levels, the MNP co-catalysts were reported to serve as electron acceptors and mediators. Sometimes, they can also enhance the visible and/or NIR light absorption. For example, due to the localized surface plasmon resonance (LSPR) effect, the loading of noble MNPs led to enhanced visible light absorption and excitation.[132–134]

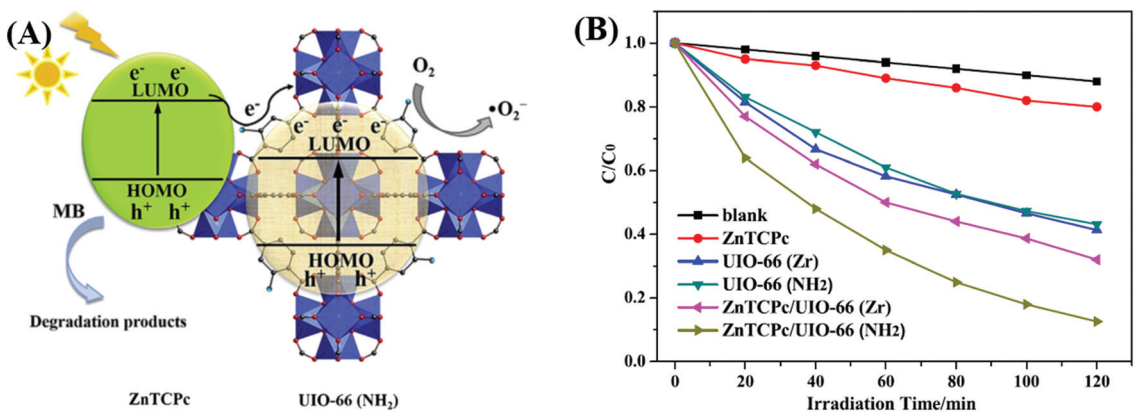

Fig. 18 (A) Proposed mechanism for the degradation of MB by ZnTCPc/UIO-66(NH_2) under visible light; (B) degradation dynamics of MB by different samples. Adapted with permission from ref. 124, © 2016 Elsevier B.V.

For photocatalytic elimination of environmental pollutants, Pd nanoparticles (3 to 6 nm in diameter) were immobilized and highly dispersed in NH_2-UiO-66(Zr) *via* a one-pot hydrothermal method. The as-prepared Pd@NH_2-UiO-66(Zr) composite displayed reusable and highly enhanced photocatalytic activity for Cr(VI) reduction.[135] As listed in Table 3, at a catalyst dosage of 0.5 g L^{-1} and after 90 min visible light irradiation, the removal efficiency for Cr(VI) increased from 33% to 99% after Pd loading. Besides, the BET surface area slightly increased from 756 to 837 m^2 g^{-1}, indicating more surface active sites. Moreover, the addition of an organic dye (MB or MO) can further promote the reduction of Cr(VI). In this way, dye oxidation and Cr(VI) reduction can be simultaneously achieved by photogenerated electrons (e^-) and holes (h^+), respectively.

Furthermore, Pd@MIL-100(Fe) with a higher surface area was also fabricated (2102 m^2 g^{-1}).[145] As shown in Fig. 19A and B, using H_2PdCl_4 as the precursor, 1 wt% Pd nanoparticles (6 to 10 nm in diameter) with high dispersion were anchored on MIL-100(Fe) *via* a facile alcohol reduction method. The as-prepared brown Pd@MIL-100(Fe) powder displayed slightly enhanced absorption in the visible light region relative to the unmodified one. For the photocatalytic degradation of pharmaceuticals and personal care products (PPCPs), such as theophylline, ibuprofen and bisphenol A, Pd@MIL-100(Fe) displayed superior photocatalytic activity (Fig. 19C). The enhanced photocatalytic performance was ascribed to more efficient separation of photogenerated e^-–h^+ pairs and easier transfer of interfacial charges induced by Pd loading. To gain more insight into the reaction, trapping experiments using different radical scavengers were further carried out, and the results indicated that $HO^{\bullet}$ played a major role for PPCP degradation. Thus, a proposed mechanism is given in Fig. 19D.

Furthermore, Wu's group prepared a series of M@MIL-100(Fe) (M: Au, Pd or Pt) *via* a photochemical route and compared their photocatalytic performance under visible light.[137] Metal ion precursors can capture the photogenerated electrons in the LUMO of MIL-100(Fe), leading to the reduction and deposition of the corresponding MNPs on the MIL-100(Fe) substrate. The average diameters were estimated to be 15, 12 and 2 nm for Au, Pd and Pt nanoparticles, respectively (Fig. 20A). The as-prepared M@MIL-100(Fe) was compared for the photocatalytic removal of MO and Cr(VI) under visible light. Enhanced photocatalytic activity can be observed after loading different kinds of MNPs, among which Pt loading exhibited the highest performance. The order of Pt@MIL-100(Fe) > Pd@MIL-100(Fe) > Au@MIL-100(Fe) > MIL-100(Fe) was consistent with the results of visible light absorption and photocurrent response (Fig. 20B and C), but in the reverse order of the surface area. Therefore, the presence of noble MNPs plays a crucial role in enhancing visible light absorption and prolonging the lifetime of photogenerated charges, which together lead to boosted photocatalytic performance for the removal of environmental pollutants.

Ag nanoparticles are also excellent electron sinks due to the formation of Ag-MOF Schottky junctions at the interface. Thus, the e^-–h^+ recombination in MOFs can be greatly inhibited, leading to enhanced photocatalytic activity after loading Ag nanoparticles. For example, Ag@MIL-125(Ti) was fabricated through a facile photo-reduction method. The $AgNO_3$ precursor can be photo-reduced to uniform Ag nanoparticles (~40 nm) and loaded onto the surface of MIL-125(Ti). After 40 min of visible-light irradiation, about 8% RhB was degraded by pure MIL-125(Ti), whereas, the value was boosted to 93% by Ag@MIL-125(Ti).[140] Simultaneously, the post-synthetic modification of NH_2-MIL-125(Ti) with acetylacetone (AC) led to the

Table 3 Photocatalytic removal of environmental pollutants by MNP/MOF composites under visible light

MNPs/MOF	S_{BET} variation[a] (m^2 g^{-1})	Pollutant	$C_{pollutant}$ (mg L^{-1})	$C_{catalyst}$ (g L^{-1})	Time (min)	η variation[b] (%)	Ref.
Pd@NH_2-UiO-66(Zr)	756 → 837	Cr(VI)	10	0.5	90	36 → 99	135
Pd@MIL-100(Fe)	2006 → 2102	Theophylline[c]	20	0.125	150	82 → 100	136
		Ibuprofen[c]	20	0.125	150	67 → 100	
		Bisphenol A[c]	20	0.125	240	35 → 66	
Pd@MIL-100(Fe)	2007 → 1898	MO[c]	20	0.125	40	41 → 84	137
		Cr(VI)[d]	20	1.0	8	69 → 100	
Pt@MIL-100(Fe)	2007 → 1724	MO[c]	20	0.125	40	41 → 100	137
		Cr(VI)[d]	20	1.0	8	69 → 86	
Pt/NH_2-MIL-125(Ti)	1052 → 896	Cr(VI)	15	1.0	120	41 → 77[e]	138
Pt/NH_2-MIL-125(Ti)	1101 → 910	Nitrobenzene[f]	3075	6.25	1200	NA → 98	139
Au@MIL-100(Fe)	2007 → 1822	MO[c]	20	0.125	40	41 → 65	137
		Cr(VI)[d]	20	1.0	8	69 → 82	
Ag@MOF-5	NA	*E. coli*	NA	NA	70	28 → 91	34
Ag@MIL-125(Ti)	NA	RhB	NA	1.0	40	8 → 93	140
Ag/MIL-125(Ti)-AC	1245 → 977	MB	20	0.06	30	55 → 100[g]	141
Ag/UiO-66–NH_2	NA	Cr(VI)	10	1.0	105	40 → 90	142
PtPd@ZIF-8	1024 → 713	C_2H_4	100	NA	120	<5 → 93[e]	143
CuPd@ZIF-8	1531 → 1259	Cr(VI)	20	0.2	60	22 → 89[e]	144

NA: no experimental data available. [a] S_{BET} variation indicates the surface area of MOFs before and after loading MNPs. [b] Removal efficiencies (η) for pollutants are used as received or estimated from the figures in the reference and presented in integer numbers; η variation indicates the performance of MOFs before and after loading MNPs. [c] Addition of H_2O_2. [d] Addition of ammonium oxalate. [e] UV-Vis light or solar light. [f] In acetonitrile with the addition of TEOA. [g] 100 W daylight lamp.

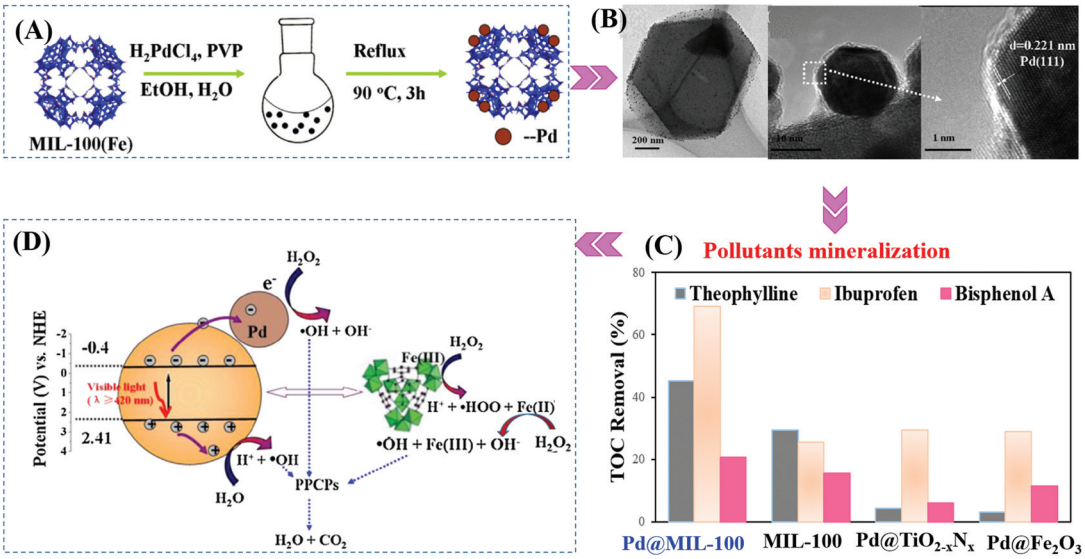

Fig. 19 (A) Schematic processes for preparing Pd@MIL-100(Fe) *via* a facile alcohol reduction method; (B) TEM and HRTEM images of Pd@MIL-100 (Fe); (C) TOC removal efficiency of theophylline, ibuprofen and bisphenol A by different photocatalysts. Reaction conditions: 5 mg photocatalyst, 40 mL PPCPs (20 mg L^{-1}), 40 μL H_2O_2, pH 4; (D) proposed mechanism for visible-light-induced PPCP degradation by Pd@MIL-100(Fe). Adapted with permission from ref. 145, © 2015 Elsevier B.V.

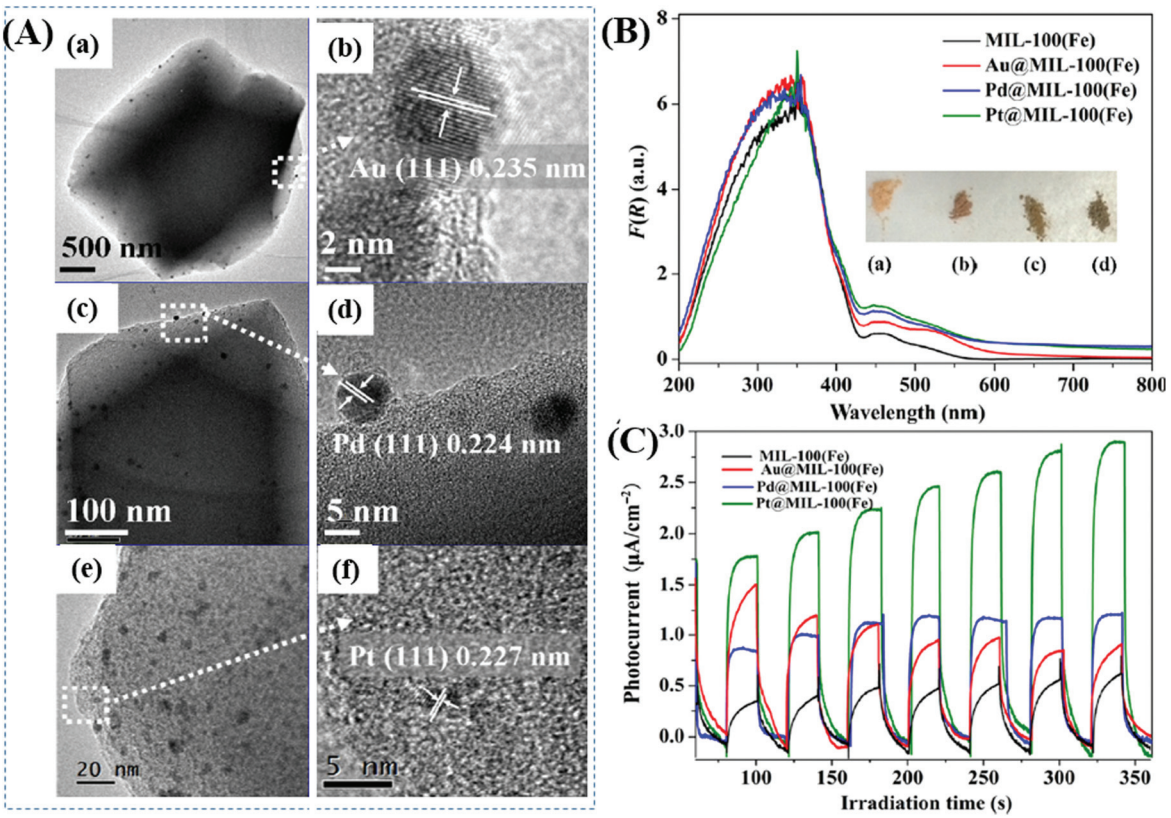

Fig. 20 (A) TEM and the corresponding HRTEM images of (a, b) Au@MIL-100(Fe); (c, d) Pd@MIL-100(Fe); (e, f) Pt@MIL-100(Fe); (B) UV-vis DRS spectra and (C) photocurrent response of MIL-100(Fe) and M@MIL-100(Fe). Adapted with permission from ref. 137, © 2015 Springer.

formation of MIL-125-AC, which was subsequently treated with CH_3COOAg.[141] In this way, smaller Ag nanoparticles, mostly 5–10 nm in size, were spread on the external surface and embedded within NH_2-MIL-125(Ti). The as-prepared Ag/MIL-125(Ti)-AC displayed enhanced activity for photocatalytic degradation of MB dye.

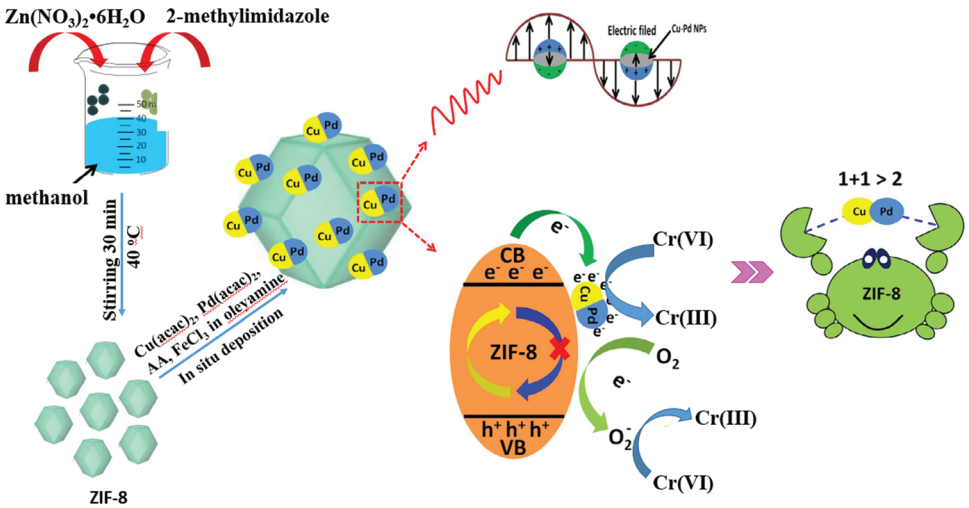

Fig. 21 Schematic processes for preparing CuPd@ZIF-8 and the proposed mechanism for photocatalytic reduction of Cr(VI). Adapted by permission of ref. 143, © 2014 The Royal Society of Chemistry.

In addition to single MNPs, bimetallic alloy nanocrystals were also encapsulated in MOFs for photocatalytic applications. For example, PtPd alloy nanocrystals were encapsulated in microporous ZIF-8 with high dispersion (Table 3). Superior activity for the degradation of ethylene to CO_2 can be achieved.[143] Recently, CuPd alloy nanoparticles was dispersed on ZIF-8 with good stability for Cr(VI) reduction.[144] As shown in Fig. 21, CuPd@ZIF-8 was fabricated *via* a sol–gel method. Compared with pristine ZIF-8, the loading of CuPd alloy led to enhanced adsorption capacity for O_2 and more photogenerated e^-–h^+ pairs due to the LSPR effect. Upon light irradiation, the photogenerated e^- can be directly transferred to Cr(VI) or O_2. Despite the competition of O_2 in capturing e^-, the reduction product of O_2 ($O_2^{\bullet-}$) will also contribute to Cr(VI) reduction, which would finally led to boosted photocatalytic activity. After 60 min visible light irradiation, the efficiency of Cr(VI) reduction increased from 22% on pristine ZIF-8 to 89% on optimized CuPd@ZIF-8 with 5 wt% CuPd. Moreover, other control samples were also tested, which were in the order of CuPd@ZIF-8 > Cu@ZIF-8 > Pd@ZIF-8 > ZIF-8 > CuPd > Pd > Cu. Obviously, the CuPd alloy displayed a synergistic effect compared to single MNPs. Besides, the stability of the optimized CuPd@ZIF-8 was maintained well (>90%) after four successive cyclic runs.

3.6 Carbon material decoration

In traditional semiconductor photocatalytic systems, carbon materials with superior electrical conductivity were widely applied to form hybrid photocatalysts. The recombination of photogenerated charges can be suppressed after the loading of carbon materials.[146–148] For example, graphene oxide (GO), reduced graphene oxide (rGO), carbon quantum dots (CQDs), *etc*. were typical carbon materials, which could accelerate the transfer of photogenerated charges. Similarly, coupling carbon materials with MOFs will also solve the disadvantages of fast charge recombination in pristine MOFs, and lead to enhanced photocatalytic performance. As listed in Table 4, some typical carbon-MOF composites were fabricated. No matter whether the specific surface area (S_{BET}) is increased or decreased, carbon coupling led to boosted photocatalytic performance for the elimination of environmental pollutants.

For example, MIL-53(Fe)/rGO hybrid materials were prepared *via* a simple one-step solvothermal method. With an optimal loading amount of rGO (2.5 wt%), the degradation of MB dye can be increased.[149] Besides, Li *et al.* reported the fabrication of GO modified NH_2-MIL-125(Ti) with enhanced performance for photocatalytic degradation of gaseous pollutants. The light absorption, charge generating and transfer properties of NH_2-MIL-125(Ti) can be greatly altered after GO coupling. For example, the light absorption was greatly enhanced in the region of 200–500 nm, and the absorption edge was also shifted from 445 to 455 nm due to strong interaction between GO and NH_2-MIL-125(Ti). Moreover, the charge transfer resistance was also decreased (Fig. 22A), and the photocurrent response under visible light was dramatically increased (Fig. 22B). Due to the above combined effects, both photocatalytic oxidation of NO and degradation of acetaldehyde were greatly accelerated in optimized GO/NH_2-MIL-125(Ti) relative to pristine NH_2-MIL-125(Ti) (Fig. 22C and D). For better understanding, the proposed mechanism is depicted in Fig. 22E. Namely, upon visible light irradiation, the organic linker (2-aminoterephthalic acid) can be excited and generate electrons which will be transferred to the center of the Ti–O cluster. In this way, the photoexcited electrons will be trapped on metallic Ti by reducing Ti^{4+} to Ti^{3+}. The presence of GO can rapidly accumulate the trapped electrons and accelerate their transfer to O_2. Thus, more reactive $O_2^{\bullet-}$ radicals can be generated, which will be beneficial for the degradation of gaseous pollutants.

As a novel carbon nanomaterial, CQDs were also applied to couple with MOFs. In addition to the beneficial properties of good electron conductivity, easy functionalization, low cost

Table 4 MOF–carbon composites for the photocatalytic removal of environmental pollutants under visible light

MOF-based composite	Carbon materials (wt%)	S_{BET} variation[a] ($m^2\ g^{-1}$)	Pollutant	$C_{pollutant}$ ($mg\ L^{-1}$)	$C_{catalyst}$ ($g\ L^{-1}$)	Time (min)	η variation[b] (%)	Ref.
MIL-53(Fe)	2.5% rGO	NA	MB	20	0.5	80	82 → 95	149
MIL-53(Fe)	0.5% rGO	NA	Cr(VI)[c]	20	1.0	80	79 → 100	150
NH_2-MIL-68(In)	GO	530 → 681	AMX	20	0.6	10	60 → 93	151
MIL-88B(Fe)	10% GO[c]	NA → 99	RR195[d]	100	0.3	20	50 → 95[e]	152
MIL-88(Fe)	3% GO[c]	NA	MB	100	0.5	10	48 → 95[e]	153
			RhB				49 → 94[e]	
NH_2-MIL-125(Ti)	10% GO	871 → 501	NO	0.5	5	30	30 → 50	154
			CH_3CHO	1.95	50	80	48 → 65	
NH_2-MIL-125(Ti)	1% CQDs	487 → 198	RhB	10	0.5	240	67 → 100	155
NH_2-UiO-66(Zr)	2% rGO	732 → 767	Cr(VI)	10	0.5	100	35 → 100	156
ZIF-8	2.5% CQDs[f]	1356 → 1479	NO	0.42	10	30	0 → 43	157
$[Cu_2Br(ptz)]_n$	20% FCF	NA	RhB	4.8	0.25	180	3 → 88	158

NA: no experimental data available; rGO: reduced graphene oxide; GO: graphene oxide; CQDs: carbon nanodots; FCF: functional carbon fiber; ptz: 5-(4-pyridyl)-1*H*-tetrazole. [a] S_{BET} variation indicates the surface area of MOFs before and after loading carbon materials. [b] Removal efficiencies (η) for pollutants are used as received or estimated from the figures in the reference and presented in integer numbers; η variation indicates the performance of MOFs before and after loading carbon materials. [c] Addition of ammonium oxalate. [d] Addition of H_2O_2. [e] UV-Vis light or sunlight. [f] Vol%.

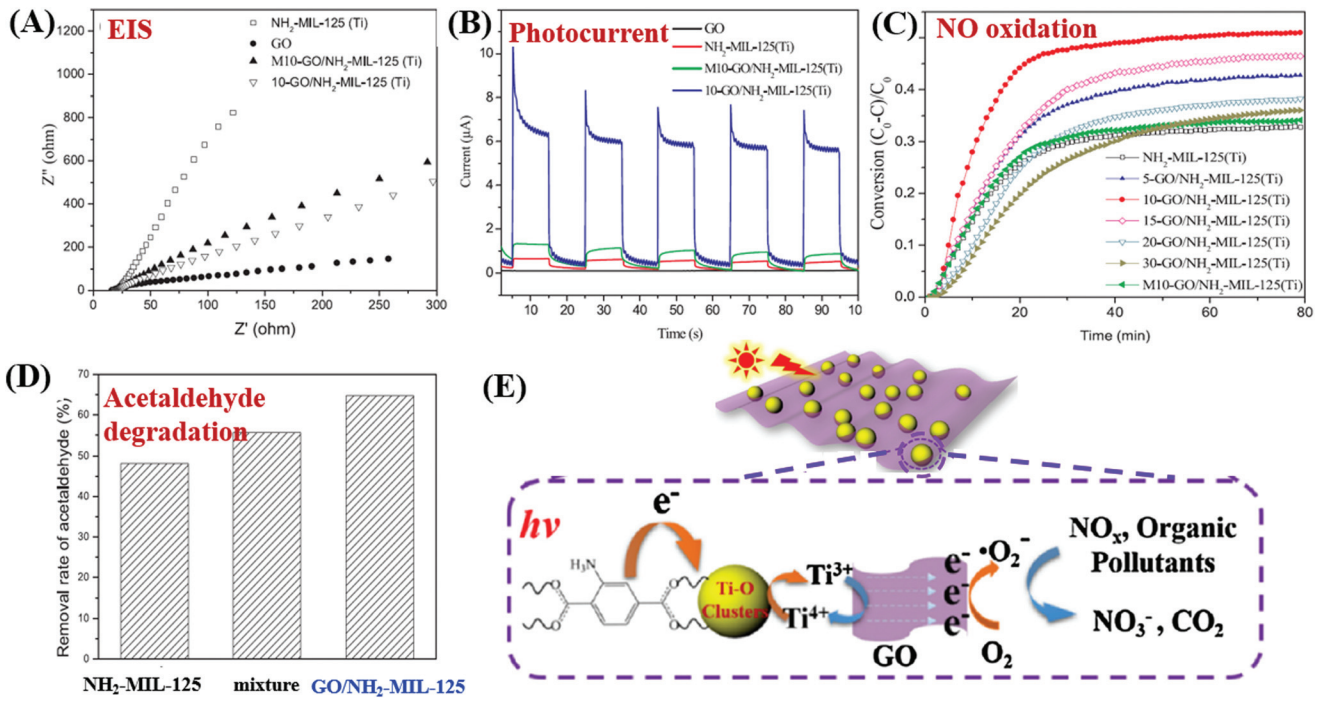

Fig. 22 Comparison of NH_2-MIL-125(Ti) and GO/NH_2-MIL-125(Ti): (A) EIS Nyquist plots and (B) photo-current responses; (C) photocatalytic oxidation of NO; (D) photocatalytic degradation of acetaldehyde; (E) proposed mechanism for pollutant degradation by GO/NH_2-MIL-125(Ti) under visible light irradiation. Adapted with permission from ref. 154, © 2018 Elsevier B.V.

and low toxicity, CQDs have special optical properties in upconversion luminescence.[159–161] The incident near infrared light can be absorbed by CQDs and then converted to visible light which will enhance the utilization of solar energy.[162] As shown in Fig. 23A, CQDs with a size of 2 nm were successfully distributed on NH_2-MIL-125(Ti) *via* a simple solvent-deposition method.[163] The large surface area of NH_2-MIL-125(Ti) (487 $m^2\ g^{-1}$) was beneficial for CQD loading. For the photocatalytic degradation of RhB dye (Fig. 23B), the as-prepared CQD/NH_2-MIL-125 composite always exhibited enhanced performance, no matter the incident light is full spectrum, visible light or near-infrared light. The highest activity was observed at a loading amount of 1 wt% CQDs. Meanwhile, good stability of the optimized CQD/NH_2-MIL-125 can be maintained after 7 successive cyclic runs. For better understanding of the photocatalytic mechanism, photoluminescence (PL) spectra and electrochemical impedance spectroscopy (EIS) Nyquist plots were obtained to investigate the separation efficiency and transfer resistance of photogenerated charge carriers, respectively. Moreover, the upconversion PL spectra were also

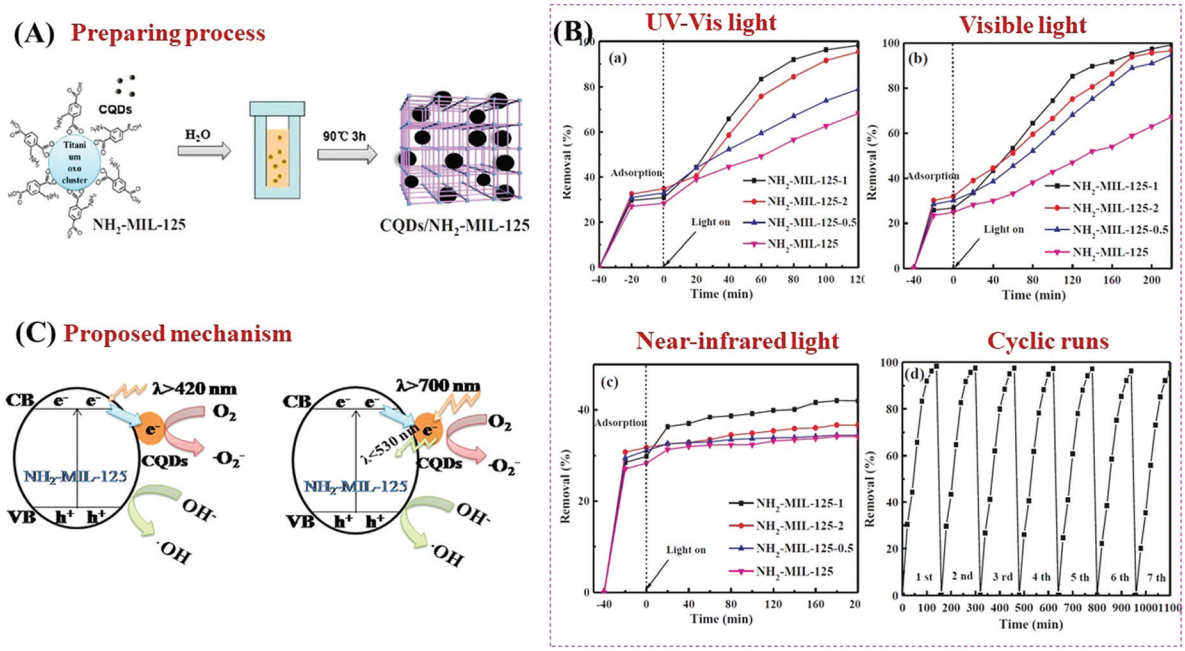

Fig. 23 (A) Schematic processes for preparing CQD/NH_2-MIL-125(Ti); (B) photocatalytic degradation of RhB by NH_2-MIL-125 and CQD/NH_2-MIL-125 composites under the irradiation of (a) full spectrum light, (b) visible light and (c) near-infrared light; (d) cyclic runs for RhB degradation by optimized CQD/NH_2-MIL-125 under full spectrum light; (C) proposed mechanism for charge transfer in CQD/NH_2-MIL-125(Ti) under visible light (λ > 420 nm) and near-infrared light (λ > 700 nm) irradiation; adapted with permission from ref. 155, © 2018 Elsevier B.V.

obtained to detect the unique PL upconversion performance of CQDs. Based on the above results, the mechanisms for charge generation, separation and transfer in CQD/NH_2-MIL-125(Ti) were proposed (Fig. 23C). Under visible light (λ > 420 nm) irradiation, the good electron conductivity of CQDs can facilitate efficient separation of photogenerated e^-–h^+ pairs in NH_2-MIL-125(Ti). Under near-infrared light (λ > 700 nm) irradiation, in addition to electron conductivity, the special upconversion luminescence properties of CQDs can convert near infrared light into visible light, leading to more efficient utilization of solar energy.

As another attractive option, functional carbon fiber (FCF) has several merits, such as high conductivity, large surface area and excellent absorption capability. In particular, FCF can act as a photosensitizer to extend the photoresponse. For example, a new coordination polymer $[Cu_2Br(ptz)]_n$ (CP) (ptz = 5-(4-pyridyl)-1*H*-tetrazole) nanobelt (CPNB) was loaded on the surface of FCF *via* a simple colloidal blending process.[158] The resulting CPNB/FCF composite exhibited significantly enhanced activity for photocatalytic degradation of RhB. At a catalyst dosage of 0.25 g L^{-1} and after 180 min visible light irradiation, the removal efficiency for RhB dramatically increased from 3% using pristine CPNB to 88% using the CPNB/FCF composite. As shown in Fig. 24A, the band gap (E_g) of pristine CPNB was 3.17 eV, and it decreased to 2.02–2.69 eV after loading FCF with different pretreatment times. Moreover, results from both photocurrent response and EIS Nyquist plots indicated the merits of loading FCB (Fig. 24B and C). Considering the flat band potential in the Mott–Schottky plot (Fig. 24C) and the E_g (3.17 eV), the CB and VB positions of CPNB were estimated to be −0.31 V and +2.86 V (*vs.* SCE), respectively. Under visible light irradiation, only FCF can be excited (Fig. 24D). The photogenerated electrons will transfer from the CB of FCF to CPNB, leading to an effective separation of e^-–h^+ pairs.

3.7 MOF-semiconductor heterojunctions

Coupling MOFs with other photoactive semiconductors was another alternative way to enhance the photocatalytic activity. In this approach, the porous network of MOFs can facilitate the dispersion of semiconductors, generating more active sites. Moreover, due to the formation of heterojunctions,[164] more efficient separation of photo-excited charges can be achieved. Typically, there are three types of heterojunctions for semiconductors, depending on the CB/VB position as well as the n/p type nature of independent components (Fig. 25). Until now, many semiconductors have been reported to form composites with MOFs. For example, metal-containing semiconductors (such as ZnO, TiO_2, $BiVO_4$, AgI, α-Fe_2O_3, CdS, *etc.*) and nonmetal graphitic carbon nitride (g-C_3N_4) have been coupled with photoactive MOFs and exhibited superior performance in the field of photocatalysis.

3.7.1 Coupling with metal-containing semiconductors. Since the first report of TiO_2 photocatalysis in 1972, more and more semiconductor photocatalysts have been synthesized and reported. Some semiconductors can be directly excited by visible light, such as BiOBr, BiOI, MoO_3, WO_3, Bi_2MoO_6, $BiVO_4$, AgI, Ag_3PO4, *etc.* As for the construction of MOF-based heterojunctions, such metal-containing semiconductors were

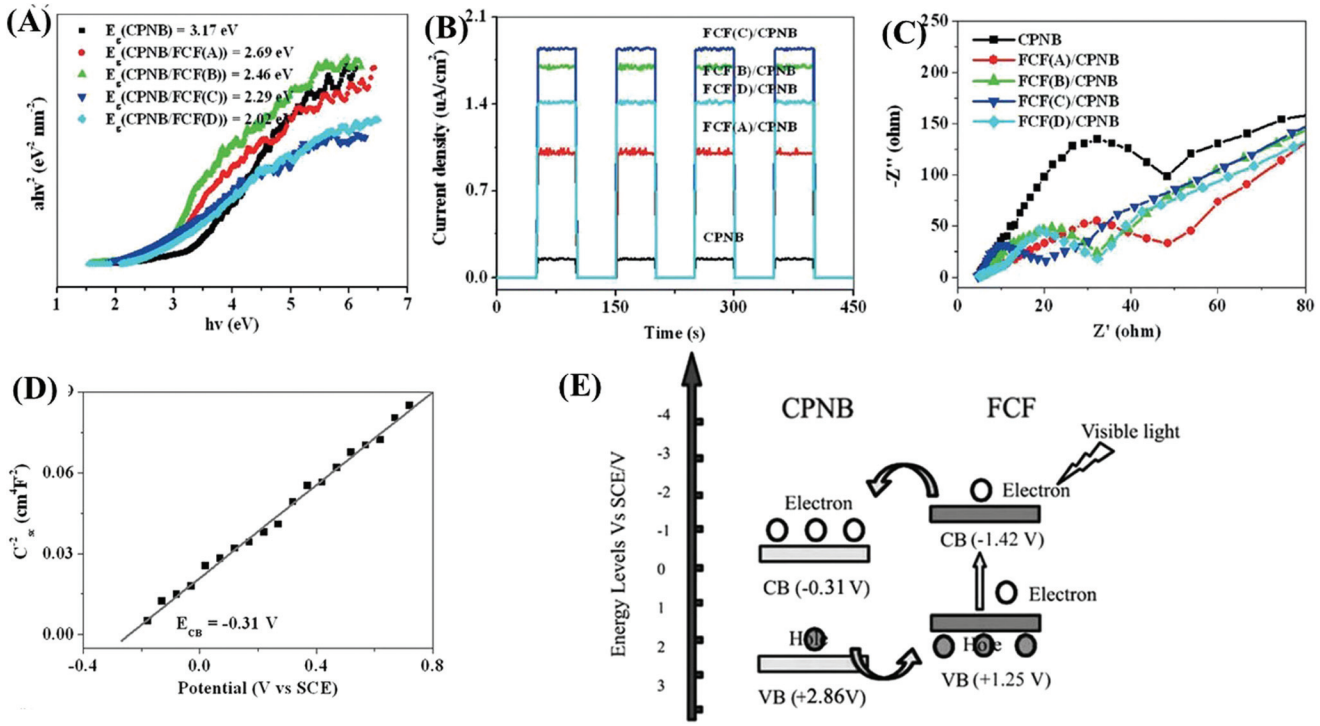

Fig. 24 Comparison between CPNB and CPNB/FCF: (A) Tauc plots; (B) photocurrent response; (C) EIS Nyquist plots; (D) Mott–Schottky plot of CPNB; (E) proposed photocatalytic mechanism for CPNB/FCF. Adapted with permission from ref. 158, © 2015 Wiley-VCH.

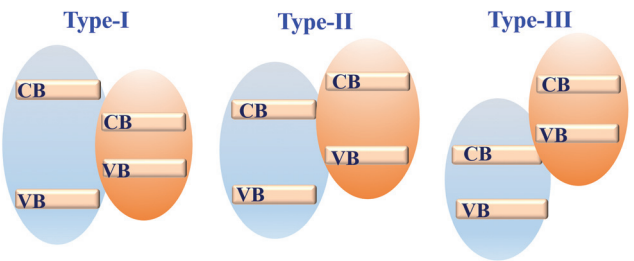

Fig. 25 Three types of semiconductor heterojunctions. Type-I: straddling gap; type-II: staggered gap; type-III: broken gap.

gradually tested. The as-prepared MOF-based binary composites for the photocatalytic removal of environmental pollutants are summarized in Table 5. Except for MIL-53(Fe) with 1D lozenge-shaped channels and ultra-small surface area (<100 m^2 g^{-1}),[165–167] the coupling of other MOFs with a photoactive semiconductor led to a decreased surface area relative to pristine MOFs. Due to the comprehensive effects of various factors, including light absorption, charge generation, separation and transfer properties, the photocatalytic performance for environmental remediation can be increased.

For example, Ag_3PO_4@NH_2-MIL-125(Ti) was fabricated *via* a simple drying process.[208] As shown in Fig. 26A, Ag_3PO_4 nanoparticles (10 to 20 nm) were well-dispersed onto the surface of NH_2-MIL-125(Ti). The band structures of Ag_3PO_4 and NH_2-MIL-125(Ti) are illustrated in Fig. 26B, which indicates a Type I heterojunction. The as-prepared binary composite exhibited significantly enhanced performance (Fig. 26C) as well as good stability for MB degradation under visible light irradiation. Similarly, $WO_{2.72}$/UiO-66(Zr)[198] and Co,Ni-MOF/$BiFeO_3$[213] composites were also prepared and displayed characteristic properties of Type I heterojunctions.

Due to the water-stability of UiO-66(Zr), the UiO-66(Zr)-based composites were competitive candidates for wastewater treatment. For example, BiOBr/UiO-66(Zr) was prepared by incorporating UV-active UiO-66 (E_g = 4.0 eV) with visible light-active BiOBr (E_g = 2.8 eV) through a convenient solution method.[195] The as-prepared BiOBr/UiO-66 composite displayed enhanced photocatalytic activity for RhB degradation, as well as good stability in cyclic runs. After 15 min visible light irradiation, the removal efficiency of RhB was in the order of BiOBr/UiO-66 (100%) > BiOBr (84%) > UiO-66(Zr) (<5%). Furthermore, amine-functionalized UiO-66 was also applied to couple with BiOBr.[196] As shown in Fig. 27A, a flower-like BiOBr/NH_2-UiO-66(Zr) composite with a three-dimensional structure was fabricated. Intensive characterization by SEM, XRD and XPS has been carried out to investigate the structure properties. Results indicated that BiOBr nanoplates successfully grew on the surface of NH_2-UiO-66(Zr) with an intimate interaction. The recombination of charge carriers can be inhibited, which was evidenced by the PL spectra. For the photocatalytic degradation of a typical fluoroquinolone antibiotics (norfloxacin), the as-prepared BiOBr/NH_2-UiO-66(Zr) composites with different loading amounts all displayed enhanced

Table 5 MOF-based binary composites for the photocatalytic removal of environmental pollutants

Composites	S_{BET} variation[a] ($m^2\ g^{-1}$)	Pollutant	$C_{pollutant}$ ($mg\ L^{-1}$)	$C_{catalyst}$ ($g\ L^{-1}$)	Time (min)	η variation[b] (%)	Ref.
Coupled with Zn-MOFs							
BiOBr/MOF-5(IL)	915 → NA	MO	10	0.4	150	<2 → 88	168
TiO_2@ZIF-8	NA	MB	1.6	NA	120	54 → 88[d]	169
		RhB	2.4	NA	120	50 → 65[d]	
Bi_2MoO_6/ZIF-8	NA	MB	20	0.25	100	34 → 67	170
3D MoO_3@ZIF-8	1531 → 213	Cr(VI)	15	0.5	40	13 → 96	171
MoO_3-NPs/ZIF-8	1710 → 1529	MB	10	0.25	180	59 → 82[d]	172
$BiFeO_3$/ZIF-8	NA	MB	20	0.375	100	50 → 93	173
ZIF-8@$BiVO_4$	1180 → 249	MB	20	0.25	130	NA → 81[d]	174
Bi_2S_3@ZIF-8	1297 → 821	RhB	10	0.4	90	NA → 97	175
$Cd_{0.5}Zn_{0.5}S$@ZIF-8	1190 → 174	Cr(VI)	20	1	10	5 → 100	176
Coupled with Fe-MOFs							
Fe_2O_3/MIL-53(Fe)	48 → 47	MB	10	0.2	120	31 → 48	177
WO_3/MIL-53(Fe)	57 → 97	Cr(VI)	30	1.5	240	70 → 94[d]	167
		2,4-D	30	1.5	240	58 → 100[d]	
Ag_3PO_4/MIL-53(Fe)	9 → 16	TC	20	0.5	60	26 → 94	165
AgI/MIL-53(Fe)	NA	RhB	4.8	0.3	45	86 → 99	166
CdS/MIL-53(Fe)	NA	RhB	10	1.0	120	5 → 86	178
1T-MoS_2/MIL-53(Fe)	21 → 337	IBP[c]	10	0.4	120	50 → 100	179
MIL-53(Fe)/SnS	56 → 34	Cr(VI)	20	1.0	60	16 → 71	180
TiO_2@NH_2-MIL-88B(Fe)	34 → 19	Cr(VI)[e]	10.4	0.5	35	85 → 99[d]	181
TiO_2NS@MIL-100(Fe)	1670 → 474	MB[c]	50	0.2	60	NA → 96	182
MIL-100(Fe)/TiO_2	1189 → 307	TC[c]	100	0.05	60	NA → 86[d]	183
		Cr(VI)	10	0.05	60	NA → 50[d]	
N-TiO_2QDs/MIL-100(Fe)	1556 → 1413	MB	16	0.1	140	90 → 99	184
		RhB	24	0.1	140	83 → 94	
M.MIL-100(Fe)@ZnO	766 → 654	Phenol	5	0.2	120	43 → 85	185
		BPA	5	0.2	120	35 → 89	
		Atrazine	5	0.2	120	30 → 70	
Bi_2WO_6/MIL-100(Fe)	1370 → 140	SA[c]	10	1.0	50	35 → 95	186
Bi_2MoO_6/MIL-100(Fe)	NA → 110	RhB	10	1.0	120	51 → 88	187
MIL-100(Fe)@Bi_2S_3	1394 → 404	RhB	10	0.5	60	70 → 94	188
M-MIL-101(Fe)/TiO_2	394 → 159	TC	20	1.0	80	74 → 92	189
Coupled with Cr-MOFs							
N-$K_2Ti_4O_9$/MIL-101(Cr)	2321 → 135	RhB	5	0.2	180	43 → 54[d]	190
WO_3@MIL-101(Cr)@WO_3	2480 → 1360	MB	30	NA	80	NA → 100	191
Coupled with Zr-MOFs							
Ag_2CO_3/UiO-66(Zr)	808 → 522	RhB	14.4	0.5	120	NA → 94	192
AgI/UiO-66(Zr)	808 → 289	RhB	14.4	0.5	60	NA → 100	193
N-$K_2Ti_4O_9$/NH_2-UiO-66(Zr)	NA	RhB	5	0.2	180	53 → 90[d]	194
		MB	5	0.2	180	NA → 94[d]	
		NR	5	0.2	180	NA → 91[d]	
BiOBr/UiO-66(Zr)	869 → 204	RhB	14.4	0.5	15	<5 → 98	195
BiOBr/NH_2-UiO-66(Zr)	NA	Noroxin	0.3	0.3	180	34 → 94[d]	196
α-Fe_2O_3@UiO-66(Zr)	1296 → 1204	MB	12.8	1.0	50	70 → 100	197
$WO_{2.72}$/UiO-66(Zr)	1099 → 187	MO	20	0.3	60	48 → 100	198
$BiVO_4$/UiO-66(Zr)	646 → 387	RhB	10	1.0	150	<10 → 100	199
Bi_2WO_6/UiO-66(Zr)	808 → 275	RhB	14.4	0.5	180	NA → 100	200
Bi_2MoO_6/UiO-66(Zr)	621 → 209	RhB	10	0.5	120	30 → 92	201
$ZnIn_2S_4$/UiO-66(Zr)	911 → 242	Cr(VI)	80	0.5	60	<5 → 99	202
		MO	20	0.17	180	49 → 98	
CdS@NH_2-UiO-66(Zr)	840 → 114	MG	20	0.2	30	16 → 100	203
Coupled with Ti-MOFs							
In_2S_3@MIL-125(Ti)	1548 → 304	TC	46	0.3	60	42 → 63	204
BiOBr/NH_2-MIL-125(Ti)	1012 → 8	RhB	20	0.2	100	41 → 98	205
		Phenol	20	0.2	150	NA → 24	
BiOI/NH_2-MIL-125(Ti)	NA	MO	20	1.0	120	22 → 93	206
NH_2-MIL-125(Ti)/BiOCl	770 → 46	TC	20	0.5	120	5 → 78	207
		BPA	10	0.5	240	NA → 65	
Ag_3PO_4/NH_2-MIL-125(Ti)	NA	MB	10	0.5	50	55 → 100	208
		RhB	10	0.5	180	50 → 94	
PHIK/NH_2-MIL-125(Ti)	1160 → 185	RhB	100	1.0	120	66 → 97[h]	209
CdTe QDs/NTU-9	1205 → 880	Rh6G	1.0	0.05	30	55 → 96[f]	210
Coupled with Cu-MOFs							
HKUST-1/$BiVO_4$	855 → 585	DB17	30	0.2	20	NA → 100[g]	211
		RB	30	0.2	20	NA → 99[g]	
$Cu_2(OH)PO_4$-HKUST-1	NA	Abamectin	30	0.4	20	NA → 100[g]	212
Coupled with other MOFs							

Table 5 *(Contd.)*

Composites	S_{BET} variation[a] ($m^2\ g^{-1}$)	Pollutant	$C_{pollutant}$ ($mg\ L^{-1}$)	$C_{catalyst}$ ($g\ L^{-1}$)	Time (min)	η variation[b] (%)	Ref.
Co,Ni-MOF/$BiFeO_3$	1058 → 895	MO	50	0.2	90	34 → 94	213
		4-NP	50	0.2	90	24 → 75	
Co,Ni-MOF/$CuWO_4$	1054 → 801	MB	10	0.2	135	32 → 98	214
		4-NP	10	0.2	105	24 → 81	
Ag_3PO_4@Co,Ni-MOF	NA	Phenol	40	1.0	16	<5 → 100	215
		BPA	40	1.0	20	<5 → 99	
BiOBr/CAU-17	NA	RhB	20	0.2	40	22 → 99	216

NA: no experimental data available. [a] S_{BET} variation indicates the surface area of MOFs before and after forming composites. [b] Removal efficiencies (η) for pollutants are used as received or estimated from the figures in the reference and presented in integer numbers; η variation indicates the performance of MOFs before and after forming composites. [c] Addition of H_2O_2. [d] UV-Vis light or simulated sunlight. [e] Addition of ammonium oxalate. [f] 500 nm monochromatic light. [g] Under the assistance of sonication. [h] 465 nm LED light.

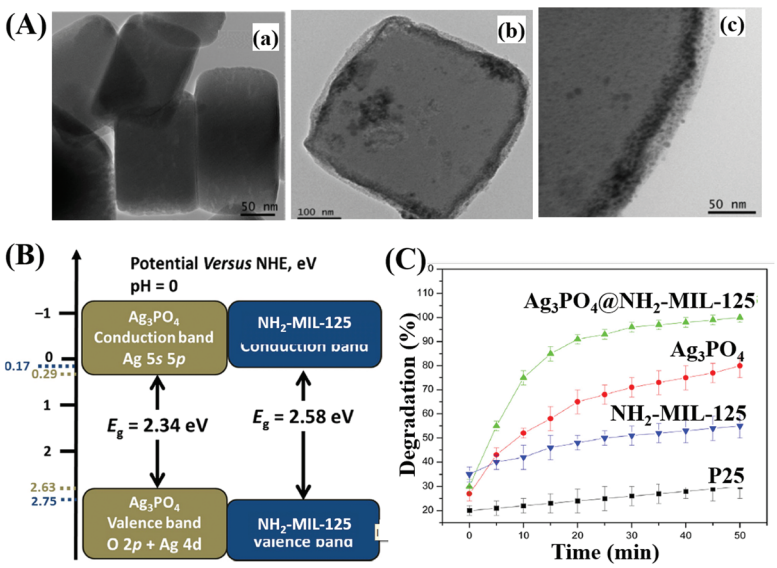

Fig. 26 (A) TEM images of NH_2-MIL-125(Ti) (a), Ag_3PO_4@NH_2-MIL-125(Ti) (b), and high magnification of Ag_3PO_4@NH_2-MIL-125(Ti) (c); (B) CB and VB positions of Ag_3PO_4 and NH_2-MIL-125 (Ti); (C) photocatalytic degradation of MB by different samples under visible light irradiation. Adapted with permission from ref. 208, © 2017 Elsevier B.V.

performance (Fig. 27B). The highest activity was achieved by BUN-20 with 20 wt% NH_2-UiO-66. Furthermore, trapping experiments were also performed to reveal the active species for norfloxacin degradation. Both the addition of an electron scavenger (HCOOH) and emptying of oxygen (N_2 purging) significantly inhibited the degradation dynamics. Thus, the dominant role of $O_2^{\bullet-}$ can be speculated since $O_2^{\bullet-}$ originated from the electron transfer to O_2. Besides, the secondary role of $HO^{\bullet}$ and h^+ can also be confirmed *via* the addition of the corresponding IPA and NaCl scavengers. Considering the band positions of independent BiOBr and NH_2-UiO-66(Zr), a Type II heterojunction[167,196,207] can be used to explain the charge transfer processes (Fig. 27C). It is thermodynamically feasible that the photogenerated electrons in the LUMO of NH_2-UiO-66 (Zr) (−0.6 eV) can be transferred to the CB of BiOBr (+0.32 eV). Meanwhile, holes (h^+) in the VB of BiOBr (+3.02 eV) can be transferred to the HUMO of NH_2-UiO-66(Zr) (+2.22 eV). Moreover, the LUMO of NH_2-UiO-66(Zr) and the VB of BiOBr are energetic enough for reducing O_2 to $O_2^{\bullet-}$ and oxidizing HO- to $HO^{\bullet}$, respectively. The synergistic effect between BiOBr and NH_2-UiO-66(Zr) led to highly enhanced performance for norfloxacin degradation.

In addition to traditional Type II heterojunctions, novel MOF-based Z-scheme heterojunctions were recently reported.[165,167] For example, an Ag_3PO_4/MIL-53(Fe) composite was prepared through a simple *in situ* precipitation strategy. The as-prepared binary composite displayed enhanced photocatalytic performance for the degradation of multiple antibiotics such as tetracycline (TC), oxytetracycline (OTC), chlortetracycline (CTC) and deoxytetracycline (DCL). As shown in Fig. 28A, the optimized Ag_3PO_4/MIL-53(Fe) composite (APM-3) with a 1 : 3 mass ratio exhibited the highest activity for TC degradation. More importantly, the binary composite also displayed higher photostability and recyclability than pristine Ag_3PO_4 (Fig. 28B). After four cyclic runs for TC degradation, the loss of degradation efficiency using APM-3 was *ca.* 8%. Whereas, the value was *ca.* 25% using Ag_3PO_4. The instability of Ag_3PO_4 during the photocatalytic process was evidenced by

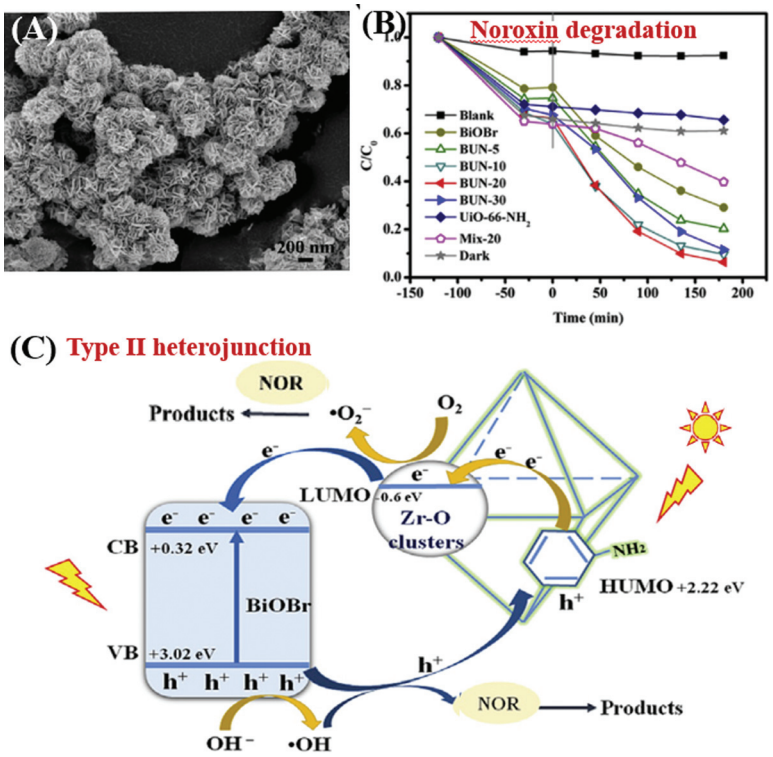

Fig. 27 (A) SEM image of BiOBr/NH_2-UiO-66(Zr); (B) photocatalytic degradation of Noroxin by different samples under simulated sunlight irradiation; (C) proposed mechanism for photocatalytic degradation of Noroxin by BiOBr/NH_2-UiO-66(Zr). Adapted with permission from ref. 196, © 2018 Elsevier Ltd.

the formation of metallic Ag. More obvious XRD signals of Ag (JCPDS card no. 65-2871) were observed in pristine Ag_3PO_4 relative to APM-3 (Fig. 28C). Interestingly, the formation of tiny metallic Ag may lead to a Z-scheme structure for charge transfer in the Ag_3PO_4/MIL-53(Fe) composite. As shown in Fig. 28D, the CB/LUMO positions of Ag_3PO_4 and MIL-53(Fe) matched well with typical Type II heterojunctions. In this mechanism, the electrons in the LUMO of MIL-53(Fe) (−0.41 eV) will flow into the CB of Ag_3PO_4 (+0.42 eV). Since the CB edge of Ag_3PO_4 is more positive than the redox potential of $O_2/O_2^{\bullet-}$ (−0.33 eV *vs.* NHE), the formation of $O_2^{\bullet-}$ was not feasible. Similarly, the HOMO position of MIL-53(Fe) (+2.33 eV) was not energetic enough to oxidize surface HO− into HO$^\bullet$ ($E_{HO-/HO\cdot}$ = +2.40 eV *vs.* NHE). However, strong signals of both HO$^\bullet$ and $O_2^{\bullet-}$ were detected by electron spin resonance (ESR) spectroscopy. Thus, the Type II heterojunction mechanism was not suitable for Ag_3PO_4/MIL-53(Fe). Since metallic Ag was detected during the photocatalytic process, a Z-scheme mechanism can well explain the above phenomena. As depicted in Fig. 28E, metallic Ag nanoparticles with an appropriate Fermi level can act as a bridge for electron transfer from the CB of Ag_3PO_4 to the HOMO of MIL-53(Fe). In this way, both the high reductive ability of MIL-53(Fe) and the oxidative ability of Ag_3PO_4 can be well maintained, leading to the generation of sufficient active species (HO$^\bullet$ and $O_2^{\bullet-}$).

Compared with Type I and Type II heterojunctions, there were very few reports of Type III heterojunctions for environmental photocatalysis. In 2016, Wang *et al.* reported the fabrication of core–shell In_2S_3@MIL-125(Ti) *via* a solvothermal method.[204] As shown in Fig. 29A, the band positions of In_2S_3 and MIL-125(Ti) matched well with Type III heterojunctions. Upon visible light irradiation, the photogenerated electrons in the CB of In_2S_3 will be transferred to the LUMO of MIL-125 (Ti), which finally led to the reduction of adsorbed O_2. Meanwhile, the corresponding h^+ left in the VB of In_2S_3 will oxidize water into O_2. Thus, increased separation of photogenerated charges can be achieved, which finally led to an enhanced degradation of TC (Fig. 29B). However, probably due to the low oxidizing ability of h^+ in In_2S_3, the degradation of TC on optimized In_2S_3@MIL-125(Ti) slows down with prolonged irradiation time. Besides, the cycling stability for TC degradation exhibited moderate loss (Fig. 29C).

3.7.2 Coupling with a metal free g-C_3N_4 semiconductor. Nonmetal g-C_3N_4 was a star photocatalyst due to its appealing electronic structure, low cost and high stability. The band gap of g-C_3N_4 was *ca.* 2.7 eV, indicating the light absorption edge into the visible region (up to 450 nm). Thus, coupling g-C_3N_4 with MOFs may lead to enhanced visible light response. As summarized in Table 6, many kinds of MOF-C_3N_4 binary composites have been fabricated and displayed superior photocatalytic activity. After coupling with g-C_3N_4, the BET specific surface area was decreased to different extends in most cases, indicating less surface active sites. Despite this, the negative effects by the decreased surface area can be offset by enhanced

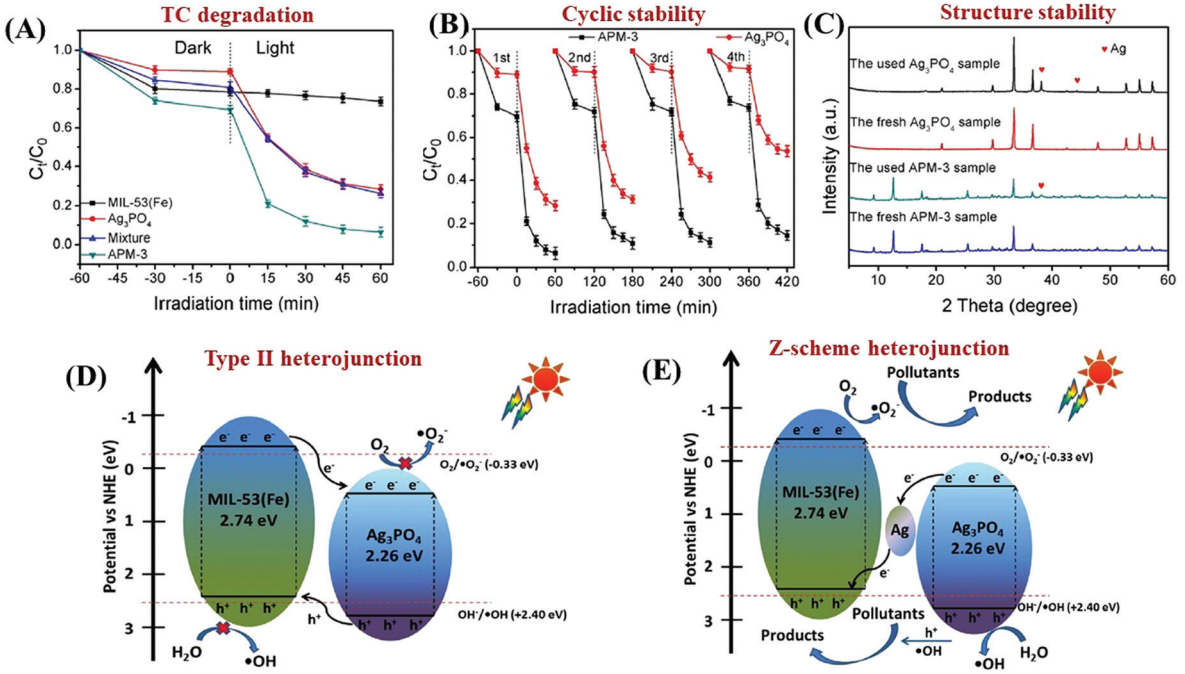

Fig. 28 (A) Photocatalytic degradation of TC by different samples under visible light irradiation; (B) cycling stability of Ag_3PO_4 and Ag_3PO_4/MIL-53 (Fe) composites for photocatalytic degradation of TC; (C) XRD patterns of Ag_3PO_4 and Ag_3PO_4/MIL-53(Fe) under different conditions; proposed mechanism for charge separation over Ag_3PO_4/MIL-53(Fe): (D) Traditional Type II heterojunction and (E) Z-scheme heterojunction. Adapted with permission from ref. 165, © 2018 Elsevier B.V.

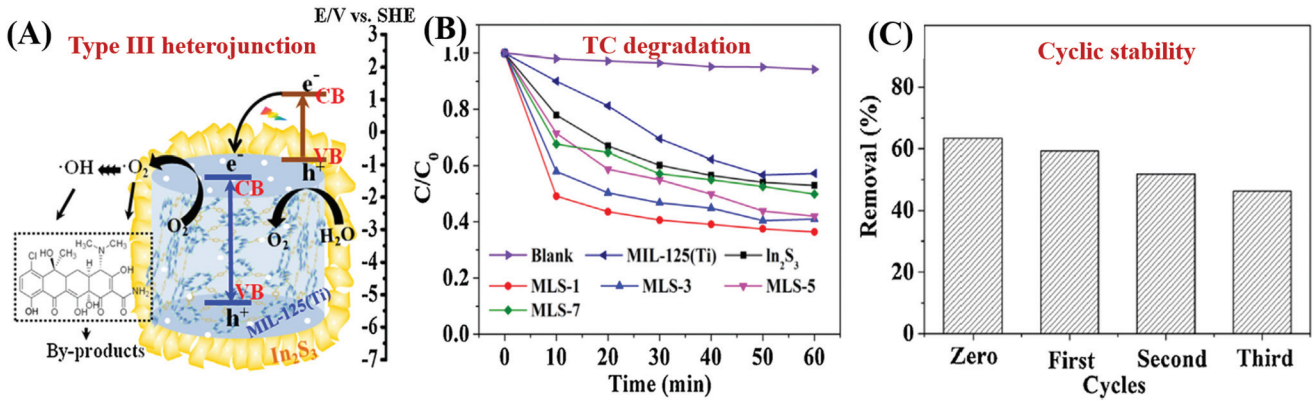

Fig. 29 (A) Proposed mechanism for the charge transfer processes in In_2S_3@MIL-125(Ti); (B) photocatalytic degradation of TC by different samples; (C) cycling stability of optimized In_2S_3@MIL-125(Ti) for TC degradation under visible light. Adapted with permission from ref. 204, © 2016 Elsevier.

visible light absorption, increased conductivity, more efficient charge separation and lower charge transfer resistance induced by g-C_3N_4.

For example, Wang's group reported the facile fabrication of a Type-I heterojunction between a novel Zn-MOF (BUC-21) and g-C_3N_4 through ball-milling. The as-prepared BUC-21/g-C_3N_4 composite displayed enhanced photocatalytic performance for Cr(VI) reduction. The radius of the EIS Nyquist plot for the BUC-21/g-C_3N_4 composite was smaller than either BUC-21 or g-C_3N_4 (Fig. 30A), indicating the lowest electron transfer impedance. Thus, for the reduction of Cr(VI) under simulated sunlight, BUC-21/g-C_3N_4 composites with different loading percentages of g-C_3N_4 displayed significantly enhanced performance (Fig. 30E). After 120 min light irradiation, only 13% and 18% Cr(VI) can be reduced by single BUC-21 and g-C_3N_4, respectively. Whereas, 100% reduction efficiency can be achieved by the BUC-21/g-C_3N_4 (B100G100) composite with 50 wt% g-C_3N_4. In order to further confirm the formation of heterojunctions, a mixture of BUC-21 and g-C_3N_4 with the same content as optimized BUC-21/g-C_3N_4 was also tested for Cr(VI) reduction. The value was *ca.* 52%, which was far less than the composite. For better understanding the interfacial

Table 6 MOF-C_3N_4 binary composites for the photocatalytic removal of environmental pollutants

MOFs	C_3N_4 (wt%)	S_{BET} variation[a] ($m^2\ g^{-1}$)	Pollutant	$C_{pollutant}$ ($mg\ L^{-1}$)	$C_{catalyst}$ ($g\ L^{-1}$)	Time (min)	η variation[b] (%)	Ref.
Coupled with Zn-MOFs								
ZIF-8(Zn)	60%	1318 → 555	TC	89	0.1	60	45 → 91[c]	217
ZIF-8(Zn)	97%	NA	TC	20	0.5	30	NA → 74	218
			RhB	10	0.5	75	NA → 99	
			MO	50	0.5	180	NA → 86	
BUC-21(Zn)	50%	1 → 12	Cr(VI)	10	0.25	120	13 → 100	219
Coupled with Al-MOFs								
MIL-53(Al)	20%	NA → 44	RhB	10	0.5	75	NA → 100[c]	220
Coupled with Fe-MOFs								
MIL-53(Fe)	3%	21 → 19	Cr(VI)	10	0.4	180	52 → 100	221
NH_2-MIL-53(Fe)	50%[e]	NA	TC[d]	50	0.4	30	82 → 90	222
			CBZ[d]	50	0.4	150	52 → 78	
			BPA[d]	50	0.4	10	NA → 100	
			PNP[d]	50	0.4	30	NA → 100	
MIL-88A(Fe)	90%	22 → 38	RhB	10	1.0	30	<5 → 100	223
			Phenol	10	1.0	120	<5 → 26	
			TC	10	1.0	120	<5 → 46	
MIL-88A(Fe)	NA	24 → 16	MB	NA	1.0	120	25 → 75	224
NH_2-MIL-88B(Fe)	10%	NA	MB[d]	30	1.0	120	57 → 100	225
MIL-100(Fe)	1%[f]	1225 → 1096	RhB[d]	50	0.2	240	68 → 100	226
MIL-100(Fe)	80%	NA	Cr(VI)	10	0.5	80	76 → 98[c]	227
			DS[d]	32	0.5	30	NA → 100[c]	
MIL-100(Fe)	9%[g]	1556 → 1252	RhB	10	1	200	36 → 87	228
			MB	10	1	200	27 → 82	
			Pyridine	560[h]	5	360	53 → 76	
MIL-101(Fe)	2%	NA	BPA[i]	10	0.5	60	51 → 100	229
NH_2-MIL-101(Fe)	NA	NA	Cr(VI)	10	0.5	60	56 → 100	230
Coupled with Zr-MOFs								
UiO-66(Zr)	50%	1335 → 1133	RhB	10	0.4	180	19 → 93	231
UiO-66(Zr)	50%	972 → 384	MB	10	0.25	240	48 → 100	232
PCN-222(Zr)	99%	NA → 36	RhB	20	0.1	120	78 → 98	233
			Ofloxacin	20	0.1	200	72 → 96	
Coupled with Ti-MOFs								
MIL-125(Ti)	7%	1548 → 328	RhB	50	0.4	60	15 → 95	234
NH_2-MIL-125(Ti)	30%	1535 → 830	4-NP	NA	NA	240	55 → 75	235
Coupled with Cu-MOFs								
HKUST-1	25%[j]	1084 → 392	DMCP	NA	NA	1440	NA	236
HKUST-1/fiber	25%	1084 → 392	DMCP	NA	NA	1440	NA	237

NA: no experimental data available. [a] S_{BET} variation indicates the surface area of MOFs before and after forming composites. [b] Removal efficiencies (η) for pollutants are used as received or estimated from the figures in the reference and presented in integer numbers; η variation indicates the performance of MOFs before and after forming composites. [c] UV-Vis light or sunlight. [d] Addition of H_2O_2. [e] g-C_3N_4 doped with pyromellitic diimide (PDI). [f] g-C_3N_4 nanosheets. [g] Protonated g-C_3N_4. [h] $\mu g\ g^{-1}$. [i] Addition of PS. [j] Oxidized g-C_3N_4.

charge transfer mechanism, the band positions of pristine BUC-21 and g-C_3N_4 were estimated from typical Mott–Schottky measurements. As illustrated in Fig. 30B and C, the flat band potentials were *ca.* −1.24 V and −1.10 V (*vs.* Ag/AgCl) for BUC-21 and g-C_3N_4, corresponding to −1.04 V and −0.90 V (*vs.* NHE), respectively. Besides, the positive slope of the Mott–Schottky plot indicated an n-type semiconductor. Therefore, the VB position can be calculated from the equation: $E_g = E_{VB} - E_{CB}$. As shown in Fig. 30D, a Type-I heterojunction can be deduced from the BUC-21/g-C_3N_4 composite. In addition to UV active BUC-21, Type-I heterojunctions can also be achieved when visible light-active Fe-MOFs were coupled with g-C_3N_4.[224–226,228] For example, MIL-100(Fe) with a tricarboxylate linker was reported to be very stable with a relatively high BET surface area (>1000 $m^2\ g^{-1}$).[5] The LUMO and HOMO positions of MIL-100(Fe) were estimated to be −0.24 V and 1.73 V (*vs.* Ag/AgCl) at pH 7, respectively.[226] The corresponding CB and VB values were −0.92 V and 1.96 V (*vs.* Ag/AgCl) for g-C_3N_4 nanosheets. The MIL-100(Fe)/g-C_3N_4 composite with a Type I heterojunction exhibited enhanced activity for RhB degradation. After 240 min visible light irradiation, the degradation efficiency increased from 68% on pristine MIL-100(Fe) to 100% on MIL-100(Fe)/g-C_3N_4.

In addition to Type-I heterojunctions, UV-active UiO-66 (Zr),[231,232] MIL-125(Ti)[234,235] and visible light-active Fe-MOFs[221,224,227,229] were also reported to form Type II heterojunctions with g-C_3N_4. For example, a g-C_3N_4/MIL-101(Fe) composite was fabricated for the degradation of bisphenol A (BPA) with persulfate (PS) under visible light. Combined with the results in the Mott–Schottky plots (measuring flat band potential) and UV-Vis DRS spectra (measuring band gap E_g), the CB and VB positions of g-C_3N_4 were estimated to be −1.1 V and 1.7 V (*vs.* SCE), respectively. The corresponding LUMO and HOMO values were −0.7 V and 1.9 V (*vs.* SCE) for MIL-101(Fe), respectively. As shown in Fig. 31A, under visible light irradiation, the photogenerated electrons (e^-) will transfer

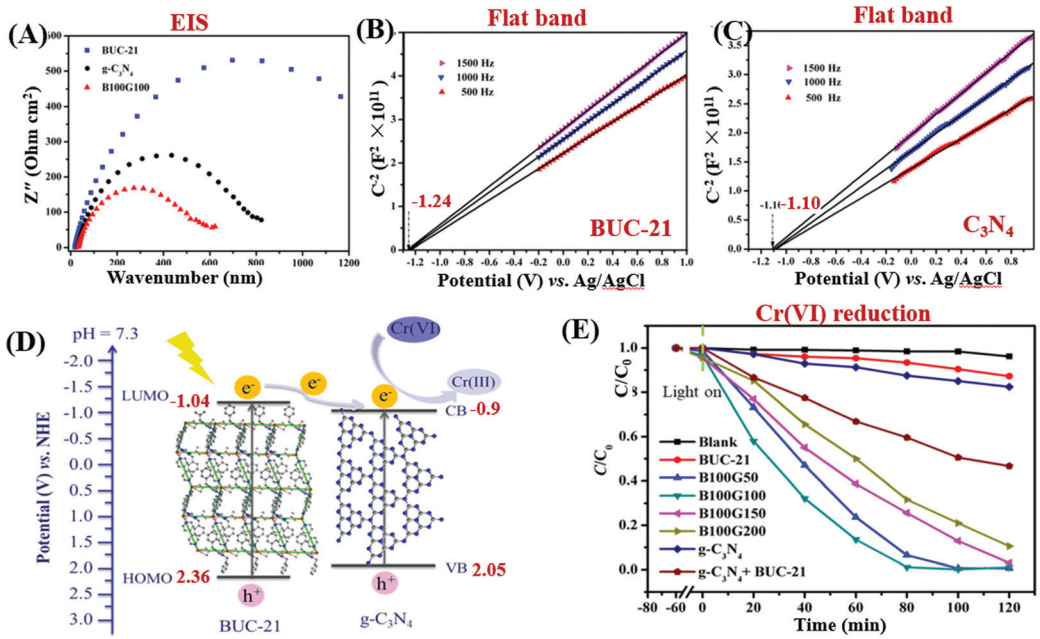

Fig. 30 (A) EIS Nyquist plots of different samples; (B) Mott–Schottky plots of BUC-21; (C) Mott–Schottky plots of g-C_3N_4; (D) proposed mechanism for photogenerated electron transfer by the BUC-21/g-C_3N_4 heterojunction; (E) photocatalytic reduction of Cr(VI) by different samples. Adapted with permission from ref. 219, © 2018 John Wiley & Sons, Ltd.

from the CB of g-C_3N_4 to the LUMO of MIL-101(Fe). Meanwhile, holes (h^+) will transfer from the HOMO of MIL-101 (Fe) to the VB of g-C_3N_4. In this way, efficient separation of photogenerated charges can be achieved. Thus, for the visible light-induced degradation of BPA, the g-C_3N_4/MIL-101(Fe) composite displayed dramatically enhanced performance relative to single MIL-101(Fe) and g-C_3N_4 (Fig. 31B). The electron transfer process and the reactive centers were further investigated by ESR analysis. As shown in Fig. 31C, an obvious ESR signal can be observed under dark conditions in MIL-101(Fe), which was ascribed to Fe^{3+} in FeO_6. Subsequently, this signal can be totally quenched under visible light irradiation, indicating the disappearance of Fe^{3+}. Due to the presence of extensive Fe–O clusters, which can be directly excited by visible light, the charge transfer from O^{2-} to Fe^{3+} will lead to the reduction of Fe^{3+} to Fe^{2+}. Interestingly, after the addition of PS, the ESR signal of Fe^{3+} can be regenerated, which may be originated from the oxidation of Fe^{2+} to Fe^{3+} by PS. Thus, it can be deduced that the active sites for PS activation were metal centers (Fe) in the network of MIL-101(Fe). Besides, stronger signals of DMPO–$HO^{\bullet}$ and DMPO–$O_2^{\bullet-}$ were also observed in the g-C_3N_4/MIL-101(Fe) composite relative to the single ones. The oxidation of H_2O/HO– by $SO_4^{\bullet-}$ led to the production of $HO^{\bullet}$. Thus, all the active species together boosted the degradation of BPA.

A direct Z-scheme heterojunction was also reported in the fabrication of a MIL-88A(Fe)/g-C_3N_4 composite.[223] The introduction of MIL-88A(Fe) can significantly promote the separation of photogenerated charges. For example, lower PL intensity, higher photocurrent response and lower charge transfer resistance were observed on MIL-88A(Fe)/g-C_3N_4 relative to single components. Therefore, for the photocatalytic degradation of colorful RhB dye and colorless organic pollutants (phenol and tetracycline), the binary composite exhibited excellent performance. Under visible light irradiation, the estimated rate constant for RhB was *ca.* 0.16 min^{-1}, which was *ca.* 253 and 5 times that for MIL-88A and g-C_3N_4, respectively.

3.8 MOF/COF coupling

During the past few decades, great progress has been achieved in the modification of MOFs. Among the various modification strategies, coupling MOFs with other MOFs may possess the merits of individual MOFs and bring in new properties. For example, MOF–MOF hybrid materials with core–shell,[238–240] Janus[241,242] and hierarchical structures[243,244] have been fabricated and applied in many fields, such as catalysis,[245] gas detection[246] and chemical/biological sensing.[247] Since photoactive MOFs possess semiconductor-like behavior, the coupling of different MOFs with matched HOMO–LUMO positions may also lead to the formation of heterojunctions, which subsequently promoted the separation of photogenerated charges as well as photocatalytic performance.[248–252] For example, hierarchical MIL-101(Cr)@NH_2-MIL-125(Ti) hybrids were developed *via* an internal extended growth method, which displayed enhanced performance for Cr(VI) reduction under visible light.[248] PCN-222/MOF-545 with porphyrin functionality, high porosity and exceptional stability was prepared and applied for the selective degradation of a mustard-gas simulant (2-chloroethyl ethyl sulfide) to nontoxic 2-chloroethyl ethyl sulfoxide.[251] As for Fe-MOFs with strong visible light absorption, MIL-100(Fe)/MIL-53(Fe) composites with Type II heterojunctions were fabricated *via* electrostatic interaction with each

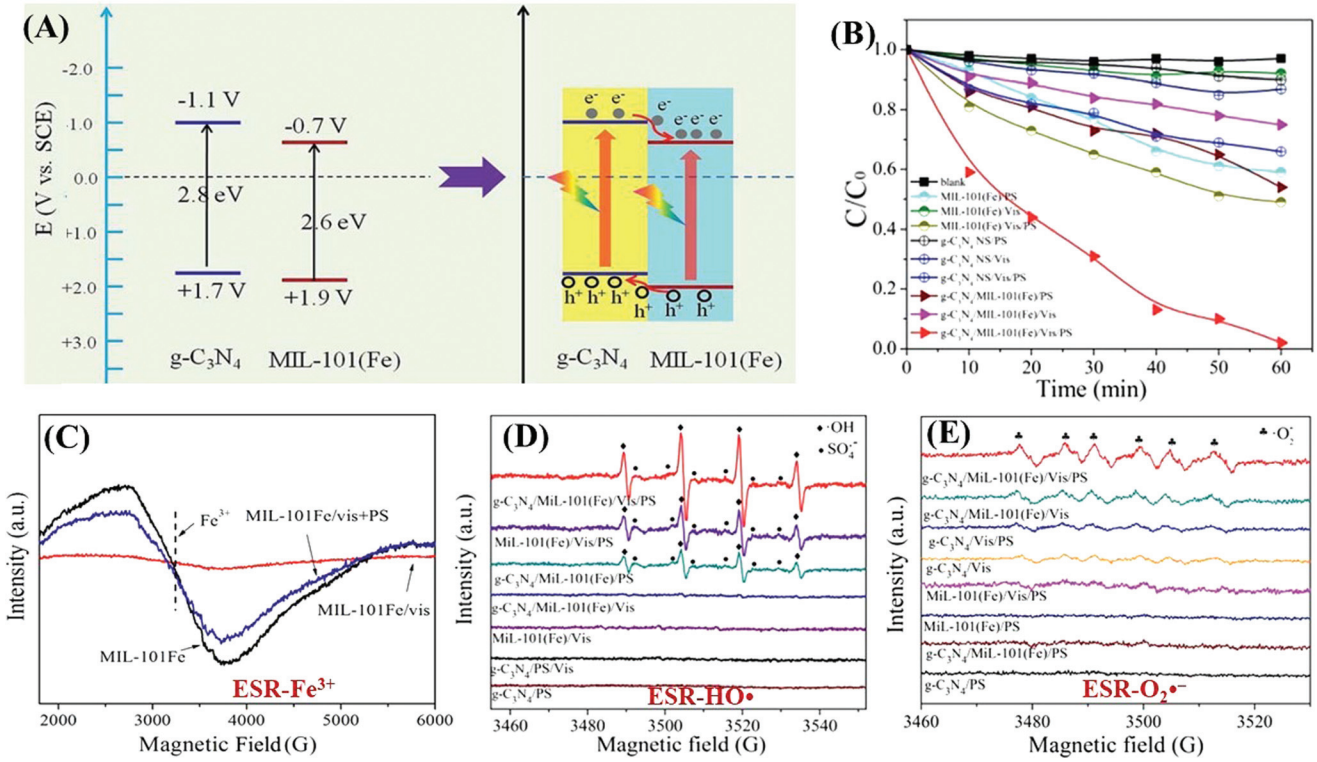

Fig. 31 (A) Schematic diagram of the band structure and charge transfer between MIL-101(Fe) and g-C_3N_4; (B) visible light-induced photocatalytic degradation of BPA under different conditions; (C) ESR spectra of Fe^{3+} in MIL-101(Fe) under different conditions; ESR signals of (D) DMPO–$HO^{\bullet}$ and (E) DMPO–$O_2^{\bullet-}$ in different photocatalytic systems. Adapted with permission from ref. 229, @ 2018 The Royal Society of Chemistry.

other. For the photocatalytic degradation of microcystin-LR (MC-LR), the hybrid material displayed enhanced activity compared to single MIL-53(Fe) and MIL-100(Fe) (Fig. 32A).[253] More importantly, the leaching of Fe^{3+} was significantly suppressed in hybrid MOFs (Fig. 32B). The reason may be ascribed to the electrostatic attraction effect between the two kinds of Fe-MOFs, since the surface of MIL-101 and MIL-53 was negatively and positively charged (at pH 6), respectively. Considering the matched LUMO and HOMO positions, more efficient charge separation can be anticipated (Fig. 32C). Thus, the complete degradation of MC-LR (4.5 mg L^{-1}) can be achieved at a very low dosage (0.02 g L^{-1}) of MIL-100/MIL-53 (Fe).

Similar to MOFs, metal-free covalent organic frameworks (COFs) are another kind of porous crystalline material, which have recently attracted increasing attention in photocatalysis.[254–256] Moreover, MOF–COF hybrid photocatalysts have also been developed.[257,258] For example, a core–shell NH_2-MIL-68(In)@TPA-COF with high crystallinity and hierarchical porosity was fabricated according to the procedure depicted in Fig. 33A.[257] The growth of a sheet-like TPA-COF on the surface of rod-like NH_2-MIL-68(In) can be obviously observed (Fig. 33B). Besides, the incorporation of the TPA-COF was further verified by XRD (Fig. 33C) and FT-IR analysis. Since the TPA-COF (2.32 eV) has a narrower band gap than NH_2-MIL-68(In) (2.82 eV), the MOF–COF hybridization led to an even smaller band gap (Fig. 33D), corresponding to more efficient utilization of visible light. Besides, due to the introduction of the TPA-COF (1136 m^2 g^{-1}), the BET surface area increased from 451 m^2 g^{-1} for NH_2-MIL-68(In) to 539 m^2 g^{-1} for the hybrid material. Thus, for the photocatalytic degradation of RhB, the NH_2-MIL-68(In)@TPA-COF hybrid displayed enhanced activity.

Recently, a series of covalently integrated MOF/COF composites with direct Z-scheme heterojunctions were also synthesized *via* a facile one-pot procedure, such as NH_2-MIL-125(Ti)/TTB-TTA, NH_2-MIL-53(Al)/TTB-TTA and NH_2-UiO-66(Zr)/TTB-TTA.[258] Due to well-matched HOMO–LUMO positions and increased separation of charge carriers across the heterojunction interface, significantly enhanced performance can be observed for the photocatalytic degradation of phenol and MO. Besides, the NH_2-MIL-125(Ti)/TTB-TTA composite with the highest activity became extremely stable after the incorporation of the TTB-TTA COF. Thus, the hybridization of MOFs with metal free COFs will be very attractive due to the formation of heterojunctions, retention of high surface area and structural stability.

3.9 Hybrid modification strategies

As described above, many single strategies have been reported to modify MOFs for enhanced photocatalytic performance.

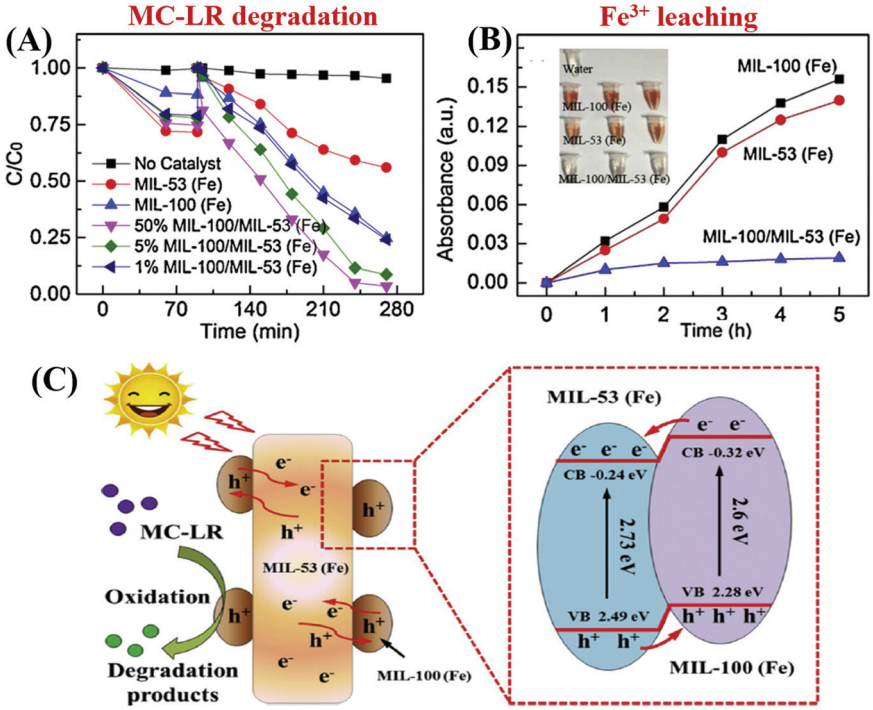

Fig. 32 (A) Photocatalytic degradation of MC-LR by different samples under visible light; (B) comparison of Fe(III) ion leaching from MIL-53 (Fe), MIL-100(Fe) and MIL-100(Fe)/MIL-53(Fe), inset: the photo of the aqueous solution during the photocatalytic process; (B) proposed mechanism for charge separation and MC-LR degradation by optimized MIL-100(Fe)/MIL-53(Fe) under visible light. Adapted with permission from ref. 253, © 2019 Elsevier.

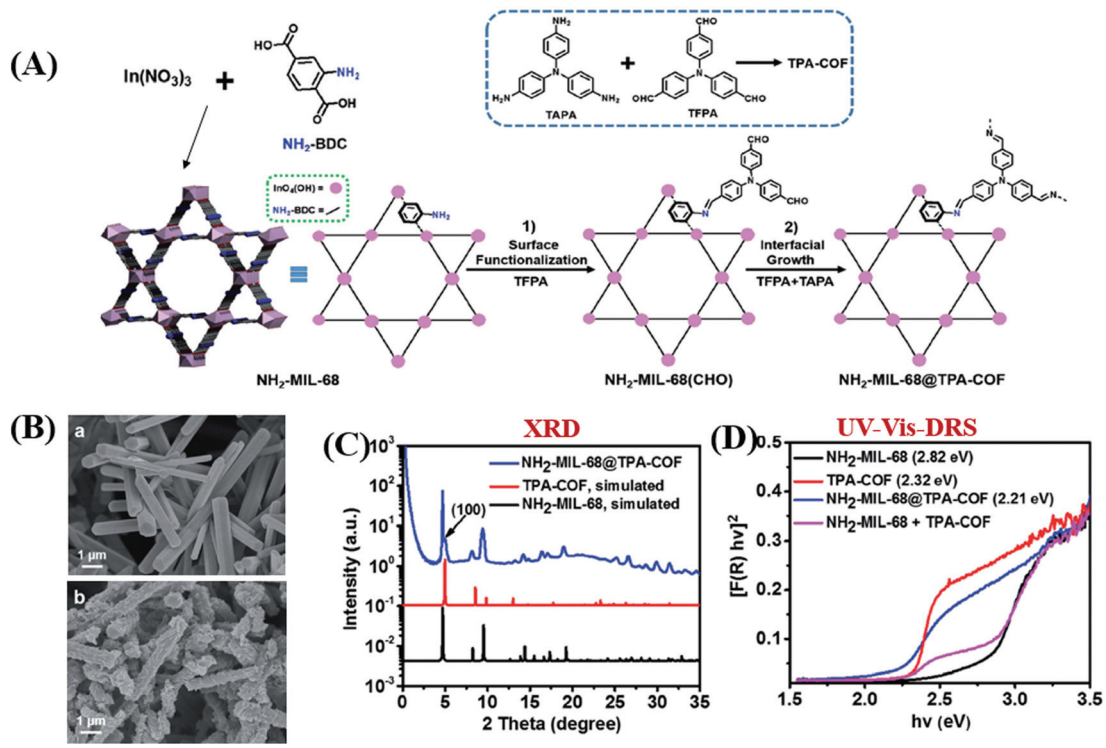

Fig. 33 (A) Schematic illustrations for the fabrication of the NH_2-MIL-68(In)@TPA-COF; (B) SEM images of (a) NH_2-MIL-68(In) and (b) NH_2-MIL-68 (In)@TPA-COF; (C) XRD patterns and (D) UV-Vis-DRS of different samples. Adapted with permission from ref. 257, © 2017 WILEY-VCH.

Each strategy has its own merits and limitations. For better utilization of the merits, proper combination of different strategies may lead to a synergistic effect.

As listed in Table 7, many hybrid modification strategies were established and displayed further enhanced photocatalytic performance relative to single strategies. For example, MOFs can be co-modified using MNPs and photoactive semiconductors, MNPs and conducting carbon materials, conducting carbon materials and photoactive semiconductors, *etc*. Besides, different photoactive semiconductors were also coupled with MOFs constructing multi-heterojunctions for more efficient charge separation.

Among the reported hybrid modification strategies, co-modification of MOFs using MNPs and photoactive semiconductors has been frequently reported. In particular, plasmonic Ag nanoparticles were competitive in comparison with other noble metals (such as Au, Pt and Pd) due to lower price. Until now, various kinds of MOFs (such as ZIF-8, MIL-Fe, MIL-Ti and HKUST) have been co-modified using Ag nanoparticles and semiconductors for environmental photocatalysis. For example, plasmonic Ag/AgCl and spindle-shaped MIL-88A(Fe) were integrated forming an Ag/AgCl@MIL-88A(Fe) (denoted as ACMA) ternary composite *via* a one-pot solvothermal method.[265] As shown in Fig. 34A, Ag/AgCl nanoparticles were uniformly anchored on the surface of spindle-shaped MIL-88A(Fe) microrods. The presence of metallic Ag was further verified by XRD analysis (Fig. 34B) and XPS investigation. The flat-band potential of ACMA was estimated to be −0.75 V *via* Mott–Schottky plot measurements.[290] Thus, the electron transfer from the CB of ACMA to O_2 forming reactive $O_2^{\bullet-}$ (0.13 eV) was thermodynamically feasible. For the photocatalytic degradation of ibuprofen (IBP), the Ag/AgCl@MIL-88A(Fe) composite exhibited significantly enhanced performance relative to Ag/AgCl and MIL-88A(Fe). The ternary composite was optimized with an Fe : Ag molar ratio of 2 : 1 in the initial preparation procedure. Furthermore, trapping experiments were carried out to investigate possible active species involved in the degradation of IBP by optimal ACMA-2. The addition of $O_2^{\bullet-}$ (benzoquinone), h^+ (EDTA-2Na) and e^- ($AgNO_3$) scavengers all inhibited the degradation dynamics, while the $HO^\bullet$ scavenger (IPA) had negligible influence. Thus, it can be deduced that $O_2^{\bullet-}$, h^+ and e^- play dominant roles in IPA degradation.[291] The production of $HO^\bullet$ ($E_{HO^-/HO^\bullet}$ = 2.38 V *vs*. NHE)[59,290] was thermodynamically infeasible due to weak oxidative ability (Fig. 34C). The degradation products were further detected. As depicted in Fig. 34D, due to the combined effect of $O_2^{\bullet-}$, h^+ and e^-, the degradation of IBP started from decarboxylation (by-products 1 and 4) and direct loss of functional groups (by-products 2, 3 and 5). The subsequent ring opening process led to the formation of HCOOH and CH_3COOH, which finally were mineralized into CO_2 and H_2O.

The merits of MNPs and conducting carbon materials can also be combined *via* co-modification. For example, MIL-125 (Ti) was modified with both Ag nanoparticles and rGO. As shown in Fig. 35A–C, bipyramid-like MIL-125(Ti) was enwrapped with rGO and Ag nanoparticles *via* one-pot self-assembly and a photoreduction method. The BET surface area slightly decreased from 755 $m^2\ g^{-1}$ for pristine MIL-125(Ti) to 730 $m^2\ g^{-1}$ for Ag/rGO/MIL-125(Ti) with negligible influence on the average pore diameter (2.2 nm *vs*. 2.3 nm), indicating the maintenance of the microporous structure. Besides, the presence of Ag nanoparticles and rGO can promote the separation of photogenerated charges, which was elucidated by PL spectra. Thus, under visible light irradiation, Ag can be excited to generate e^-–h^+ pairs due to the plasmonic effect (Fig. 35D). Due to the presence of rGO, the electrons can be more easily transferred to the Ti^{4+} metal center in MIL-125(Ti). The reduced intermediate Ti^{3+} will be re-oxidized by O_2 generating reactive $O_2^{\bullet-}$. rGO can also facilitate the interfacial electron transfer from Ag plasma to O_2. Meanwhile, $HO^\bullet$ can be generated by capturing h^+. Thus, due to the formation of the above active species, the photocatalytic performance for RhB degradation was accelerated on co-modified MIL-125(Ti) relative to single strategy modified MOFs. The rate constant was in the order of Ag/MIL-125(Ti) (0.052 min^{-1}) < rGO/MIL-125(Ti) (0.0595 min^{-1}) < Ag/rGO/MIL-125(Ti) (0.0644 min^{-1}).

Generally, the starting point of most hybrid modification strategies is focused on the formation, separation and transfer of charge carriers, which finally led to enhanced performance for the removal of pollutants. Whereas, the design of an appropriate modification strategy according to the characteristics of target pollutants may be a more promising way. For example, for efficient reduction of Cr(VI) (in the form of anionic $Cr_2O_7^{2-}$ at neutral pH), a visible light-harvesting unit (porphyrin) and a Cr(VI) adsorption site (CH_3^+) were simultaneous integrated into single MOFs (UiO-66). As illustrated in Fig. 36A, $H_2TCPP\subset(I^-)$ Meim-UiO-66 (I^- as a mobile counter anion) was fabricated *via* sequential mixed-ligand and ionization routes. The incorporation of the H_2TCPP ligand with the porphyrin unit could extend the absorption of UiO-66 from the UV to visible region (Fig. 36B). Meanwhile, the cationic struts could lead to enhanced adsorption of anionic $Cr_2O_7^{2-}$. Besides, the generation, separation and transfer of charge carriers in UiO-66 were also increased after co-modification. Furthermore, the electron transfer from excited porphyrin to Zr^{4+} centers can be confirmed from the greatly enhanced ESR signals (g = 2.003) under visible light (Fig. 36C). Time-resolved PL spectra were also used to track the photoexcited carrier in $H_2TCPP\subset(I^-)$ Meim-UiO-66 (Fig. 36D). After the *in situ* addition of Cr(VI), the long time constant (τ_2) totally disappeared, indicating fast transfer of electrons from H_2TCPP to Cr(VI). Thus, due to the above synergistic effect, the photocatalytic reduction of Cr(VI) was significantly boosted (Fig. 36E). After 30 min visible light irradiation, 100 mg L^{-1} Cr(VI) can be completely removed *via* adsorption and photoreduction by 0.25 g L^{-1} $H_2TCPP\subset(I^-)$ Meim-UiO-66. Herein, the concentration of Cr(VI) was far higher than that of most studies (10 mg L^{-1}). In other words, the rate of Cr(VI) reduction in the present system was 13.3 $mg_{Cr(VI)}\ g_{catalyst}^{-1}\ min^{-1}$, which was far higher than that in previously reported MOF-based systems. For example, the value was 0.2 $mg_{Cr(VI)}\ g_{catalyst}^{-1}\ min^{-1}$ for NH_2-UiO-66(Zr) and

Table 7 Hybrid modification strategies for the photocatalytic removal of environmental pollutants under visible light

Composites	S_{BET} [a] ($m^2\ g^{-1}$)	Pollutant	$C_{pollutant}$ ($mg\ L^{-1}$)	$C_{catalyst}$ ($g\ L^{-1}$)	Time (min)	$\eta_{composite}$ [b] (%)	Ref.
Co-modification of MOFs using MNPs and photoactive semiconductors							
Ag/AgCl@ZIF-8	367	ACT	1.0	0.5	90	99	259
Ag/AgCl/ZIF-8	576	RhB	10	1.0	60	98	260
Ag@AgCl/Ag nanofilm/ZIF-8	23	MB	10	1.0	12	96	261
Pt/ZIF-8/TiO_2-NTs	1100	Phenol	52	NA	120	19	262
Ag/AgCl@MIL-53(Fe)	NA	RhB	10	0.4	45	100	263
		Cr(VI)	10	0.4	240	100	
MIL-53(Fe)/Ag/g-C_3N_4;	NA	CLQ	10	0.2	100	95	264
Ag/AgCl@MIL-88A(Fe)	173	IBP	10	0.4	210	100	265
Ag/AgCl@MIL-101(Cr)	2016	RhB	20	1.0	18	96	266
MIL-125(Ti)/Ag/g-C_3N_4	101	NB	2050	0.83	240	43[e]	267
UiO-66(Zr)/g-C_3N_4/Ag	705	RhB	20	0.4	180	93	268
		2,4-D	20	0.4	180	84	
Ag_2CrO_4/Ag/AgCl-HKUST-1[g]	NA	AB	3	0.1	155	98	269
		OG	3	0.1	155	90	
Ag/Ag_3PO_4/HKUST-1	602	PBS	55.6	1.0	80	89	270
Ag_3PO_4/AgBr/Ag-HKUST-1[g]	NA	MB	15	0.4	75	92	271
		ER	15	0.4	75	90	
		A–O	15	0.4	75	90	
Co-modification of MOFs using MNPs and conducting carbon materials							
Ag/GO/MIL-125(Ti)	730	RhB	50	0.4	50	95	272
Pd/GO/MIL-101(Cr)	NA	BC	25	0.25	15	100	273
		AF	25	0.25	15	100	
Co-modification of MOFs using conducting carbon materials and photoactive semiconductors							
BiOBr/GO/MOF-5	185	RhB	NA	NA	120	92	274
SnO_2@UiO-66(Zr)/rGO	437	RhB	50	0.5	150	96	275
Co-modification of MOFs using two different strategies							
MIL-100(Fe)@Fe_3O_4/CA	390	TC	10	0.2	180	85	276
Fe–C oxides/MIL-101(Cr)	1116	X-3B[c]	100	0.1	120	100[d]	277
TiO_2@salicylaldehyde-NH_2-MIL-101(Cr)	853	MB[c]	30	0.125	60	86	278
H_2TCPP⊂(I^-)Meim-UiO-66	502	Cr(VI)	100	0.25	30	100	279
4-PySH@TiO_2/PCN-222(Zn)	1401	RhB[c]	50	0.048	270	98	280
		2,4-DNP[c]	20	0.048	270	68	
Co-modification of MOFs using different photoactive semiconductors							
BiOI@MIL-88A(Fe)@g-C_3N_4	70	AB92	10	0.1	180	88	281
		RhB	10	0.1	180	75	
		Phenol	10	0.1	180	70	
Ag_3PO_4/$BiPO_4$@MIL-88B(Fe)@g-C_3N_4	NA	AB92	10	0.1	60	85	282
Ag_3PO_4/MIL-101(Cr)/$NiFe_2O_4$	313	RhB	10	0.2	30	95	283
CdS/g-C_3N_4/MIL-125(Ti)	238	RhB	NA	NA	60	94	284
CdS/NH_2-MIL-125@TiO_2	968	NO	NA	4.0	5	49	85
N-$K_2Ti_4O_9$/g-C_3N_4/UiO-66(Zr)	288	RhB	10	0.2	180	68[d]	285
$Cd_{0.5}Zn_{0.5}S$@UiO-66(Zr)@g-C_3N_4	147	MO	20	0.2	120	82	286
BiOI@NH_2-UiO-66(Zr)@g-C_3N_4	123	RhB	20	0.2	80	95	287
		TC	20	0.2	180	79	
$BiPO_4$/Bi_2S_3-HKUST-1	670	TB	25	0.25	65	99	288
		AO	25	0.25	65	98	
Ag_3PO_4/Bi_2S_3-HKUST-1[f]	NA	TB	25	0.25	25	98	289
		VS	25	0.25	25	99	

NA: no experimental data available; rGO: reduced graphene oxide; GO: graphene oxide; CA: carbon aerogel. [a] S_{BET} surface area is presented in integer numbers. [b] Removal efficiencies (η) for pollutants are received or estimated from the figures in the reference and presented in integer numbers. [c] Addition of H_2O_2. [d] UV-Vis light or sunlight. [e] Under a N_2 atmosphere with methanol as a h^+ scavenger. [f] Under the assistance of sonication. [g] Measured in a continuous flow photocatalytic rotating packed bed for the degradation of dye mixtures.

1.6 $mg_{Cr(VI)}\ g_{catalyst}^{-1}\ min^{-1}$ NH_2-MIL-125(Ti), respectively. Thus, for the removal of environmental pollutants, targeted modification strategies deserve intensive study.

3.10 Carrier loading and magnetic recovery

In addition to high reactivity, good recyclability also plays an important role in further large-scale industrial applications. Since most pristine MOFs are highly dispersive in water and difficult to be separated, it is therefore desirable to enhance the recyclability. Typically, immobilization on an inert carrier or introduction of a magnetic component were proved to be two promising approaches. As listed in Table 8, resin and SBA-15 were applied as supports to immobilize MOFs with enhanced stability and photocatalytic performance.

For example, Huang's group investigated the immobilization of MIL-53(Fe) with anionic resin (Amberlite IRA 200) and cationic resin (Amberlite IRA 900), respectively. The resulting AMIL-53(Fe) and DMIL-53(Fe) showed negligible changes in the UV-Vis DRS spectra and flat band potential measurements, indicating that the optical properties and electronic properties

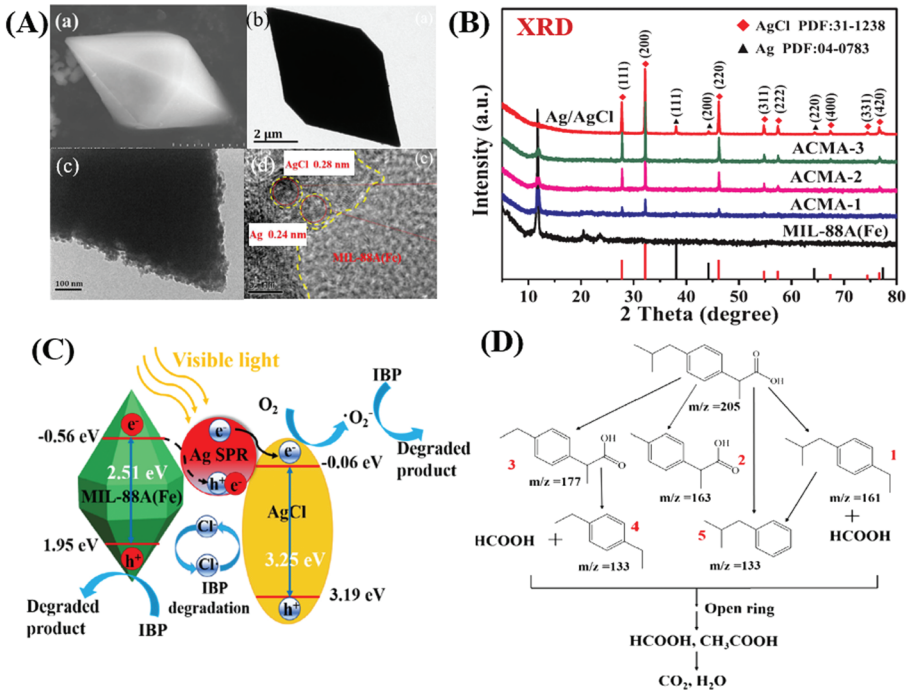

Fig. 34 (A) (a) SEM; (b) TEM; (c) and (d) HRTEM images of Ag/AgCl@MIL-88A(Fe); (B) XRD patterns of different samples; (C) proposed mechanism for photocatalytic degradation of IBP by Ag/AgCl@MIL-88A(Fe) under visible light irradiation; (D) proposed degradation pathway of IBP. Adapted with permission from ref. 265, © 2018 Elsevier B.V.

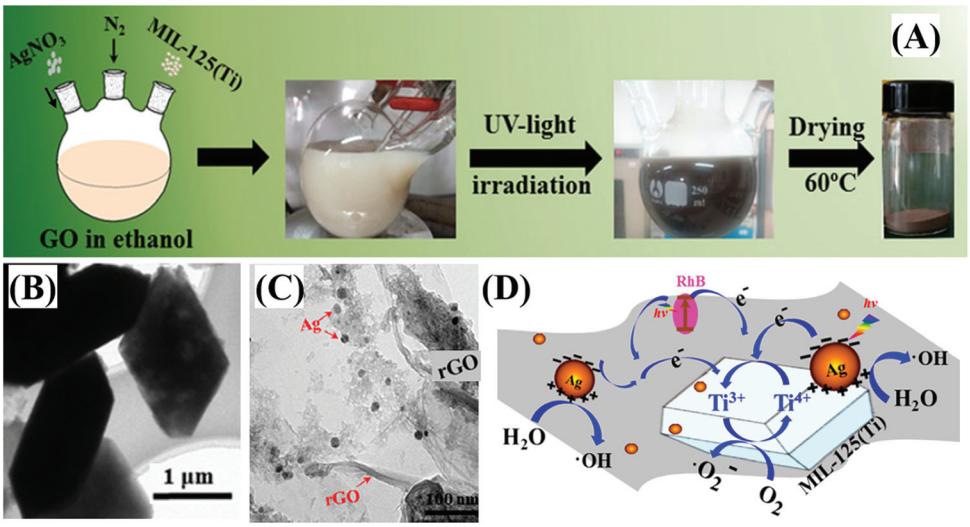

Fig. 35 (A) Schematic processes for the preparation of Ag/rGO/MIL-125(Ti); (B) TEM image of MIL-125(Ti); (C) HRTEM image (insert: TEM image) of Ag/rGO/MIL-125(Ti); (D) proposed mechanism for photocatalytic degradation of RhB by the Ag/rGO/MIL-125(Ti) ternary composite. Adapted with permission from ref. 272, © 2016 John Wiley.

were not influenced after immobilization. Decreased charge transfer resistance can be deduced from the EIS Nyquist plot with a smaller radius of curvature. The different charge characteristic of AMIL-53(Fe) and DMIL-53(Fe) led to prior adsorption and degradation of RhB and SRB, respectively. In particular, a dramatic difference can be observed in the stability of MIL-53. As shown in Fig. 37, the leaching of Fe(III) ions from MIL-53 can be significantly inhibited on AMIL-53(Fe). The reason may be ascribed to the chelation effect between the $-SO_3^-$ group of Amberlite IRA200 and Fe(III). Accordingly, for the degradation of RhB, AMIL-53 exhibited the highest stability after 5 cyclic runs.

As for preparing magnetically recyclable MOFs, Fe_3O_4 nanoparticles with good magnetic properties and low toxicity were

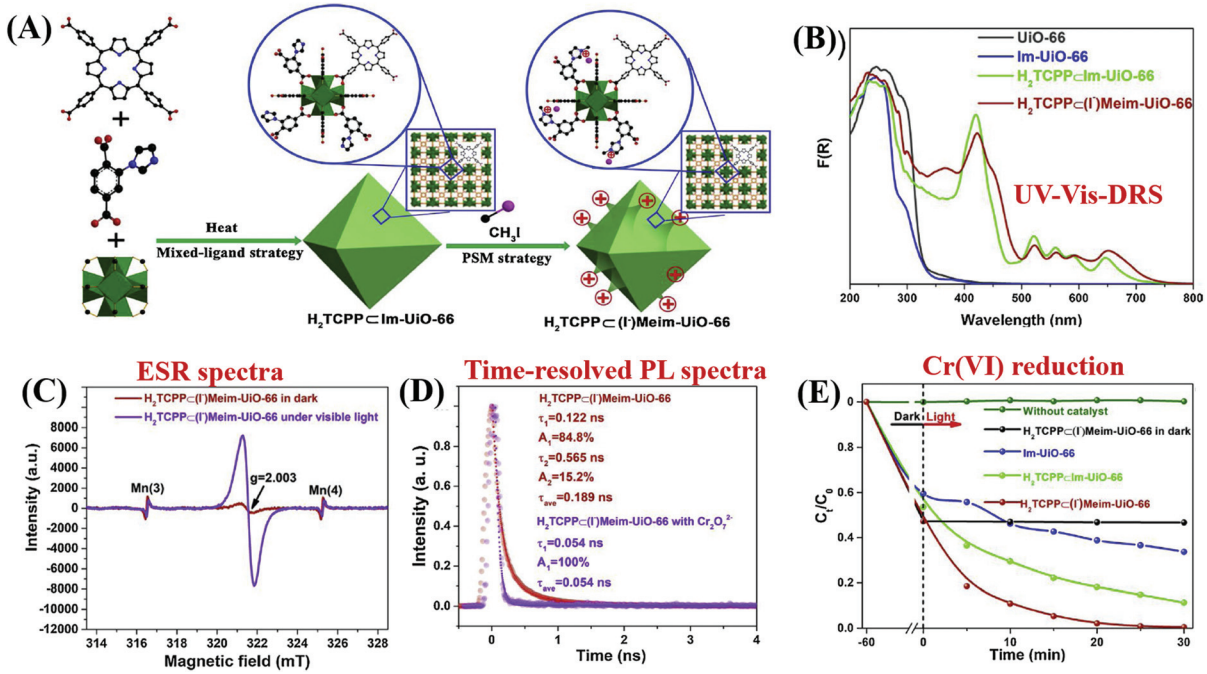

Fig. 36 (A) Schematic processes for the preparation of $H_2TCPP\subset(I^-)$Meim-UiO-66; (B) UV-vis-DRS of different samples; (C) ESR analyses of $H_2TCPP\subset(I^-)$Meim-UiO-66 with Mn as an internal standard; (D) time-resolved PL spectra of $H_2TCPP\subset(I^-)$Meim-UiO-66 suspensions with and without the presence of $Cr_2O_7^{2-}$ at an emission wavelength of 650 nm (λ_{ex} = 400 nm); (E) photocatalytic reduction of Cr(VI) by different samples under visible light irradiation. Adapted with permission from ref. 279, © 2019 Elsevier B.V.

Table 8 MOF-based composites with easy recyclability for the photocatalytic removal of environmental pollutants

Composite	S_{BET} variation[a] ($m^2\ g^{-1}$)	Pollutant	$C_{pollutant}$ ($mg\ L^{-1}$)	$C_{catalyst}$ ($g\ L^{-1}$)	Time (min)	η[b] variation (%)	Ref.
Immobilization on inert carriers							
Resin/MIL-53 (Fe)	NA	SRB	3.3[c]	0.17	120	24 → 96	292
A@FeBTC[d]	NA	RhB	35	0.4	60	69 → 99	293
HKUST-1/SBA-15	197 → 532	MG	10	0.25	80	NA → 99	70
		SO	15	0.25	80	NA → 88	
Combined with magnetic components							
Fe_3O_4@ZIF-67	301	CR	7	0.5	30	NA → 95	294
Fe_3O_4/MIL-53(Fe)	NA	RhB[e]	10	0.4	70	99 → 99	295
γ-Fe_2O_3/MIL-53(Fe)	1835 → 60	MB	10	0.4	240	87 → 72	296
Fe_3O_4@MIL-100(Fe)	1766 → 1245	DCF[e]	60	0.1	120	100 → 91	297
Fe_3O_4@MIL-100(Fe)	1646 → 213	MB[e]	50	0.1	120	68 → 99	298
MIL-100(Fe)@Fe_3O_4/CA[f]	725 → 390	TC	10	0.2	180	42 → 85	276

NA: no experimental data available. [a] S_{BET} variation indicates the surface area of MOFs before and after forming composites. [b] Removal efficiencies (η) for pollutants are used as received or estimated from the figures in the reference and presented in integer numbers; η variation indicates the performance of MOFs before and after forming composites. [c] mM. [d] Amberlite IRA-200 resin. [e] Addition of H_2O_2. [f] CA: carbon aerogel.

frequently used to form composites with MOFs. However, due to easy photo-dissolution of Fe_3O_4, MOFs were designed as shells with Fe_3O_4 as the core. The as-prepared core–shell structure displayed good stability and recyclability. For example, Zhao's group reported the fabrication of core–shell Fe_3O_4@MIL-100(Fe) microspheres (Fig. 38A–C).[298] Among the as-prepared Fe_3O_4@MIL-100(Fe) samples, the one with 20 cycles exhibited the highest photocatalytic performance for MB degradation in the presence of H_2O_2 under visible light. Moreover, the performance of magnetic Fe_3O_4@MIL-100(Fe) can be well maintained after four cyclic runs with negligible changes in the crystalline structure (Fig. 38D and E). Besides, Fe(III) ion leaching can be greatly inhibited after covering a MOF shell, and a thicker shell is more beneficial (Fig. 38F). For example, the value for Fe(III) ion leaching decreased from 1.96 ppm on pristine MIL-100(Fe) to 0.41 ppm on Fe_3O_4@MIL-100(Fe) prepared in 40 cycles. Mechanism study further indicated that the photogenerated h^+ in the MOF shell can access the Fe_3O_4 core, leading to efficient separation of e^-–h^+ pairs. The separated e^- can react with H_2O_2 forming active $HO^\bullet$ radicals, which finally lead to the degradation of MB dye (Fig. 38G).

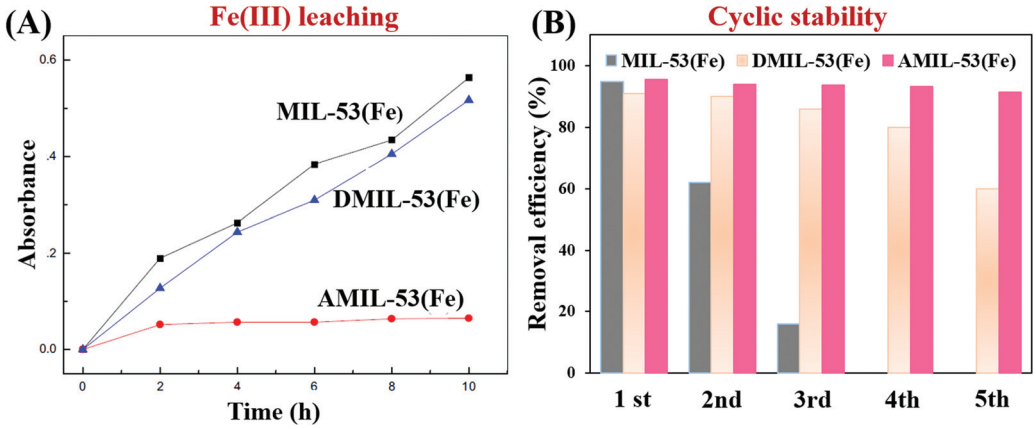

Fig. 37 (A) Comparison of Fe(III) ion leaching from MIL-53 (Fe), DMIL-53(Fe) and AMIL-53(Fe) in water under visible light irradiation; (B) comparison of cycling stability for RhB degradation over recycled MIL-53(Fe), DMIL-53(Fe) and AMIL-53(Fe). Adapted with permission from ref. 292, © 2017 Elsevier.

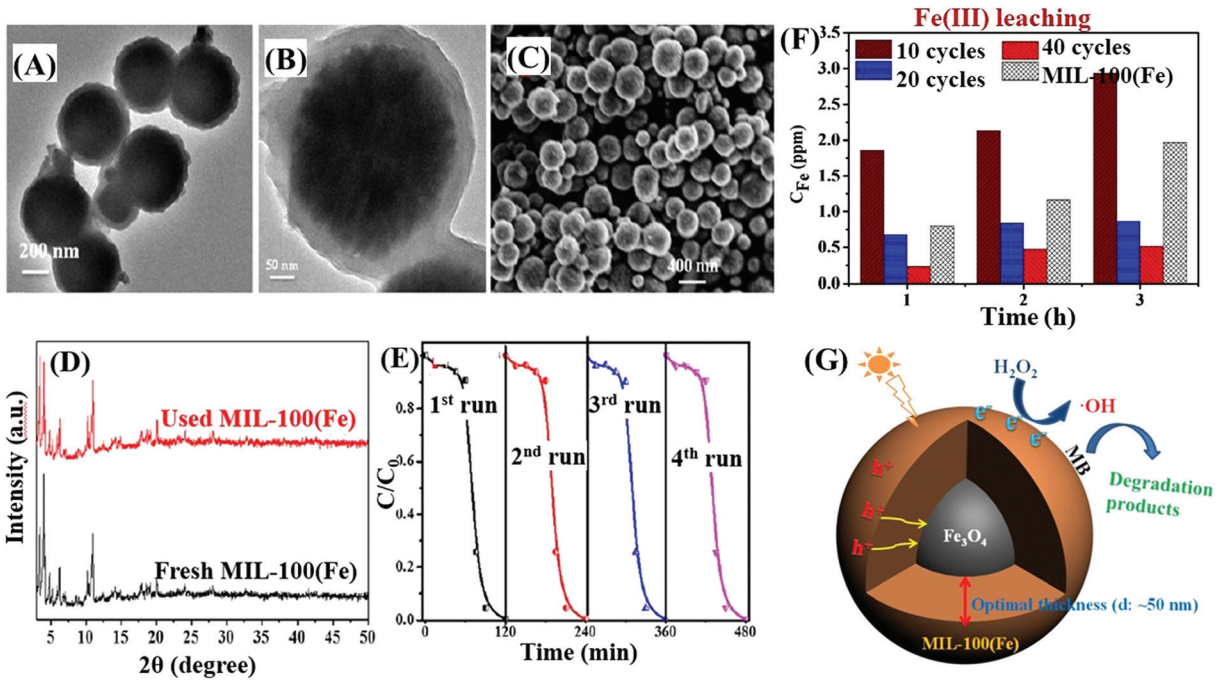

Fig. 38 The TEM (A and B) and SEM (C) images of used Fe_3O_4@MIL-100 with 20 assembly cycles, which had been reacted with H_2O_2 for 180 min at pH 3.00; (D) comparison of XRD patterns between fresh MIL-100(Fe) and used MIL-100(Fe); (E) cyclic degradation of MB using Fe_3O_4@MIL-100 with 20 assembly cycles; (F) comparison of Fe(III) ion leaching in water from different Fe_3O_4@MIL-100(Fe) samples; (G) proposed mechanism for MB degradation. Adapted with permission from ref. 298, © 2015 Wiley-VCH.

4. Conclusions and outlook

In this review, we summarize and illustrate recent progress in MOF-based photocatalysis for environmental remediation. The unparalleled versatility of MOFs allows many strategies to modify and regulate pristine MOFs for enhanced photocatalytic performance under visible light. However, MOF-based environmental photocatalysis is currently at the stage of infancy, which needs to be further developed as amiable and stable technology for low cost practical applications in the future. In general, intensive research work should be carried out to overcome the following challenges and obstacles:

(1) Most photo-active MOFs are still at the stage of lab-scale, which cannot be fabricated by one-time high-throughput synthesis. Besides, some preparation methods are complicated and difficult to control. The development of more facile synthetic routes, especially a one-step approach under mild conditions, will be highly desirable for future large-scale applications.

(2) Although there are many reports on water-resistant MOFs, such as UiO-66, MIL-125, MIL-101 and ZIF series, the stability under harsh conditions (strong acidic and alkaline pH) still needs to be improved. Besides, according to metal–ligand bond strengths and the HSAB (hard/soft acid/base) principle,[5] the selection of high-valent metal ions (such as Mo^{6+}, W^{6+}, *etc.*) as metal centers may arouse great interest for fabricating novel stable MOFs.

(3) As for MNP/MOF composites, most of the loaded metal nanoparticles were precious metals (such as Pd, Pt, Au, and Ag). Research on non-precious metals (such as Cu and Bi) deserves more exploration.

(4) In addition to immobilization on an inert carrier and introduction of a magnetic component, the fabrication of MOF films is another attractive way for the recycling of MOFs. However, the utilization of MOF films for environmental photocatalysis was very limited. In particular, the fabrication of MOF films on a conductive substrate needs to be further developed for photoelectrocatalytic degradation of organic pollutants and reduction of heavy metal ions.

(5) Up to now, multi-functional applications of MOFs were limited. There are only sporadic reports on simultaneous photocatalytic oxidation of dyes and reduction of Cr(VI) or H^+ (H_2 production).[47,135,150,299] More efficient multi-functional MOFs are required for the simultaneous and synergistic removal of environmental pollutants and production of energy or valuable products in one system.

(6) For better regulation of MOF photocatalysis, more efforts are needed to intensively explore the degradation processes. For example, the toxicity of degradation intermediates should be evaluated due to incomplete mineralization of organic pollutants under most circumstances.

(7) In addition to the detection of active species (such as $HO^{\bullet}$, $O_2^{\bullet-}$ and h^+) during photocatalysis, more details associated with the photocatalytic mechanism need in-depth investigation. For example, the adsorption sites of contaminants on the surface/in the channel of MOFs, the interfacial electron transfer mechanism as well as the rate limiting step should be identified. Based on these, the design of appropriate modification strategies will be more scientific and effective.

(8) Finally, there is still an urgent need to develop novel robust MOFs with excellent light harvesting properties, high stability and easy recyclability through the engineering of metallic nodes and organic linkers.

In summary, although there are still many challenges to be solved, in the past two decades of development, researchers from all over the world have made great progress in MOF materials from structural design, controllable modification to functional applications. We believe that with the joint efforts of researchers in many fields, the prospects of MOFs for environmental photocatalysis will be definitely bright.

Conflicts of interest

There are no conflicts to declare.

Acknowledgements

The authors are grateful for financial support from the National Natural Science Foundation of China (21876154), the Zhejiang Provincial Natural Science Foundation of China (LR18B070001), the US National Science Foundation (CBET-1706025) and the University of South Florida. The authors also extend their appreciation to the Distinguished Scientist Fellowship Program (DSFP) at King Saud University for partial funding of this work.

References

1 J. Schneider, M. Matsuoka, M. Takeuchi, J. Zhang, Y. Horiuchi, M. Anpo and D. W. Bahnemann, *Chem. Rev.*, 2014, **114**, 9919.
2 M. N. Chong, B. Jin, C. W. K. Chow and C. Saint, *Water Res.*, 2010, **44**, 2997.
3 H. C. Zhou and S. Kitagawa, *Chem. Soc. Rev.*, 2014, **43**, 5415.
4 H. Furukawa, N. Ko, Y. B. Go, N. Aratani, S. B. Choi, E. Choi, A. Ö. Yazaydin, R. Q. Snurr, M. O'Keeffe, J. Kim and O. M. Yaghi, *Science*, 2010, **329**, 424.
5 T. Devic and C. Serre, *Chem. Soc. Rev.*, 2014, **43**, 6097.
6 E. M. Dias and C. Petit, *J. Mater. Chem. A*, 2015, **3**, 22484.
7 J. Bedia, V. Muelas-Ramos, M. Peñas-Garzón, A. Gómez-Avilés, J. J. Rodríguez and C. Belver, *Catalysts*, 2019, **9**, 52.
8 C. C. Wang, X. D. Du, J. Li, X. X. Guo, P. Wang and L. Zhang, *Appl. Catal., B*, 2016, **193**, 198.
9 J. D. Xiao, D. Li and H. L. Jiang, *Sci. Sin.: Chim.*, 2018, **48**, 1058.
10 J. L. Wang, C. Wang and W. Lin, *ACS Catal.*, 2012, **2**, 2630.
11 J. He, Y. Zhang, J. He, X. Zeng, X. Hou and Z. Long, *Chem. Commun.*, 2018, **54**, 8610.
12 M. A. Nasalevich, M. van der Veen, F. Kapteijn and J. Gascon, *CrystEngComm*, 2014, **16**, 4919.
13 D. Wang, M. Wang and Z. Li, *ACS Catal.*, 2015, **5**, 6852.
14 C. Wang, X. Liu, N. Keser Demir, J. P. Chen and K. Li, *Chem. Soc. Rev.*, 2016, **45**, 5107.
15 P. Li, J. Li, X. Feng, J. Li, Y. Hao, J. Zhang, H. Wang, A. Yin, J. Zhou, X. Ma and B. Wang, *Nat. Commun.*, 2019, **10**, 2177.
16 Y. Shi, A. F. Yang, C. S. Cao and B. Zhao, *Coord. Chem. Rev.*, 2019, **390**, 50.
17 X. Ma, L. Wang, Q. Zhang and H. L. Jiang, *Angew. Chem., Int. Ed.*, 2019, **58**, 12175.
18 C. C. Wang, Y. Q. Zhang, J. Li and P. Wang, *J. Mol. Struct.*, 2015, **1083**, 127.
19 X. Yu, L. Wang and S. M. Cohen, *CrystEngComm*, 2017, **19**, 4126.
20 S. N. Zhao, G. Wang, D. Poelman and P. Van Der Voort, *Molecules*, 2018, **23**, 2947.
21 H. Liu, C. Xu, D. Li and H. L. Jiang, *Angew. Chem.*, 2018, **130**, 5477.

22 X. Liang, L. Chen, L. Zhang and C. Y. Su, *Chin. Sci. Bull.*, 2018, **63**, 248.
23 Q. Xia, H. Wang, B. Huang, X. Yuan, J. Zhang, J. Zhang, L. Jiang, T. Xiong and G. Zeng, *Small*, 2019, **15**, 1803088.
24 J. D. Xiao and H. L. Jiang, *Acc. Chem. Res.*, 2019, **52**, 356.
25 L. Jiao, J. Y. R. Seow, W. S. Skinner, Z. U. Wang and H. L. Jiang, *Mater. Today*, 2019, **27**, 43.
26 B. Pattengale, S. Yang, J. Ludwig, Z. Huang, X. Zhang and J. Huang, *J. Am. Chem. Soc.*, 2016, **138**, 8072.
27 C. C. Wang, J. R. Li, X. L. Lv, Y. Q. Zhang and G. S. Guo, *Energy Environ. Sci.*, 2014, **7**, 2831.
28 Y. Li, H. Xu, S. Ouyang and J. Ye, *Phys. Chem. Chem. Phys.*, 2016, **18**, 7563.
29 J. Qiu, X. Zhang, Y. Feng, X. Zhang, H. Wang and J. Yao, *Appl. Catal., B*, 2018, **231**, 317.
30 J. Bedia, V. Muelas-Ramos, M. Peñas-Garzón, A. Gómez-Avilés, J. J. Rodríguez and C. Belver, *Catalysts*, 2019, **9**, 52.
31 D. Wang and Z. Li, *Res. Chem. Intermed.*, 2017, **43**, 5169.
32 Z. Yan, H. Xi and L. Yuan, *Environ. Sci.*, 2019, **40**, 1819.
33 Z. Zhang, X. Li, B. Liu, Q. Zhao and G. Chen, *RSC Adv.*, 2016, **6**, 4289.
34 S. R. Thakare and S. M. Ramteke, *Catal. Commun.*, 2017, **102**, 21.
35 H. Li, M. Eddaoudi, M. O'Keeffe and O. M. Yaghi, *Nature*, 1999, **402**, 276.
36 S. Bordiga, C. Lamberti, G. Ricchiardi, L. Regli, F. Bonino, A. Damin, K. P. Lillerud, M. Bjorgen and A. Zecchina, *Chem. Commun.*, 2004, 2300.
37 M. Alvaro, E. Carbonell, B. Ferrer, F. X. Llabres, I. Xamena and H. Garcia, *Chem. – Eur. J.*, 2007, **13**, 5106.
38 T. Tachikawa, J. R. Choi, M. Fujitsuka and T. Majima, *J. Phys. Chem. C*, 2008, **112**, 14090.
39 S. Yuan, L. Feng, K. Wang, J. Pang, M. Bosch, C. Lollar, Y. Sun, J. Qin, X. Yang, P. Zhang, Q. Wang, L. Zou, Y. Zhang, L. Zhang, Y. Fang, J. Li and H. Zhou, *Adv. Mater.*, 2018, **30**, 1704303.
40 J. H. Cavka, S. Jakobsen, U. Olsbye, N. Guillou, C. Lamberti, S. Bordiga and K. P. Lillerud, *J. Am. Chem. Soc.*, 2008, **130**, 13850.
41 C. Gomes Silva, I. Luz, F. X. Llabrés i Xamena, A. Corma and H. García, *Chem. – Eur. J.*, 2010, **16**, 11133.
42 M. Dan-Hardi, C. Serre, T. Frot, L. Rozes, G. Maurin, C. Sanchez and G. Férey, *J. Am. Chem. Soc.*, 2009, **131**, 10857.
43 L. Shen, R. Liang, M. Luo, F. Jing and L. Wu, *Phys. Chem. Chem. Phys.*, 2015, **17**, 117.
44 J. Gascon, M. D. Hernández-Alonso, A. R. Almeida, G. P. M. van Klink, F. Kapteijn and G. Mul, *ChemSusChem*, 2008, **1**, 981.
45 J. X. Liu, M. Y. Gao, W. H. Fang, L. Zhang and J. Zhang, *Angew. Chem., Int. Ed.*, 2016, **55**, 5160.
46 H. Furukawa, K. E. Cordova, M. O'Keeffe and O. M. Yaghi, *Science*, 2013, **341**, 1230444.
47 R. Liang, F. Jing, L. Shen, N. Qin and L. Wu, *J. Hazard. Mater.*, 2015, **287**, 364.
48 Y. K. Seo, J. W. Yoon, J. S. Lee, Y. K. Hwang, C. H. Jun, J. S. Chang, S. Wuttke, P. Bazin, A. Vimont, M. Daturi, S. Bourrelly, P. L. Llewellyn, P. Horcajada, C. Serre and G. Férey, *Adv. Mater.*, 2012, **24**, 806.
49 P. Horcajada, T. Chalati, C. Serre, B. Gillet, C. Sebrie, T. Baati, J. F. Eubank, D. Heurtaux, P. Clayette, C. Kreuz, J.-S. Chang, Y. K. Hwang, V. Marsaud, P.-N. Bories, L. Cynober, S. Gil, G. Férey, P. Couvreur and R. Gref, *Nat. Mater.*, 2009, **9**, 172.
50 P. Horcajada, H. Chevreau, D. Heurtaux, F. Benyettou, F. Salles, T. Devic, A. Garcia-Marquez, C. Yu, H. Lavrard, C. L. Dutson, E. Magnier, G. Maurin, E. Elkaïm and C. Serre, *Chem. Commun.*, 2014, **50**, 6872.
51 K. Leus, T. Bogaerts, J. De Decker, H. Depauw, K. Hendrickx, H. Vrielinck, V. Van Speybroeck and P. Van Der Voort, *Microporous Mesoporous Mater.*, 2016, **226**, 110.
52 Y. Fang, J. Wen, G. Zeng, F. Jia, S. Zhang, Z. Peng and H. Zhang, *Chem. Eng. J.*, 2018, **337**, 532.
53 Y. K. Seo, J. W. Yoon, J. S. Lee, U. H. Lee, Y. K. Hwang, C. H. Jun, P. Horcajada, C. Serre and J. S. Chang, *Microporous Mesoporous Mater.*, 2012, **157**, 137.
54 D. Wang, F. Jia, H. Wang, F. Chen, Y. Fang, W. Dong, G. Zeng, X. Li, Q. Yang and X. Yuan, *J. Colloid Interface Sci.*, 2018, **519**, 273.
55 M. C. Das, H. Xu, Z. Wang, G. Srinivas, W. Zhou, Y. F. Yue, V. N. Nesterov, G. Qian and B. Chen, *Chem. Commun.*, 2011, **47**, 11715.
56 S. Pu, L. Xu, L. Sun and H. B. Du, *Inorg. Chem. Commun.*, 2015, **52**, 50.
57 T. L. H. Doan, H. L. Nguyen, H. Q. Pham, N.-N. Pham-Tran, T. N. Le and K. E. Cordova, *Chem. – Asian J.*, 2015, **10**, 2660.
58 Y. Gao, S. Li, Y. Li, L. Yao and H. Zhang, *Appl. Catal., B*, 2017, **202**, 165.
59 L. Ai, C. Zhang, L. Li and J. Jiang, *Appl. Catal., B*, 2014, **148–149**, 191.
60 C. J. N. Liu, Z. Li, W. Huang, B. Gao, F. You and X. Zhang, *Mater. Lett.*, 2019, **237**, 92.
61 W. Mei, D. Li, H. Xu, J. Zan, L. Sun, Q. Li, B. Zhang, Y. Wang and D. Xia, *Chem. Phys. Lett.*, 2018, **706**, 694.
62 J. J. Du, Y. P. Yuan, J. X. Sun, F. M. Peng, X. Jiang, L. G. Qiu, A. J. Xie, Y. H. Shen and J. F. Zhu, *J. Hazard. Mater.*, 2011, **190**, 945.
63 Y. Gao, G. Yu, K. Liu, S. Deng, B. Wang, J. Huang and W. Wang, *Chem. Eng. J.*, 2017, **330**, 157.
64 R. Li, Z. Chen, M. Cai, J. Huang, P. Chen and G. Liu, *Appl. Surf. Sci.*, 2018, **457**, 726.
65 F. Jing, R. Liang, J. Xiong, R. Chen, S. Zhang, Y. Li and L. Wu, *Appl. Catal., B*, 2017, **206**, 9.
66 B. Xu, H. Yang, Y. Cai, H. Yang and C. Li, *Inorg. Chem. Commun.*, 2016, **67**, 29.
67 Y. Li, G. Hou, J. Yang, J. Xie, X. Yuan, H. Yang and M. Wang, *RSC Adv.*, 2016, **6**, 16395.
68 W. T. Xu, L. Ma, F. Ke, F. M. Peng, G. S. Xu, Y. H. Shen, J. F. Zhu, L. G. Qiu and Y. P. Yuan, *Dalton Trans.*, 2014, **43**, 3792.

69 A. M. G. Kiros, C. A. D. Caiuby, M. Díaz-García, I. Díaz and M. S-Sanchez, *Cryst. Growth Des.*, 2017, **17**, 1806.
70 S. Mosleh, M. R. Rahimi, M. Ghaedi, K. Dashtian and S. Hajati, *RSC Adv.*, 2016, **6**, 17204.
71 M. C. Das, H. Xu, Z. Wang, G. Srinivas, W. Zhou, Y. Yue, V. N. Nesterov, G. Qian and B. Chen, *Chem. Commun.*, 2011, **47**, 11715.
72 G. Wang, Q. Sun, Y. Liu, B. Huang, Y. Dai, X. Zhang and X. Qin, *Chem. – Eur. J.*, 2015, **21**, 2364.
73 A. N. Meng, L. X. Chaihu, H. H. Chen and Z. Y. Gu, *Sci. Rep.*, 2017, **7**, 6297.
74 Y. Fu, D. Sun, Y. Chen, R. Huang, Z. Ding, X. Fu and Z. Li, *Angew. Chem., Int. Ed.*, 2012, **51**, 3364.
75 M. A. Nasalevich, M. G. Goesten, T. J. Savenije, F. Kapteijn and J. Gascon, *Chem. Commun.*, 2013, **49**, 10575.
76 J. Gao, J. Miao, P. Z. Li, W. Y. Teng, L. Yang, Y. Zhao, B. Liu and Q. Zhang, *Chem. Commun.*, 2014, **50**, 3786.
77 C. H. Hendon, D. Tiana, M. Fontecave, C. Sanchez, L. D'Arras, C. Sassoye, L. Rozes, C. Mellot-Draznieks and A. Walsh, *J. Am. Chem. Soc.*, 2013, **135**, 10942.
78 K. Hendrickx, D. E. P. Vanpoucke, K. Leus, K. Lejaeghere, A. Van Yperen-De Deyne, V. Van Speybroeck, P. Van Der Voort and K. Hemelsoet, *Inorg. Chem.*, 2015, **54**, 10701.
79 X. P. Wu, L. Gagliardi and D. G. Truhlar, *J. Am. Chem. Soc.*, 2018, **140**, 7904.
80 A. Dhakshinamoorthy, Z. Li and H. Garcia, *Chem. Soc. Rev.*, 2018, **47**, 8134.
81 R. Liang, R. Huang, X. Wang, S. Ying, G. Yan and L. Wu, *Appl. Surf. Sci.*, 2019, **464**, 396.
82 L. Shi, T. Wang, H. Zhang, K. Chang, X. Meng, H. Liu and J. Ye, *Adv. Sci.*, 2015, **2**, 1500006.
83 X. D. Du, X. H. Yi, P. Wang, W. W. Zheng, J. G. Deng and C. C. Wang, *Chem. Eng. J.*, 2019, **356**, 393.
84 S. Hu, M. Liu, K. Y. Li, C. S. Song, G. L. Zhang and X. W. Guo, *RSC Adv.*, 2017, **7**, 581.
85 S. Gao, W. Cen, Q. Li, J. Li, Y. Lu, H. Wang and Z. Wu, *Appl. Catal., B*, 2018, **227**, 190.
86 H. Wang, X. Yuan, Y. Wu, G. Zeng, X. Chen, L. Leng, Z. Wu, L. Jiang and H. Li, *J. Hazard. Mater.*, 2015, **286**, 187.
87 R. W. Liang, L. J. Shen, F. F. Jing, W. M. Wu, N. Qin, R. Lin and L. Wu, *Appl. Catal., B*, 2015, **162**, 245.
88 J. Wang, J. Wu, L. Lu, H. Xu, M. Trivedi, A. Kumar, J. Liu and M. Zheng, *Front. Chem.*, 2019, **7**, DOI: 10.3389/fchem.2019.00244.
89 L. F. Song, C. H. Jiang, C. L. Jiao, J. Zhang, L. X. Sun, F. Xu, W. S. You, Z. G. Wang and J. J. Zhao, *Cryst. Growth Des.*, 2010, **10**, 5020.
90 S. Abednatanzi, P. G. Derakhshandeh, H. Depauw, F. X. Coudert, H. Vrielinck, P. V. D. Voort and K. Leus, *Chem. Soc. Rev.*, 2019, **48**, 2535.
91 A. Dhakshinamoorthy, A. M. Asiri and H. Garcia, *Catal. Sci. Technol.*, 2016, **6**, 5238.
92 M. Kim, J. F. Cahill, H. Fei, K. A. Prather and S. M. Cohen, *J. Am. Chem. Soc.*, 2012, **134**, 18082.
93 L. G. Yu, Y. G. Sun and Z. L. Wang, *J. Mol. Struct.*, 2019, **1180**, 209.
94 Y. Lee, S. Kim, J. K. Kang and S. M. Cohen, *Chem. Commun.*, 2015, **51**, 5735.
95 D. Sun, W. Liu, M. Qiu, Y. Zhang and Z. Li, *Chem. Commun.*, 2015, **51**, 2056.
96 A. Santiago Portillo, H. G. Baldoví, M. T. García Fernandez, S. Navalón, P. Atienzar, B. Ferrer, M. Alvaro, H. Garcia and Z. Li, *J. Phys. Chem. C*, 2017, **121**, 7015.
97 J. Tu, X. Zeng, F. Xu, X. Wu, Y. Tian, X. Hou and Z. Long, *Chem. Commun.*, 2017, **53**, 3361.
98 H. Yang, X. W. He, F. Wang, Y. Kang and J. Zhang, *J. Mater. Chem.*, 2012, **22**, 21849.
99 S. Das, H. Kim and K. Kim, *J. Am. Chem. Soc.*, 2009, **131**, 3814.
100 R. Li, X. Ren, H. Ma, X. Feng, Z. Lin, X. Li, C. Hu and B. Wang, *J. Mater. Chem. A*, 2014, **2**, 5724.
101 D. Ao, J. Zhang and H. Liu, *J. Photochem. Photobiol., A*, 2018, **364**, 524.
102 T. A. Vu, G. H. Le, C. D. Dao, L. Q. Dang, K. T. Nguyen, P. T. Dang, H. T. K. Tran, Q. T. Duong, T. V. Nguyen and G. D. Lee, *RSC Adv.*, 2014, **4**, 41185.
103 J. Li, J. Yang, Y. Y. Liu and J. F. Ma, *Chem. – Eur. J.*, 2015, **21**, 4413.
104 A. Abbasi, M. Soleimani, M. Najafi and S. Geranmayeh, *Inorg. Chim. Acta*, 2016, **439**, 18.
105 J. Cao, Z. H. Yang, W. P. Xiong, Y. Y. Zhou, Y. R. Peng, X. Li, C. Y. Zhou, R. Xu and Y. R. Zhang, *Chem. Eng. J.*, 2018, **353**, 126.
106 M. Wang, L. Yang, C. Guo, X. Liu, L. He, Y. Song, Q. Zhang, X. Qu, H. Zhang, Z. Zhang and S. Fang, *ChemistrySelect*, 2018, **3**, 3664.
107 A. S. Yasin, J. Li, N. Wu and T. Musho, *Phys. Chem. Chem. Phys.*, 2016, **18**, 12748.
108 J. Klinowski, F. A. Almeida Paz, P. Silva and J. Rocha, *Dalton Trans.*, 2011, **40**, 321.
109 Z. Ni and R. I. Masel, *J. Am. Chem. Soc.*, 2006, **128**, 12394.
110 J. S. Choi, W. J. Son, J. Kim and W. S. Ahn, *Microporous Mesoporous Mater.*, 2008, **116**, 727.
111 T. W. Goh, C. Xiao, R. V. Maligal-Ganesh, X. Li and W. Huang, *Chem. Eng. Sci.*, 2015, **124**, 45.
112 R. Grau-Crespo, A. Aziz, A. W. Collins, R. Crespo-Otero, N. C. Hernández, L. M. Rodriguez-Albelo, A. R. Ruiz-Salvador, S. Calero and S. Hamad, *Angew. Chem., Int. Ed.*, 2016, **55**, 16012.
113 R. Navarro Amador, M. Carboni and D. Meyer, *RSC Adv.*, 2017, **7**, 195.
114 L. Shi, L. Yang, H. Zhang, K. Chang, G. Zhao, T. Kaka and J. Ye, *Appl. Catal., B*, 2018, **224**, 60.
115 K. A. Kovalenko, N. V. Ruban, S. A. Adonin, D. V. Korneev, S. B. Erenburg, S. V. Trubina, K. Kvashnina, M. N. Sokolov and V. P. Fedin, *New J. Chem.*, 2017, **41**, 2255.
116 H. Li, F. Zhai, D. Gui, X. Wang, C. Wu, D. Zhang, X. Dai, H. Deng, X. Su, J. Diwu, Z. Lin, Z. Chai and S. Wang, *Appl. Catal., B*, 2019, **254**, 47.
117 Y. P. Yuan, L. S. Yin, S. W. Cao, G. S. Xu, C. H. Li and C. Xue, *Appl. Catal., B*, 2015, **168–169**, 572.

118 E. H. Otal, M. L. Kim, M. E. Calvo, L. Karvonen, I. O. Fabregas, C. A. Sierra and J. P. Hinestroza, *Chem. Commun.*, 2016, **52**, 6665.
119 J. Qin, S. Wang and X. Wang, *Appl. Catal., B*, 2017, **209**, 476.
120 S. Yang, B. Pattengale, E. L. Kovrigin and J. Huang, *ACS Energy Lett.*, 2017, **2**, 75.
121 T. Zhou, Y. Du, A. Borgna, J. Hong, Y. Wang, J. Han, W. Zhang and R. Xu, *Energy Environ. Sci.*, 2013, **6**, 3229.
122 C. Wang, K. E. deKrafft and W. Lin, *J. Am. Chem. Soc.*, 2012, **134**, 7211.
123 S. R. Thakare and S. M. Ramteke, *J. Phys. Chem. Solids*, 2018, **116**, 264.
124 Q. Liang, M. Zhang, Z. Zhang, C. Liu, S. Xu and Z. Li, *J. Alloys Compd.*, 2017, **690**, 123.
125 Q. Li, Z. Fan, L. Zhang, Y. Li, C. Chen, R. Zhao and W. Zhu, *J. Solid State Chem.*, 2019, **269**, 465.
126 L. H. Zhang, Y. Zhu, B. R. Lei, Y. Li, W. Zhu and Q. Li, *Inorg. Chem. Commun.*, 2018, **94**, 27.
127 X. Han, X. Yang, G. Liu, Z. Li and L. Shao, *Chem. Eng. Res. Des.*, 2019, **143**, 90.
128 Q. Yang, Q. Xu and H. L. Jiang, *Chem. Soc. Rev.*, 2017, **46**, 4774.
129 T. Zhang, Y. Jin, Y. Shi, M. Li, J. Li and C. Duan, *Coord. Chem. Rev.*, 2019, **380**, 201.
130 D. N. Jiang, P. Xu, H. Wang, G. M. Zeng, D. L. Huang, M. Chen, C. Lai, C. Zhang, J. Wan and W. J. Xue, *Coord. Chem. Rev.*, 2018, **376**, 449.
131 X. Fang, Q. Shang, Y. Wang, L. Jiao, T. Yao, Y. Li, Q. Zhang, Y. Luo and H. L. Jiang, *Adv. Mater.*, 2018, **30**, 1705112.
132 D. Sun and Z. Li, *J. Phys. Chem. C*, 2016, **120**, 19744.
133 J. D. Xiao, L. Han, J. Luo, S. H. Yu and H. L. Jiang, *Angew. Chem., Int. Ed.*, 2018, **57**, 1103.
134 D. Li, S. H. Yu and H. L. Jiang, *Adv. Mater.*, 2018, **30**, 1707377.
135 L. Shen, W. Wu, R. Liang, R. Lin and L. Wu, *Nanoscale*, 2013, **5**, 9374.
136 S. L. R. Liang, F. Jing, L. Shen, N. Qin and L. Wu, *Appl. Catal., B*, 2015, **176–177**, 240.
137 R. Liang, F. Jing, L. Shen, N. Qin and L. Wu, *Nano Res.*, 2015, **8**, 3237.
138 J. Qiu, L. Yang, M. Li and J. Yao, *Mater. Res. Bull.*, 2019, **112**, 297.
139 T. Toyao, M. Saito, Y. Horiuchi, K. Mochizuki, M. Iwata, H. Higashimura and M. Matsuoka, *Catal. Sci. Technol.*, 2013, **3**, 2092.
140 H. Guo, D. Guo, Z. Zheng, W. Weng and J. Chen, *Appl. Organomet. Chem.*, 2015, **29**, 618.
141 R. M. Abdelhameed, M. M. Simoes, A. M. Silva and J. Rocha, *Chem. – Eur. J.*, 2015, **21**, 11072.
142 W. Zhang, L. Wang and J. Zhang, *Res. Chem. Intermed.*, 2019, **45**, 4801.
143 Y. Huang, Y. Zhang, X. Chen, D. Wu, Z. Yi and R. Cao, *Chem. Commun.*, 2014, **50**, 10115.
144 Y. Zhang and S. J. Park, *Chem. Eng. J.*, 2019, **369**, 353.
145 R. Liang, S. Luo, F. Jing, L. Shen, N. Qin and L. Wu, *Appl. Catal., B*, 2015, **176–177**, 240.
146 J. Zhang, M. Vasei, Y. Sang, H. Liu and J. P. Claverie, *ACS Appl. Mater. Interfaces*, 2016, **8**, 1903.
147 J. S. Lee, K. H. You and C. B. Park, *Adv. Mater.*, 2012, **24**, 1084.
148 M. Han, S. Zhu, S. Lu, Y. Song, T. Feng, S. Tao, J. Liu and B. Yang, *Nano Today*, 2018, **19**, 201.
149 Y. Zhang, G. Li, H. Lu, Q. Lv and Z. Sun, *RSC Adv.*, 2014, **4**, 7594.
150 R. Liang, L. Shen, F. Jing, N. Qin and L. Wu, *ACS Appl. Mater. Interfaces*, 2015, **7**, 9507.
151 C. Yang, X. You, J. Cheng, H. Zheng and Y. Chen, *Appl. Catal., B*, 2017, **200**, 673.
152 T. A. Vu, G. H. Le, H. T. Vu, K. T. Nguyen, T. T. T. Quan, Q. K. Nguyen, H. T. K. Tran, P. T. Dang, L. D. Vu and G. D. Lee, *Mater. Res. Express*, 2017, **4**, 035038.
153 Y. Wu, H. Luo and H. Wang, *RSC Adv.*, 2014, **4**, 40435.
154 X. Li, Z. Le, X. Chen, Z. Li, W. Wang, X. Liu, A. Wu, P. Xu and D. Zhang, *Appl. Catal., B*, 2018, **236**, 501.
155 G. W. Q. Wang, X. Liang, X. Dong and X. Zhang, *Appl. Surf. Sci.*, 2019, **467–468**, 320.
156 L. Shen, L. Huang, S. Liang, R. Liang, N. Qin and L. Wu, *RSC Adv.*, 2014, **4**, 2546.
157 X. Wei, Y. Wang, Y. Huang and C. Fan, *J. Alloys Compd.*, 2019, **802**, 467.
158 X. X. Xu, H. Y. Yang, Z. Y. Li, X. X. Liu and X. L. Wang, *Chem. – Eur. J.*, 2015, **21**, 3821.
159 Z. Zhang, T. Zheng, X. Li, J. Xu and H. Zeng, *Part. Part. Syst. Charact.*, 2016, **33**, 457.
160 X. Wu, J. Zhao, L. Wang, M. Han, M. Zhang, H. Wang, H. Huang, Y. Liu and Z. Kang, *Appl. Catal., B*, 2017, **206**, 501.
161 Y. Ma, X. Li, Z. Yang, S. Xu, W. Zhang, Y. Su, N. Hu, W. Lu, J. Feng and Y. Zhang, *Langmuir*, 2016, **32**, 9418.
162 R. Miao, S. Zhang, J. Liu and Y. Fang, *Chem. Mater.*, 2017, **29**, 5957.
163 Q. Wang, G. Wang, X. Liang, X. Dong and X. Zhang, *Appl. Surf. Sci.*, 2019, **467–468**, 320.
164 H. Wang, L. Zhang, Z. Chen, J. Hu, S. Li, Z. Wang, J. Liu and X. Wang, *Chem. Soc. Rev.*, 2014, **43**, 5234.
165 L. Xie, Z. Yang, W. Xiong, Y. Zhou, J. Cao, Y. Peng, X. Li, C. Zhou, R. Xu and Y. Zhang, *Appl. Surf. Sci.*, 2019, **465**, 103.
166 Y. Han, C. Bai, L. Zhang, J. Wu, H. Meng, J. Xu, Y. Xu, Z. Liang and X. Zhang, *New J. Chem.*, 2018, **42**, 3799.
167 A. A. Oladipo, *Process Saf. Environ. Prot.*, 2018, **116**, 413.
168 H. Yang, X. Liu, X. Song, T. Yang, Z. Liang and C. Fan, *Trans. Nonferrous Met. Soc. China*, 2015, **25**, 3987.
169 R. Chandra, S. Mukhopadhyay and M. Nath, *Mater. Lett.*, 2016, **164**, 571.
170 Y. Xia, S. K. Shang, X. R. Zeng, J. Zhou and Y. Y. Li, *Nanomaterials*, 2019, **9**, 545.
171 Y. Zhang and S. J. Park, *Appl. Catal., B*, 2019, **240**, 92.

172 M. Ciprian, P. Xu, S. Chaemchuen, R. Tu, S. Zhuiykov, P. M. Heynderickx and F. Verpoort, *Microporous Mesoporous Mater.*, 2018, **267**, 185.
173 Y. Si, Y. Li, J. Zou, X. Xiong, X. Zeng and J. Zhou, *Materials*, 2017, **10**, 1161.
174 Y. Si, Y. Li, Y. Xia, S. Shang, X. Xiong, X. Zeng and J. Zhou, *Crystals*, 2018, **8**, 432.
175 Y. H. Ding, X. L. Zhang, N. Zhang, J. Y. Zhang, R. Zhang, Y. F. Liu and Y. Z. Fang, *Dalton Trans.*, 2018, **47**, 684.
176 J. Qiu, X. F. Zhang, X. Zhang, Y. Feng, Y. Li, L. Yang, H. Lu and J. Yao, *J. Hazard. Mater.*, 2018, **349**, 234.
177 R. Panda, S. Rahut and J. K. Basu, *RSC Adv.*, 2016, **6**, 80981.
178 L. Hu, G. Deng, W. Lu, S. Pang and X. Hu, *Appl. Surf. Sci.*, 2017, **410**, 401.
179 N. Liu, W. Huang, M. Tang, C. Yin, B. Gao, Z. Li, L. Tang, J. Lei, L. Cui and X. Zhang, *Chem. Eng. J.*, 2019, **359**, 254.
180 Q. Xia, B. Huang, X. Yuan, H. Wang, Z. Wu, L. Jiang, T. Xiong, J. Zhang, G. Zeng and H. Wang, *J. Colloid Interface Sci.*, 2018, **530**, 481.
181 R. Yuan, C. Yue, J. Qiu, F. Liu and A. Li, *Appl. Catal., B*, 2019, **251**, 229.
182 X. Liu, R. Dang, W. Dong, X. Huang, J. Tang, H. Gao and G. Wang, *Appl. Catal., B*, 2017, **209**, 506.
183 X. He, H. Fang, D. J. Gosztola, Z. Jiang, P. Jena and W. N. Wang, *ACS Appl. Mater. Interfaces*, 2019, **11**, 12516.
184 J. Huang, H. Song, C. Chen, Y. Yang, N. Xu, X. Ji, C. Li and J. A. You, *J. Environ. Chem. Eng.*, 2017, **5**, 2579.
185 M. Ahmad, S. Chen, F. Ye, X. Quan, S. Afzal, H. Yu and X. Zhao, *Appl. Catal., B*, 2019, **245**, 428.
186 J. Zheng and Z. Jiao, *J. Colloid Interface Sci.*, 2017, **488**, 234.
187 J. Yang, X. Niu, S. An, W. Chen, J. Wang and W. Liu, *RSC Adv.*, 2017, **7**, 2943.
188 A. Soheil, K. Elaheh, A. Moghaddam, M. Reza, S. Laura and J. Christoph, *J. Solid State Chem.*, 2018, **266**, 54.
189 L. He, Y. Dong, Y. Zheng, Q. Jia, S. Shan and Y. Zhang, *J. Hazard. Mater.*, 2019, **361**, 85.
190 Y. Xu, Q. Chen, H. Yang, M. Lv, Q. He, X. Liu and F. Wei, *Mater. Sci. Semicond. Process.*, 2015, **36**, 115.
191 L. Wang and L. Zan, *Sci. Rep.*, 2019, **9**, 4860.
192 Z. Sha, H. S. O. Chan and J. Wu, *J. Hazard. Mater.*, 2015, **299**, 132.
193 Z. Sha, J. Sun, H. S. O. Chan, S. Jaenicke and J. Wu, *ChemPlusChem*, 2015, **80**, 1321.
194 S. Li, X. Wang, Q. He, Q. Chen, Y. Xu, H. Yang, M. M. Lu, F. Y. Wei and X. T. Liu, *Chin. J. Catal.*, 2016, **37**, 367.
195 Z. Sha and J. Wu, *RSC Adv.*, 2015, **5**, 39592.
196 Z. Yang, X. Tong, J. Feng, S. He, M. Fu, X. Niu, T. Zhang, H. Liang, A. Ding and X. Feng, *Chemosphere*, 2019, **220**, 98.
197 R. Zhang, B. Du, Q. Li, Z. Cao, G. Feng and X. Wang, *Appl. Surf. Sci.*, 2019, **466**, 956.
198 Q. Zhang, J. Yang, M. Xu, J. Chen, Y. Lou, J. Zhou and L. Cheng, *J. Chem. Technol. Biotechnol.*, 2018, **93**, 2710.
199 C. Cheng, J. Fang, S. Lu, C. Cen, Y. Chen, L. Ren, W. Feng and Z. Fang, *J. Chem. Technol. Biotechnol.*, 2016, **91**, 2785.
200 Z. Sha, J. Sun, H. S. On Chan, S. Jaenicke and J. Wu, *RSC Adv.*, 2014, **4**, 64977.
201 J. Ding, Z. Yang, C. He, X. Tong, Y. Li, X. Niu and H. Zhang, *J. Colloid Interface Sci.*, 2017, **497**, 126.
202 B. Liu, X. Liu, J. Liu, C. Feng, Z. Li, C. Li, Y. Gong, L. Pan, S. Xu and C. Sun, *Appl. Catal., B*, 2018, **226**, 234.
203 Q. Liang, S. Cui, C. Liu, S. Xu, C. Yao and Z. Li, *J. Colloid Interface Sci.*, 2018, **524**, 379.
204 H. Wang, X. Yuan, Y. Wu, G. Zeng, H. Dong, X. Chen, L. Leng, Z. Wu and L. Peng, *Appl. Catal., B*, 2016, **186**, 19.
205 S. R. Zhu, P. F. Liu, M. K. Wu, W. N. Zhao, G. C. Li, K. Tao, F. Y. Yi and L. Han, *Dalton Trans.*, 2016, **45**, 17521.
206 L. Han, X. Zhang and D. Wu, *J. Mater. Sci.: Mater. Electron.*, 2019, **30**, 3773.
207 Q. Hu, J. Di, B. Wang, M. Ji, Y. Chen, J. Xia, H. Li and Y. Zhao, *Appl. Surf. Sci.*, 2019, **466**, 525.
208 R. M. Abdelhameed, D. M. Tobaldi and M. Karmaoui, *J. Photochem. Photobiol., A*, 2018, **351**, 50.
209 N. A. Rodríguez, A. Savateev, M. A. Grela and D. Dontsova, *ACS Appl. Mater. Interfaces*, 2017, **9**, 22941.
210 R. Kaur, A. Rana, R. K. Singh, V. A. Chhabra, K. H. Kim and A. Deep, *RSC Adv.*, 2017, **7**, 29015.
211 S. Mosleh, M. R. Rahimi, M. Ghaedi and K. Dashtian, *RSC Adv.*, 2016, **6**, 61516.
212 S. Mosleh and M. R. Rahimi, *Ultrason. Sonochem.*, 2017, **35**, 449.
213 H. Ramezanalizadeh and F. Manteghi, *J. Photochem. Photobiol., A*, 2017, **346**, 89.
214 H. Ramezanalizadeh and F. Manteghi, *J. Cleaner Prod.*, 2018, **172**, 2655.
215 Y. Liang, R. Shang, J. Lu, L. Liu, J. Hu and W. Cui, *ACS Appl. Mater. Interfaces*, 2018, **10**, 8758.
216 S. R. Zhu, M. K. Wu, W. N. Zhao, P. F. Liu, F. Y. Yi, G. C. Li, K. Tao and L. Han, *Cryst. Growth Des.*, 2017, **17**, 2309.
217 S. Panneri, M. Thomas, P. Ganguly, B. N. Nair, A. P. Mohamed, K. G. K. Warrier and U. S. Hareesh, *Catal. Sci. Technol.*, 2017, **7**, 2118.
218 D. Yuan, J. Ding, J. Zhou, L. Wang, H. Wan, W. L. Dai and G. Guan, *J. Alloys Compd.*, 2018, **762**, 98.
219 X. H. Yi, F. X. Wang, X. D. Du, P. Wang and C. C. Wang, *Appl. Organomet. Chem.*, 2019, **33**, e4621.
220 D. Guo, R. Wen, M. Liu, H. Guo, J. Chen and W. Weng, *Appl. Organomet. Chem.*, 2015, **29**, 690.
221 W. Huang, L. Ning, X. Zhang, M. Wu and L. Tang, *Appl. Surf. Sci.*, 2017, **425**, 107.
222 Y. F. Y. Li, Z. Cao, N. Li, D. Chen, Q. Xu and J. Lu, *Appl. Catal., B*, 2019, **250**, 150.
223 Z. Shao, D. Zhang, C. Su, X. Pu and Y. Geng, *Sep. Purif. Technol.*, 2019, **220**, 16.
224 S. G. Khasevani and M. R. Gholami, *Inorg. Chem. Commun.*, 2019, **102**, 221.
225 X. Li, Y. Pi, L. Wu, Q. Xia, J. Wu, Z. Li and J. Xiao, *Appl. Catal., B*, 2017, **202**, 653.

226 J. Hong, C. Chen, F. E. Bedoya, G. H. Kelsall, D. O'Hare and C. Petit, *Catal. Sci. Technol.*, 2016, **6**, 5042.
227 X. Du, X. Yi, P. Wang, J. Deng and C. C. Wang, *Chin. J. Catal.*, 2019, **40**, 70.
228 J. Huang, X. B. Zhang, H. Y. Song, C. X. Chen, F. Q. Han and C. C. Wen, *Appl. Surf. Sci.*, 2018, **441**, 85.
229 Y. Gong, B. Yang, H. Zhang and X. Zhao, *J. Mater. Chem. A*, 2018, **6**, 23703.
230 B. Liu, Y. Wu, X. Han, J. Lv, J. Zhang and H. Shi, *J. Mater. Sci.: Mater. Electron.*, 2018, **29**, 17591.
231 X. Zhang, Y. Yang, W. Huang, Y. Yang, Y. Wang, C. He, N. Liu, M. Wu and L. Tang, *Mater. Res. Bull.*, 2018, **99**, 349.
232 Y. Zhang, J. Zhou, Q. Feng, X. Chen and Z. Hu, *Chemosphere*, 2018, **212**, 523.
233 H. Jia, D. Ma, S. Zhong, L. Li, L. Li, L. Xu and B. Li, *Chem. Eng. J.*, 2019, **368**, 165.
234 H. Wang, X. Yuan, Y. Wu, G. Zeng, X. Chen, L. Leng and H. Li, *Appl. Catal., B*, 2015, **174–175**, 445.
235 R. Abazari, A. R. Mahjoub and G. Salehi, *J. Hazard. Mater.*, 2019, **365**, 921.
236 D. A. Giannakoudakis, N. A. Travlou, J. Secor and T. J. Bandosz, *Small*, 2017, **13**, 1601758.
237 D. A. Giannakoudakis, Y. Hu, M. Florent and T. J. Bandosz, *Nanoscale Horiz.*, 2017, **2**, 356.
238 K. Koh, A. G. Wong-Foy and A. J. Matzger, *Chem. Commun.*, 2009, 6162.
239 Y. Yoo and H. K. Jeong, *Cryst. Growth Des.*, 2010, **10**, 1283.
240 T. Fukushima, S. Horike, H. Kobayashi, M. Tsujimoto, S. Isoda, M. L. Foo, Y. Kubota, M. Takata and S. Kitagawa, *J. Am. Chem. Soc.*, 2012, **134**, 13341.
241 S. Furukawa, K. Hirai, K. Nakagawa, Y. Takashima, R. Matsuda, T. Tsuruoka, M. Kondo, R. Haruki, D. Tanaka, H. Sakamoto, S. Shimomura, O. Sakata and S. Kitagawa, *Angew. Chem.*, 2009, **121**, 1798.
242 P. Á. Szilágyi, M. Lutz, J. Gascon, J. Juan-Alcañiz, J. van Esch, F. Kapteijn, H. Geerlings, B. Dam and R. van de Krol, *CrystEngComm*, 2013, **15**, 6003.
243 T. Y. Luo, C. Liu, X. Y. Gan, P. F. Muldoon, N. A. Diemler, J. E. Millstone and N. L. Rosi, *J. Am. Chem. Soc.*, 2019, **141**, 2161.
244 A. Knebel, P. Wulfert-Holzmann, S. Friebe, J. Pavel, I. Strauß, A. Mundstock, F. Steinbach and J. Caro, *Chem. – Eur. J.*, 2018, **24**, 5728.
245 X. Yang, S. Yuan, L. Zou, H. Drake, Y. Zhang, J. Qin, A. Alsalme and H. C. Zhou, *Angew. Chem., Int. Ed.*, 2018, **57**, 3927.
246 T. Li, J. E. Sullivan and N. L. Rosi, *J. Am. Chem. Soc.*, 2013, **135**, 9984.
247 N. Zhou, F. Su, C. Guo, L. He, Z. Jia, M. Wang, Q. Jia, Z. Zhang and S. Lu, *Biosens. Bioelectron.*, 2019, **123**, 51.
248 Y. Gu, Y. Wu, L. Li, W. Chen, F. Li and S. Kitagawa, *Angew. Chem., Int. Ed.*, 2017, **56**, 15658.
249 G. Jia, L. Liu, L. Zhang, D. Zhang, Y. Wang, X. Cui and W. Zheng, *Appl. Surf. Sci.*, 2018, **448**, 254.
250 L. Liu, L. Zhang, F. Wang, K. Qi, H. Zhang, X. Cui and W. Zheng, *Nanoscale*, 2019, **11**, 7554.
251 Y. Liu, A. J. Howarth, J. T. Hupp and O. K. Farha, *Angew. Chem., Int. Ed.*, 2015, **54**, 9001.
252 S. Abdpour, E. Kowsari and M. R. A. Moghaddam, *J. Solid State Chem.*, 2018, **262**, 172.
253 H. L. Tian, T. Araya, R. P. Li, Y. F. Fang and Y. P. Huang, *Appl. Catal., B*, 2019, **254**, 371.
254 P. Pachfule, A. Acharjya, J. Roeser, T. Langenhahn, M. Schwarze, R. Schomäcker, A. Thomas and J. Schmidt, *J. Am. Chem. Soc.*, 2018, **140**, 1423.
255 Y. Zhi, Z. Li, X. Feng, H. Xia, Y. Zhang, Z. Shi, Y. Mu and X. Liu, *J. Mater. Chem. A*, 2017, **5**, 22933.
256 P. F. Wei, M. Z. Qi, Z. P. Wang, S. Y. Ding, W. Yu, Q. Liu, L. K. Wang, H. Z. Wang, W. K. An and W. Wang, *J. Am. Chem. Soc.*, 2018, **140**, 4623.
257 Y. Peng, M. Zhao, B. Chen, Z. Zhang, Y. Huang, F. Dai, Z. Lai, X. Cui, C. Tan and H. Zhang, *Adv. Mater.*, 2018, **30**, 1705454.
258 S. J. He, Q. F. Rong, H. Y. Niu and Y. Q. Cai, *Appl. Catal., B*, 2019, **247**, 49.
259 G. D. Fan, X. M. Zheng, J. Luo, H. P. Peng, H. Lin, M. C. Bao, L. Hong and J. J. Zhou, *Chem. Eng. J.*, 2018, **351**, 782.
260 J. X. Liu, R. Li, Y. F. Wang, Y. W. Wang, X. C. Zhang and C. M. Fan, *J. Alloys Compd.*, 2017, **693**, 543.
261 J. Liu, R. Li, Y. Hu, T. Li, Z. Jia, Y. Wang, Y. Wang, X. Zhang and C. Fan, *Appl. Catal., B*, 2017, **202**, 64.
262 T. T. Isimjan, H. Kazemian, S. Rohani and A. K. Ray, *J. Mater. Chem.*, 2010, **20**, 10241.
263 Q. Liu, C. Zeng, L. Ai, Z. Hao and J. Jiang, *Appl. Catal., B*, 2018, **224**, 38.
264 S. K. Patra, S. Rahut and J. K. Basu, *New J. Chem.*, 2018, **42**, 18598.
265 W. Huang, C. Jing, X. Zhang, M. Tang, L. Tang, M. Wu and N. Liu, *Chem. Eng. J.*, 2018, **349**, 603.
266 S. Gao, T. Feng, C. Feng, N. Shang and C. Wang, *J. Colloid Interface Sci.*, 2016, **466**, 284.
267 Z. Yang, X. Xu, X. Liang, C. Lei, Y. Cui, W. Wu, Y. Yang, Z. Zhang and Z. Lei, *Appl. Catal., B*, 2017, **205**, 42.
268 S. Feng, R. Wang, S. Feng, Z. Zhang and L. Mao, *Res. Chem. Intermed.*, 2019, **45**, 1263.
269 S. Jalali, M. R. Rahimi, K. Dashtian, M. Ghaedi and S. Mosleh, *Polyhedron*, 2019, **166**, 217.
270 F. A. Sofi, K. Majid and O. Mehraj, *J. Alloys Compd.*, 2018, **737**, 798.
271 S. Mosleh, M. R. Rahimi, M. Ghaedi, K. Dashtian, S. Hajati and S. Wang, *Chem. Eng. Process.*, 2017, **114**, 24.
272 X. Yuan, H. Wang, Y. Wu, G. Zeng, X. Chen, L. Leng, Z. Wu and H. Li, *Appl. Organomet. Chem.*, 2016, **30**, 289.
273 Y. Wu, H. Luo and L. Zhang, *Environ. Sci. Pollut. Res.*, 2015, **22**, 17238.
274 Y. Chen, J. Li, B. Zhai and Y. Liang, *Colloids Surf., A*, 2019, **568**, 429.
275 X. Zhao, X. Liu, Z. Zhang, X. Liu and W. Zhang, *RSC Adv.*, 2016, **6**, 92011.

276 H. U. Rasheed, X. M. Lv, S. Y. Zhang, W. Wei, N. Ullah and J. M. Xie, *Adv. Powder Technol.*, 2018, **29**, 3305.
277 L. Qin, Z. W. Li, Z. H. Xu, X. W. Guo and G. L. Zhang, *Appl. Catal., B*, 2015, **179**, 500.
278 X. Y. Li, Y. H. Pi, Q. B. Xia, Z. Li and J. Xiao, *Appl. Catal., B*, 2016, **191**, 192.
279 X. S. Wang, C. H. Chen, F. Ichihara, M. Oshikiri, J. Liang, L. Li, Y. Li, H. Song, S. Wang, T. Zhang, Y. B. Huang, R. Cao and J. Ye, *Appl. Catal., B*, 2019, **253**, 323.
280 Y. Zhao, Y. Dong, F. Lu, C. Ju, L. Liu, J. Zhang, B. Zhang and Y. Feng, *J. Mater. Chem. A*, 2017, **5**, 15380.
281 S. Gholizadeh Khasevani and M. R. Gholami, *Mater. Res. Bull.*, 2018, **106**, 93.
282 S. Gholizadeh Khasevani, N. Mohaghegh and M. R. Gholami, *New J. Chem.*, 2017, **41**, 10390.
283 T. Zhou, G. Zhang, H. Zhang, H. Yang, P. Ma, X. Li, X. Qiu and G. Liu, *Catal. Sci. Technol.*, 2018, **8**, 2402.
284 Y. Chen, B. Y. Zhai, Y. N. Liang, Y. C. Li and J. Li, *J. Solid State Chem.*, 2019, **274**, 32.
285 F. Wang, Y. T. Zhang, Y. Xu, X. Wang, S. Li, H. Yang, X. Liu and F. Wei, *J. Environ. Chem. Eng.*, 2016, **4**, 3364.
286 Q. Liang, J. Jin, C. Liu, S. Xu, C. Yao and Z. Li, *Inorg. Chem. Front.*, 2018, **5**, 335.
287 L. Qian, S. Cui, J. Jin, C. Liu, S. Xu, C. Yao and Z. Li, *Appl. Surf. Sci.*, 2018, **456**, 899.
288 S. Mosleh, M. R. Rahimi, M. Ghaedi, K. Dashtian and S. Hajati, *RSC Adv.*, 2016, **6**, 63667.
289 S. Mosleh, M. R. Rahimi, M. Ghaedi and K. Dashtian, *Ultrason. Sonochem.*, 2016, **32**, 387.
290 N. Liu, W. Huang, X. Zhang, L. Tang, L. Wang, Y. Wang and M. Wu, *Appl. Catal., B*, 2018, **221**, 119.
291 M. A. Henderson, W. S. Epling, C. H. F. Peden and C. L. Perkins, *J. Phys. Chem. B*, 2003, **107**, 534.
292 T. Araya, M. Jia, J. Yang, P. Zhao, K. Cai, W. H. Ma and Y. P. Huang, *Appl. Catal., B*, 2017, **203**, 768.
293 T. Araya, C. C. Chen, M. Jia, D. Johnson, R. P. Li and Y. P. Huang, *Opt. Mater.*, 2017, **64**, 512.
294 W. Guan, X. Gao, G. Ji, Y. Xing, C. Du and Z. Liu, *J. Solid State Chem.*, 2017, **255**, 150.
295 C. Zhang, L. Ai and J. Jiang, *J. Mater. Chem. A*, 2015, **3**, 3074.
296 X. Feng, H. Chen and F. Jiang, *J. Colloid Interface Sci.*, 2017, **494**, 32.
297 S. Li, J. Cui, X. Wu, X. Zhang, Q. Hu and X. Hou, *J. Hazard. Mater.*, 2019, **373**, 408.
298 H. Zhao, L. Qian, H. Lv, Y. Wang and G. Zhao, *ChemCatChem*, 2015, **7**, 4148.
299 S. Kampouri, T. N. Nguyen, M. Spodaryk, R. G. Palgrave, A. Züttel, B. Smit and K. C. Stylianou, *Adv. Funct. Mater.*, 2018, **28**, 1806368.